The copyright of this thesis vests in the author. No quotation from it or information derived from it is to be published without full acknowledgement of the source. The thesis is to be used for private study or non-commercial research purposes only.

Published by the University of Cape Town (UCT) in terms of the non-exclusive license granted to UCT by the author.

University of Cape Town

Gravitational Microlensing and the Search for Extrasolar Planets

By Getachew Mekonnen Mengistie

Supervisors:
Emeritus Prof. Michael Feast(UCT)
Dr. John Menzies (SAAO[1])

Thesis submitted in partial fulfilment of the requirements
of the Degree of Master of Science in Astrophysics and Space Science

April, 2013

Department of Astronomy
University of Cape Town (UCT)

University of Cape Town

[1]South African Astronomical Observatory

Declaration

I know the meaninig of plagiarism and declare that all of the work in the thesis, save for that which is properly acknowledged, is my own.

University of Cape Town

Acknowledgement

I would like to thank Dr. John Menzies, my supervisor, for introducing me to the concept of searching planets using Gravitational Microlensing, a research area in which I dreamt of doing for long time, and for his many suggestions and constant support and guidance in each step of this work for successful completion. He thought me a lot from his wealth experience in research and showed me what real research mean and the way to handle challenges in Astrophysics research. Words can't express my appreciation.

Next I would like to thank Emeritus Prof. Michael Feast, in the department of Astronomy for being my co-supervisor and sharing his wealth of experience in research.

This is a great opportunity to express my respect and appreciation to Professor Keith Horne, St. Andrews, Scotland, since the time I met him during the 2010 PLANET searching campaign, he taught me how microlensing observations are conducted and allowed me to use his FORTRAN code and assisting me in each and every step of the data analysis.

I would like to extend my thanks to the two examiners who spent their precious time to read this thesis and presented critical comments and working on their comments made me grasp a lot of knowledge.In addition their comments made this work more improved content wise as well as making it more explanatory.

I also want to thank the SAAO community for providing me a conducive working environment. Also the SAAO IT group for helping me fixing Desktop and my laptop during my stay.

I also want to acknowledge the National Astrophysics and Space Science Program(NASSP) for offering me the scholarship to study at the university of Cape Town. I would like to extend my gratitude to Mrs. Nicky Walker for her valuable support and advice. I want to extend my gratitude to the Astronomy department, University of Cape Town especially to Ms. Roslyn Daniels (Senior Secretary) of the department for her unreserved assistance in every step of this research thesis. Roz you are a star!!

I also would like to thank Dr. Thebe Medupe for making my stay comfortable in Cape Town during his lecturing time in the NASSP course work and during his visits at SAAO.

I would also thank my family especially MY MOM (ASRESIE KINDIE), brothers and sisters Addisu , Abebe , Muluken (she is always in my side from the very beginning to the end), Tefera , Dr. Demeke , Mimiye for their moral support and encouragement. I also want to thank Seyoum, Abirish, Ermias, Enana, for their moral support. You are all gifts of God, I thank you very much for every thing you did for me. DAD you are and will be in my heart! I missed you! I Love you all.

I would also like to thank my wife, TIGIST SEYOUM. I really appreciate your patience, honesty,commitment and every thing you sacrificed for me while I was studying.

University of Cape Town

Your love, support and encouragement are tools for my hard work and make me strong to work harder and push forward in challenging times. God bless you!

I want to thank also my best friend Bishop Mongwane, who taught me FORTRAN and helping me in every difficulties I faced during this thesis, He is an excellent person with lovable personality, God Bless you!

Last but not least, I am extremely grateful to the following people in Cape Town, Dr. Abiy Getachew, who helped and encouraged me in each steps of my work and fixing my Latex, Hussien Seid for his support, encouragement and his unreserved hospitality, He is a very nice friend with lovable personality, Amare Abebe for his precious time spent in proof reading and critical comments, he is a very nice person with his f(R) personality, Efrem, Fitse, Selam, Millo, Fasilo, Biruh and others for your support and encouragement.

Getachew Mekonnen Mengistie April, 2013

University of Cape Town

Dedication

This Work is dedicated to My Father!!

Abstract

This project is aimed at tackling binary gravitational microlensing events.

Since the early conception of gravitational lensing before Einstein's General Theory of Relativity, physicists and astronomers of the early 18^{th} century speculated that light, if treated as particle, can be affected by gravitational field.

Gravitational Microlensing is defined as a phenomenon occurring when light coming from a distant (source) star is bent by the gravitational field of an intervening mass (lens) creating multiple image of the source which cannot be resolved.

In this project, we applied a model for binary lens microlensing events. We analysed data obtained from different observatories: PLANET, which includes SAAO, Sutherland, Canopus and Perth observatories, OGLE, Danish Telescope, LaSilla. For the observed microlensing target OGLE-2011-BLG-265, analysis of the data using the program supplied by Keith Horne, using different minimization schemes and algorithms, I found best fit model to be a binary lens with mass ratio q = 0.0042 and separation of components is found to be u = 1.034 where in this case the separation falls under an intermediate binary lens topology.

Finally, the deviation from the point-source point-lens microlensing events on the light curve and small mass ratio suggested a planetary system. I also calculated the time, t_p, that the source needs to cross the diameter of the planet Einstein Ring radius, which is related to the mass ratio, and is found to be 3.30 days.

University of Cape Town

Contents

University of Cape Town

University of Cape Town

List of Tables

University of Cape Town

List of Figures

University of Cape Town

University of Cape Town

University of Cape Town

University of Cape Town

University of Cape Town

University of Cape Town

1 Introduction

University of Cape Town

1.1 Historical Background

The deflection of light by a gravitational field was suspected well before Einstein's formulation of the General Theory of Relativity. In 1704, Sir Isaac Newton in his Opticks paper asked, "Do not bodies act up on light at a distance, and by their action bend its rays; and is not this action(caeteris paribus) strongest at the least distance?" (Schneider et al., 1992).

Several physicists and astronomers in the early 18^{th} century speculated that if light could be treated like a particle, light rays might be affected by a gravitational field. John Mitchell in 1784 and later Johann Georg Soldner in 1804, explained the possibility that light propagating in the gravitational field of a spherical mass M could be deflected by the gravitational field of the mass and determined the first known deflection angle of the light ray, using Newtonian mechanics, and obtained

$$\hat{\alpha_N} = \frac{2GM}{c^2\xi}, \tag{1.1}$$

where G and c are Newtonian constants of gravity and speed of light respectively and ξ is the impact parameter, the closest distance of a light ray to the mass, M. But this deflection angle was half of the value calculated with General Theory of Relativity

(Paczynski, 1996). Later in 1795, Pierre-Simon Marquis de Laplace described the influence of a heavy body's gravitational force on light flow. With the aid of General relativity it is now possible to give a correct expression for the radius within which light cannot escape from a given mass. This is now referred as the Schwarzschild radius, and is given by :

$$R = R_s = \frac{2GM}{c^2}, \tag{1.2}$$

(Schneider et al., 1992), (Schneider, 2006).

Theoretical works regarding deflection of light were done assuming that light could behave as a test particle: during that time the concept of photons was not introduced (Schneider, 2006). But the advancement in the General Theory of Relativity, by Albert Einstein, especially the paper he published in 1911, helped him to obtain the same value for the deflection angle from the principle of equivalence as obtained by Soldner. He derived the deflection angle without the prior knowledge and work of Soldner (Schneider et al., 1992). Some time after the theoretical work derived by Einstein, the deflection angle was observationally confirmed during solar eclipse with some 30% error, though some scientists did not accept this result due to the growing antisemitism in the early 1920s in Germany (Schneider et al., 1992). But this deflection angle was later confirmed by observation using radio-interferometric method with 1% error (Schneider, 2006).

After all these works O.G Lodge in 1919 used the term 'lens' in relation to the gravitational light deflection, but emphasized that 'it has no focal length' (Schneider et al., 1992; Schneider, 2006). Then Schneider et al. and Schneider in their two papers (1992 and 2006) described the next major step studied by Eddington regarding the formation of multiple images. Eddington also stated that when we observe from Earth, it is known that primary images appear and the second dimmer image will appear on the opposite side of the closer star. Soon after Eddington's remarkable work, Chwolson (1924) described the formation of an Einstein ring when the source is perfectly aligned with a foreground mass. He concluded that the source should be imaged as a ring around the lens.

In 1936 Einstein published a paper which describes the equation of gravitational microlensing by a foreground star (Gaudi, 2010) but at the same time he dismissed the practical significance of microlensing effect. He also concluded "there is no great chance of observing this phenomenon" due to the low rate of occurrence of gravitational microlensing. For some time studies in this field were a bit slow, even dormant (Gaudi, 2010).

Between 1963 and 1964 studies were made on lensing of galaxies by galaxies (Klimov, 1963) and lensing by point mass lenses (Liebes, 1964; Refsdal, 1964). Refsdal also studied the time delay for the two images due to the different light travel time along light rays

University of Cape Town

corresponding to each image (Schneider, 2006). These remarkable works initiated the rebirth of gravitational lensing.

Walsh et al. (1979) discovered the first case of a double image created by gravitational lensing of a distant source, the quasar $0957 + 561$. In his paper, Paczynski (1996)(and references therein) also mentioned that a point mass in a halo of a distant galaxy would create two unresolvable images of a background quasar, but the time variation of their brightness could be observed. This is also a method to detect the effect of non-luminous matter. Paczynski (1986) introduced the term "microlensing", which describes the effect of gravitational lensing that can be studied by the change in intensity of macro-images made from unresolved micro-images.

In his second paper Paczynski suggested that dark matter halo can be detected by studying light variability of target stars in the Large and Small Magellanic Clouds and Griest (1991) proposed that MACHOs (Massive Astrophysical Compact Halo Objects) are responsible for gravitational microlensing, an event that could be used to detect brown dwarfs as well as to discover planetary companions to the primary microlens star (Mao & Paczynski, 1991).

Microlensing in the search of planets was studied by Gould & Loeb (1992) and laid the foundation for the observational search for planets (Gaudi, 2010). They also introduced two-phase observational evidence: the first one is to discover suspected targets using one dedicated telescope and alert observers to monitor these targets. In the second phase, the alerted events will be monitored by many telescopes all over the world.

In 1995 several follow-up observation groups and collaborations dedicated to planet searching started monitoring microlensing targets so as to find planetary deviations from ongoing events. These collaborations will be discussed in detail in the upcoming chapters. Although intensive monitoring was done in selected targets, no certain planet detections were made from $1995 - 2001$ due to the fact that the number of alerted events was quite small ($50 - 100$ targets per year) (Gaudi, 2010). Gaudi (2010) also stated that some time later in 2001, one of the collaborations, OGLE, (Udalski, 2003) upgraded its telescope with a new camera with 16 times larger field of view which enabled them to find many targets as well as leading to the detection of the first extrasolar planet using microlensing in 2003 . This paved the way for other groups to upgrade their telescopes. Among these the MOA (Microlensing Observation in Astrophysics) collaboration upgraded to a 1.8 metre telescope with $2deg^2$ camera in 2004. The two collaborations then increased the number of targets to be monitored for planet searching to 850 events each year.

University of Cape Town

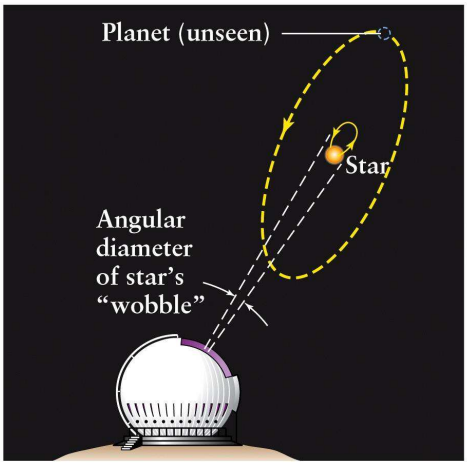

Figure 1.1: Figure illustrating astrometry technique (Adapted from :www.astro.wisc.edu/ ∼ townsend)

University of Cape Town

1.2 Techniques used to detect planets

Extrasolar planets are difficult to observe because they are faint light sources as compared to their host stars. So detecting extrasolar planets by the light coming from them is difficult and hence indirect methods are applied to find these planets. In this section an overview of the techniques used to detect extrasolar planets will be summarized.

1. Astrometry: one of the oldest methods to search for planets. It is a technique to search for planets by studying the exact position of a star and directly detect the wobbling. In this method the mass of the host star is assumed to be larger than the planet so that the centre of mass is much closer to the host star and the two, planet and star, are orbiting around this common centre of mass called the barycenter, making the orbit of the star to be very small as compared to that of the planet.

   In this method the main task is to observe the periodic changes in the position of the star on the plane of the sky and this will be done by subtracting out the star's apparent motion due to parallax motion and the projection of its real proper motion through space (Doyle, 2008). Though many attempts for planetary detection around nearby stars were made using ground based telescope observations, none of the possible detections have been confirmed with modern methods. This is due to the fact that the change in the position of the stars is very small. So the fate of astrometry heavily relies on space based observations. The Hubble telescope in its

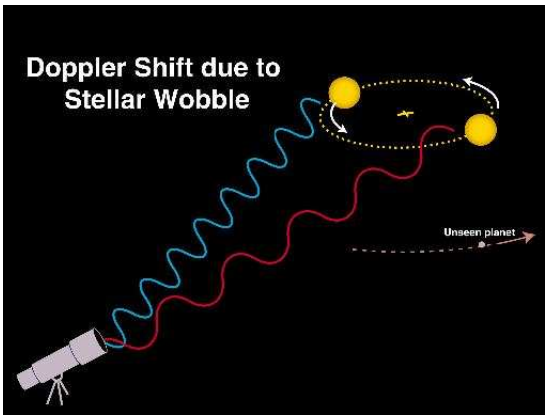

Figure 1.2: Illustration of Radial Velocity Method (Adapted from http:www.deepfly.org/ TheNeighborhood/ 7c1)

University of Cape Town

Fine Guide Sensor (FGS) was successfully used on $2-3$ objects to detect exoplanets (Perryman, 2011)(and references therein). The European Space Agency(ESA) is also working on a mission called GAIA, to be launched in 2012, using astrometric techniques (Perryman, 2000, 2011) to find exoplanets as it is illustrated in Fig.1.1.

2. Radial Velocity: This is one of the most successful planet search techniques from ground based telescopes. This method requires intensive monitoring of the variation in the spectrum of the light coming from the star. When a star-planet system rotates about their common barycentre, the variation in velocity of the star can be measured when it moves toward or away from the Earth and hence results in the variation of the spectral lines of the light emitted due to the Doppler effect. Fig.1.2 shows the illustration of radial velocity method, which shows the Doppler shift due to the stellar wobble.

   When the star moves toward the Earth, an observed spectrum line shifts to the blue and when it moves away, a red-shifted spectrum is observed as it is illustrated in Fig. 1.2. The relation between velocity v and wave length shift $\Delta\lambda$ is $\frac{\Delta\lambda}{\lambda} = \frac{v}{c}$. Because the star is much more massive than the planet the value of $\Delta\lambda$ is very small.

   For the planetary system in our solar system, the amplitude of the radial velocity of the sun is about $13m/s$ for Jupiter and $0.1m/s$ for the Earth. The precision currently obtained for radial velocity method is $\sim 1m/s$ (Doyle, 2008). Therefore, this technique is limited to detecting Jupiter sized planets.

3. Transit Method: This technique relies on the drop in brightness of parent star when

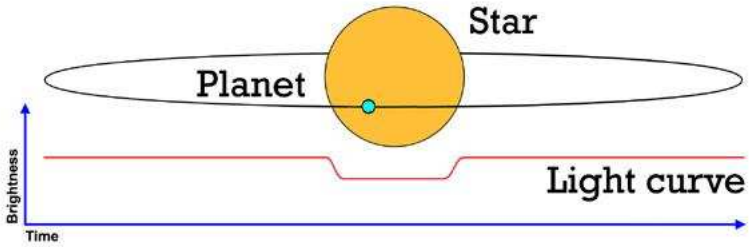

Figure 1.3: Figure showing Transit method alignment (Adapted from:http:www.deepfly.org/ TheNeighborhood/7c1)

the orbital plane of an extrasolar planet is seen edge-on from Earth and the planet happens to pass in front of the parent stars. Once in every orbit, there will be a partial eclipse. This leads to detection of periodic dimming which can imply the presence of a planet. The amount the star dims depends on the size of the parent star as well as the size of the planet. This phenomenon is illustrated in Fig.1.3, showing a planet orbiting a host star causes a drop in brightness of the host star as the planet passes in front of it which is revealed in the light curve.

The main advantage of this method is that the size of the planet can be determined from the light curve. In combination with the radial velocity method, which can help to determine mass of the planet, it is possible to determine the density of the planet which in turn leads to the study of the physical nature of the planet. The planet orbit can also be determined exactly. Using ground based observations, transit method can only detect gaseous and very large planets due to the fact that the drop in brightness of the host star may not be detected for smaller sized planets. There are two main drawbacks of the transit method: the first is, in order to see planetary signals using this method, planetary transits can only be observed when planets' orbit happen to be perfectly aligned from the observer's point of view. This alignment happens rarely. The other drawback of this method is, its susceptibility to high rate of false detection, because many of the stars in our galaxy happen to have binary components and multiple systems that lead to eclipsing. This does not mean that a planet transit is happening. So, this method sometimes requires additional confirmation from other methods like the radial velocity method.

To detect Earth-like rocky planets, nowadays space-based observations play a major role. One of these space-based observations is CoRoT (Convection, Rotation and Transit) is a mission launched in 2006 and is playing a major role in exploring planets. CoRoT is a collaboration of the French space agency CNES, ESA(European

University of Cape Town

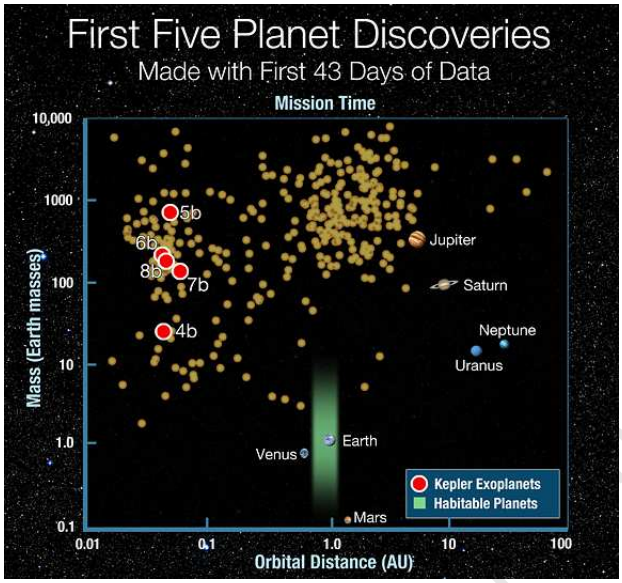

Figure 1.4: Planets detected using Kepler's Mission (Adapted from:www.onorbit.com/Astronomy?)

Space Agency), Austria, Belgium, Brazil, Germany and Spain (Auvergne et al., 2009). The other space-based mission in observing exoplanets is the Kepler mission, whose primary goal is to determine the frequency of Earth-size and larger planets in the habitable zone. Habitable zone is defined as a region capable of supporting life in the solar system or it is a distance from a star where Earth-like planets can maintain water on their surface and sustain life (Borucki et al., 2010).

University of Cape Town

Figure 1.4 shows the planets detected by Kepler mission which was sent to orbit in 2009, and monitors stars for a decrease in brightness that results from transiting planets. This mission detected five planets in the first 43 days of data collected. It is currently monitoring and measuring changes in brightness of 150,000 solar-like stars to study patterns in transit. This method also helps to get information about the size of the planet with respect to the star and its orbital period (Borucki et al., 2010). Combining results from Kepler's measurement with ground-based spectroscopy, astronomers obtain stellar parameters, the planet radius, orbital semi-major axis and its location relative to the habitable zone. Endl et al. (2011) presented the first confirmed planet, Kepler-15b, a giant planet observed from the Kepler mission later confirmed with ground based observation in the Hobby-Eberly Telescope at McDonald Observatory. Using the high-resolution-spectrograph, the mass of the Kepler's planet via radial velocity was measured. They also determined the stellar parameters as well as properties of the host star (Endl et al., 2011).

4. Direct Imaging: This method focuses on direct observation of planets around other stars, so that researchers analyze the light reflected from the planet itself, determine chemical composition and assess the physical state of the planet. But this method is difficult to use with the observing facilities available on account of a planets low brightness as compared to the host star. There are exceptional cases like GQ Lupi b (Neuhäuser et al., 2008) and 2M1207*b* (Mohanty et al., 2007) planets which are detected using direct infrared images by two groups using the European Southern Observatory Very Large Telescope Array in Chile. These planets have masses very much larger than the mass of Jupiter and they orbit at 50 AU from the parent star.

5. Gravitational Microlensing: It is one of the indirect methods of extrasolar planet searching techniques having different principles as compared to the previous methods. That is, when a light coming from a background source passes close to a very large mass, the lens, it will be deflected by the gravitational field of this mass and results in the formation of two images on opposite side of the lens mass, one of the unique features of gravitational microlesing. To study microlensing principles it is customarily to define three different planes: the source plane, the lens plane (deflector plane) and the observer's plane, which are perpendicular to the optical axis which passes through the centre of the lens plane.

   The effect of microlensing results in the formation of multiple images with separation of the order of $2\theta_E$, where θ_E is the Einstein angular radius, which is far below the lower limit of resolution set for observation (Wambsganss, 2006). Microlensing in

University of Cape Town

general happens to occur for small mass objects with large distance between source and lens as well in compact objects with mass range between $10^{-6} \leq \frac{M}{M_{\odot}} \leq 10^{6}$, where $M_{\odot}$ is the solar mass (Wambsganss, 2006). This mass range can be translated into Einstein radii/ angular separation of milli-arcsecond or smaller depending on the two distance regimes. For an event supposed to be galactic microlensing the source-lens separation should be of the order of 10kpc whereas extragalactic or cosmological microlensing events have distances of the order of Gpc (Wambsganss, 2006). Gravitational microlensing is different from other methods of planet searching techniques because it is a purely gravitational method which does not depend on detecting photons from either the planet or its host star (Bennett, 2010).

The unique features of microlensing, as stated in (Bennett, 2010), in searching for planets as compared to the other techniques is its amplitude of planetary microlensing signal which typically is $\geq 10\%$. Microlensing is more sensitive to low mass planets and its sensitivity extends as low as 0.1 $M_{\odot}$ mass planets regarding the orbital separation this method can detect planets in the range of $1.5-4$AU and can be used as a supplement for radial velocity method and transit. The other unique feature of microlensing is its ability to detect old free floating planets from ground based observations as well as detecting planets orbiting unseen stars.

Gravitational microlensing observations have shortcomings. Among these, one is difficulties to identify the target under consideration. In addition it is hard to study the property of the stars. But the aforementioned challenges can be tackled using space-based observations which helps one to get information about the host star and in turn make it possible to study its properties.

6. Pulsar Timing

A Pulsar is a rapidly rotating/ spinning neutron star with a strong magnetic field. Due to the presence of the magnetic field, the radiation produced by neutron stars is focused in two oppositely directed beams. These radiation beams are swept across the sky as the star rotates. If the beam intercepts the Earth once per rotation regular pulses of radiation can be seen. It is believed that some pulsars can exist with planets. So if a planet exists closer to the pulsar, both the planet and the pulsar rotate in their centre of mass, which is close to the pulsar because it is heavier than the planet. After one complete rotation the pulsar travels smaller distance as compared to the planet. Similarly as the methods discussed before, the pulsar's wobble is small, but pulsar wobble affects the timing of pulses received from the pulsar.

University of Cape Town

As in Doppler method, when a pulsar moves away from the Earth, the time between each pulse becomes longer and in reverse, when a pulsar moves toward the Earth, the time will be shorter. So by measuring periodic changes in pulse timing, the existence of planets around the pulsars together with estimates of the semi-major axis of the planet's orbit as well as a lower limit on the mass of the planet can be obtained. In searching for extrasolar planets, unexpectedly, the first planetary object was detected around a pulsar. The parent star was the pulsar PSR B1257+12, 500 pc away, two planetary objects detected around it with $2.8M_{\oplus}$ having a period of 98.22 days and a $3.4M_{\oplus}$ with a period 66.54 days (see Doyle (2008) and references therein).

In order to search for planets using the pulsar timing method it is good to study the basics on the time delay of pulses by considering a system consisting of a planet of mass M_p orbiting around a pulsar, a_p distance away from the common barycentre and a pulsar with mass M_* and a_* away from the barycentre to the centre of the pulsar, where the barycentre is a common point around which the pulsar and the planet rotate. During rotation, the motion of the pulsar around the barycentre causes the addition/subtraction of the light travel time which in turn results in delay or early arrival of the periodic variations in the timing of the pulsar pulses. A pulsar and a planet rotating in a circular orbit around a barycentre cause a maximum amplitude of time delay given by:

$$\tau = sin\,(i)\frac{a_p}{c}\frac{M_p}{M_*}, \tag{1.3}$$

where i is the inclination of the planet's orbit (i = 90^o, edge-on orbit), c- the speed of light.

For phase angles 90^o and 270^o, the pulses will be 'on time' whereas for phase angle 0^o, the pulse will be late by an amount τ. For phase angle 180^o, the pulse will be early by an amount τ (Doyle, 2008). Using the light travel time across the stellar-barycentre distance, the pulsar timing method can be used to determine the planet-star mass ratio, true orbital period of the planet and if the planet-star system orbit is not circular its eccentricity can be determined as well. Pulsar timing is very sensitive and is capable of detecting planets with $(\frac{1}{10})^{th}M_{\oplus}$. Jovian or terrestrial planets can also be detected around normal slow pulsars (Perryman, 2000). This method is capable of detecting mutual gravitational perturbations. Its analysis in turn can reveal information about the planet and its orbital parameters.

University of Cape Town

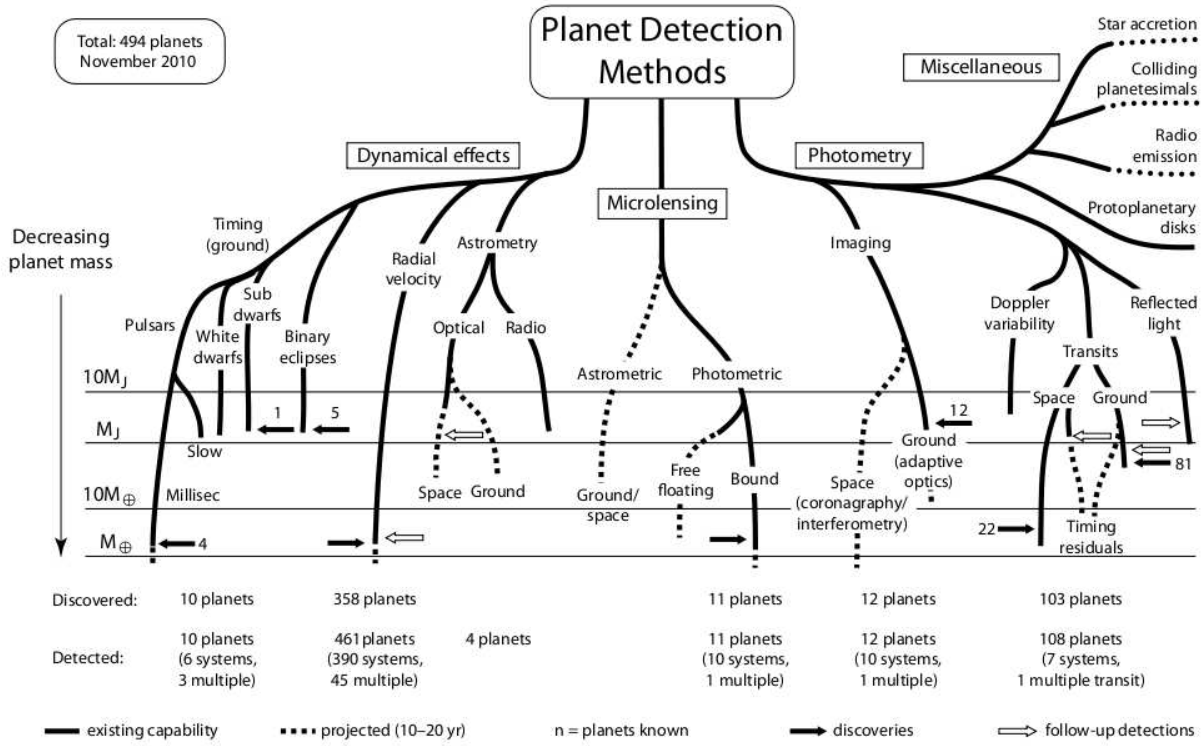

Figure 1.5: Techniques used to detect planets and the total number of planets detected (Adapted from: http:exoplanet.eu/papers/macp-detection-methods.pdf)

The figure above, Fig.1.5, shows the general overview of the methods to find extrasolar planets and their capabilities in finding smaller mass planets. It also shows the existing capability of planet searching and projected plans for the coming $10 - 20$years.

University of

1.3 Objectives

This work aims to tackle problems related to modeling microlensing events and address the following main points:

(a) Review concepts of Gravitational Microlensing and its application in searching extrasolar planets.

(b) Rudimentary program is available, but needs more elaboration so that SAAO (the South African Astronomical Observatory) can join modeling efforts to improve efficiency of network

(c) Visualization of circumstances of events and prediction of light curves is required

University of Cape Town

1.4 Outline of the thesis

This work focuses on studying gravitational microlensing in searching for extrasolar planets and is organized as follows:

In the Introduction, the thesis addresses the historical background of gravitational lensing and also gives a brief overview of different methods of planet searching techniques as well as introducing the main thrust of the work ahead. The second chapter will try to address the theoretical background of gravitational lensing. In this section gravitational lensing by single lens star, amplification, modeling point- source point-lens gravitational microlensing events, their light curves and some examples will be presented. This section will also try to give an overview about finite-source effect.

In Chapter Three, we extend the point-source point-lens model to more complex binary lens events and the theoretical background of binary microlensing formalism as well as overview of binary lens with the presence of shear is presented. The fourth chapter addresses caustics, critical curves, and topologies of binary lenses. The fifth chapter is devoted to giving overview of microlensing in searching extrasolar planets, observational evidences and groups working on planet searching as well as the advantages and drawbacks of the microlensing techinique . In the sixth chapter, we review the planets discovered through gravitational microlensing and the last two chapters focuses on the main results of the research work. Finally, in the appendix

summary of the optimization techniques used in analysis of microlensing data is presented.

2

Theory of Gravitational Lensing

University of Cape Town

Gravitational lensing during the early stages of its theoretical development was mostly considered as a subject of curiosity which is related to the bending of light by the gravitational field of massive objects predicted by the General Theory of Relativity. However, for the last few years ($2-3$ years) this phenomenon was observed quite intensively so that many scientists have been engaged in studying these events. This has made gravitational lensing as one of the promising research areas for both astrophysicists and cosmologists due to the fact that studying these lensing events in one or in another way has a major implication in understanding the universe.

In this chapter we will try to give a brief overview of lensing equations for single lens microlensing events, image formation, Einstein Ring radius, amplification, and the finite source effect so as to lay foundation for the binary microlensing events to be discussed in the later chapters.

2.1 Gravitational Lensing by Single Stars

The simplest and easiest case of microlensing is due to the presence of a single lens in the lens plane and a single source star in the source plane. Lensing by a single star has some features which will help us in deriving the lens equation. Among these are the following:

(a) The star is assumed to be spherically symmetric and all light rays coming from the source and approaching the lens in a distance range $\xi > R$, where R is the radius of the lens, ξ, the closest distance from the lens, and the basic physics of Gravitational lensing depends only on a single input from the General Theory of Relativity, the deflection angle $\widehat{\alpha}$, given by:

$$\widehat{\alpha} = \frac{4GM}{c^2\xi}, \tag{2.1}$$

where M is the total mass of the lens star.

(b) The source can be considered as a point source if the angular size is smaller than the Einstein Radius θ_E, further explanation of this term is going to be given in the upcoming section.

University of Cape Town

2.1.1 Normalized Lens Equations

The lens equation usually describes a mapping from the lens plane to source plane. Using these equations we can easily study all the properties of point mass lenses including caustic curves and critical lines, which give rise to infinite magnification at the source or image positions, and also describe the behavior of amplification of sources close to the folds and cusps of the caustic curves (Mollerach & Roulet, 2002) with little effort in numerical work.

Gravitational microlensing events occur when a foreground object (lens) passes very close to our line of sight to a very distant background star (source). Since, as Gaudi (2010) described, microlensing is a relatively improbable phenomenon, to increase the chance of detecting these events, astronomers usually search for targets toward dense stellar fields, mostly toward the galactic center especially for planet microlensing surveys.

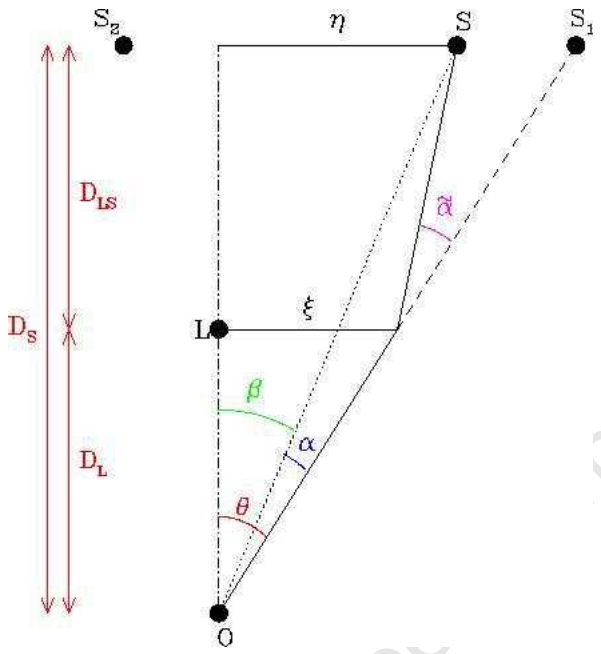

Figure 2.1: A schematic representation of gravitational lensing by a spherically symmetric single lens showing observer position O, lens position L and the two images S_1 and S_2. D_{LS}, D_s, and D_L are distances from source plane to lens plane, observer plane to source plane and observer plane to lens plane, respectively (Schneider 2006)

.

To study the point-source point-lens model, let us derive the lens equation, which relates the observed image positions to the actual source position in the presence of deflectors (lenses) by considering the simplest situation:

$$\beta = \theta - \alpha. \tag{2.2}$$

Introducing the reduced deflection angle α as $\alpha \equiv \widehat{\alpha}\frac{D_{LS}}{D_S}$, and substituting back this value the lens equation can be rewritten as

$$\theta D_S = \beta D_S + \widehat{\alpha} D_{LS}, \tag{2.3}$$

where D_{LS} and D_S are distances from source plane to lens plane and observer plane to source plane. This is the equation that we are going to use to study single lens microlensing events and is henceforth referred to as the *lens equation*. This equation explains the relation between the real and apparent position of the source.

The lens equation given by equation 2.3 is non-linear, which is going to be verified later in this work. This equation provides the chance to observe multiple images at the position θ corresponding to a single source at the angular separation of β. The figure above (Fig. 2.1), shows the position of the two images on either side of the source labeled as S_1 and S_2. To make the lens equation clear, it is possible to reduce the deflection angle for the point-like lens using the closest distance ξ which can be written as $\xi = \theta D_L$.

Then substituting the value of $\widehat{\alpha}$ from equation 2.1 one obtains,

$$\alpha = \frac{4GM}{\xi c^2}\frac{D_{LS}}{D_s}. \tag{2.4}$$

Using the value of ξ once more this equation can be rewritten the following form:

$$\alpha = \frac{4GM}{\theta D_L c^2}\frac{D_{LS}}{D_s}, \tag{2.5}$$

Substituting equation 2.5 back into equation 2.3, by using the value of α from the reduced deflection angle, and rearranging, the lens equation can be rewritten as:

$$\theta^2 - \beta\theta - \theta_E^2 = 0, \tag{2.6}$$

where $\theta_E = \sqrt{\frac{D_{LS}}{D_S D_L}\frac{4GM}{C^2}}$, called the Einstein ring radius, is the unit to which all length and time scales in gravitational lensing are normalized to make all lensing variables dimensionless. If we try to solve the lens equation for position of the source β, as shown in Fig.2.1 above, we can get the position of the image which corresponds to θ.

Since equation 2.6 is quadratic in θ, we can get two solutions, which are positions of the two images. Now let us investigate the image position for different cases:

(a) For $\beta = 0$, a special case in which the source and lens are perfectly aligned, due to the symmetry of the lens configuration, the image is a ring of angular radius θ_E called the Einstein ring radius.

(b) For $\beta \neq 0$, the case of imperfect alignment, the solution of the lens equation is given by:

University of Cape Town

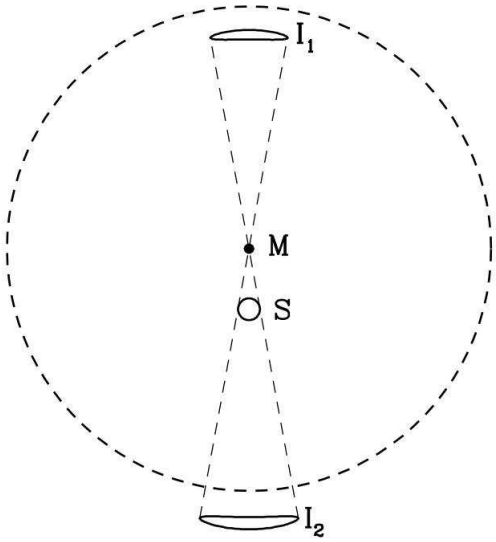

Figure 2.2: Figure showing lensing mass M, source S and the two images produced I_1 and I_2 due to the gravitational microlensing as well as the Einstein ring radius, the circle shown with dashed lines observed from the sky (Adapted from Paczynski, 1996).

$$\theta_{\pm} = \frac{\beta}{2} \pm \theta_E \sqrt{1 + \frac{\beta^2}{4\theta_E^2}}. \tag{2.7}$$

One of the images, the major image, is always outside the Einstein ring radius $\theta_+ \geq 1$ on the same side of the lens as the source and the other image called minor image is always inside the Einstein ring radius $\theta_- \leq 1$ on the opposite side of the source and the optical axis as it is illustrated in Fig.2.2 (Mao, 2008; Gaudi, 2010).

We can also further study the angular separation of the two images as:

$$\triangle\theta = \theta_+ - \theta_-, \tag{2.8}$$

$$\triangle\theta = \frac{\beta}{2} + \theta_E \sqrt{1 + \frac{\beta^2}{4\theta_E^2}} - \frac{\beta}{2} + \theta_E \sqrt{1 + \frac{\beta^2}{4\theta_E^2}}, \tag{2.9}$$

$$\triangle\theta = \theta_+ - \theta_- = 2\theta_E \sqrt{1 + \frac{\beta^2}{4\theta_E^2}}. \tag{2.10}$$

If $\beta < \theta_E$ the deviation from the optical axis is small as compared to the Einstein angle and the image separation is approximately twice the Einstein radius. It is also possible to derive a dimensionless lens equation by dividing the lens equation with θ, that is:

$$\beta\theta = \theta^2 - \theta_E^2, \tag{2.11}$$

$$\beta = \theta - \frac{\theta_E^2}{\theta}, \tag{2.12}$$

$$\frac{\beta}{\theta_E} = \frac{\theta}{\theta_E} - \frac{\theta_E}{\theta}. \tag{2.13}$$

Now define $\frac{\beta}{\theta_E} = u$ and $y = \frac{\theta}{\theta_E}$, so the lens equation will have the form $u = y - \frac{1}{y}$, reduced to a quadratic equation in y and hence resulting in two solutions $y_\pm = \frac{1}{2}\{u \pm \sqrt{u^2 - 4}\}$. As discussed earlier in this section the nonlinearity of the lens equation is verified here since we get two solutions from the lens equation.

Thus, a point-mass has two images for any source, irrespective of its distance y from the lens. Since the Einstein angular radius is of the order of milliarcseconds for typical lens masses $M \simeq M_\odot$, source and lens distance of the order of $\simeq$ 3kpc in events toward the galactic bulge, the images are unresolved (Gaudi, 2010).

2.2 Amplification

Gravitational lensing preserves the number of photons, it only redistributes them. An observer either receives more photons (amplified) or less photons (de-amplified) in comparison to the absence of the lens. In order to get the amplification or de-amplification it is relevant to discuss the change in the solid angle of the source to be observed. The flux received from a source during observation is the product of surface brightness and the solid angle it subtends (Mollerach & Roulet, 2002). Gravitational lensing conserves surface brightness but, the differential deflection of light ray changes the shape and solid angle that a source subtends on the sky. It amplifies the source luminosity by:

$$A = \frac{d\Omega}{d\Omega_0}, \tag{2.14}$$

University of Cape Town

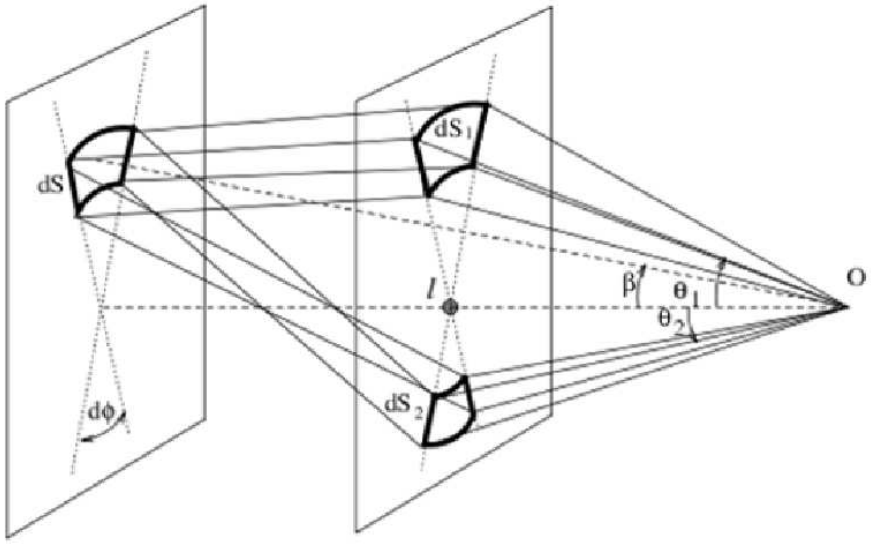

Figure 2.3: Figure showing trajectories of light rays from a surface area dS of the source and its corresponding two images dS_1 and dS_2 projected on the lens plane (Adapted from Mollerach and Roulet, 1996).

where $d\Omega$ is the observed solid angle and $d\Omega_0$ is the solid angle in the absence of gravitational lensing. We clearly stated previously that a source with angular position $\overrightarrow{\beta}$ has two images at θ_+ and θ_-. Consider a source element dS in Fig.2.3, subtending a solid angle $d\Omega_0 = \frac{dS}{D_s^2} = \beta d\phi d\beta$ observed in the image positions subtending a solid angle $d\Omega_\pm = \frac{dS_\pm}{D_L^2} = \theta_\pm d\phi d\theta_\pm$. Then the amplification of each of the images is given by:

$$Magnification = \frac{Image\,solid\,angle}{Source\,solid\,angle} = \frac{Image\,area}{Source\,area}. \tag{2.15}$$

The total magnification if i is the number of images can also be written as:

$$A = \sum_i A_i = \sum \frac{1}{|detJ_{j,k}|_i}, \tag{2.16}$$

where $J_{j,k}$ is the Jacobian and is the transformation matrix from lens plane $\xi = (\xi_1, \xi_2)$ to the source plane $\eta = (\eta_1, \eta_2)$ given by:

$$J_{j,k} = \frac{\partial \eta_j}{\partial \xi_k}. \tag{2.17}$$

The gravitational lensing equation is a mapping from lens to source plane. Due to this mapping the area of the image is not necessarily equal to the source area, thus the source is either magnified or de-magnified. The magnification of each image is just the amount the source area element is 'stretched', which is given by the inverse of the determinant of the Jacobian. Mathematically, stretching is given by inverse value of the Jacobian determinant, of the mapping from image to source evaluated at the image position (Bozza et al., 2011)

$$A_{\pm} = \frac{d\Omega_{\pm}}{d\Omega_0} = \frac{\theta_{\pm} d\theta_{\pm}}{\beta d\beta}. \tag{2.18}$$

By using the lens equation we can rewrite the amplification as

$$A_{\pm} = \frac{1}{2} \pm \frac{\beta^2 \pm 2\theta_E^2}{2\beta\sqrt{\beta^2 + 4\theta_E^2}}. \tag{2.19}$$

For the image appearing on the opposite side of the lens, at an angle θ_-, the amplification is denoted by A_-, meaning the image is inverted. On the other hand, from the images produced in Fig.2.2 the two images are stretched horizontally and are contracted radially (Mao, 2008; Gaudi, 2010). So, the amplification will have the following form:

$$A_{\pm} = |\frac{y_{\pm}}{u}\frac{dy_{\pm}}{du}|, \tag{2.20}$$

$$A_{\pm} = \frac{1}{2}\{\frac{u^2+2}{u\sqrt{u^2+4}} \pm 1\}. \tag{2.21}$$

The total magnification is then reduced to the following form

$$A(u) = \frac{u^2+2}{u\sqrt{u^2+4}}, \tag{2.22}$$

where $u = \frac{\beta}{\theta_E}$ and $y = \frac{\theta}{\theta_E}$. As authors like Gaudi (2010) stated if $u \to \infty$, then $A_+ \to 1$ and $A_- \to 0$.

University of Cape Town

This implies two important results: the first one is that one of the images formed is unchanged while the other does not exist during microlensing. For image separations of the order of milliarcseconds, gravitational microlensed images which cannot be resolved can be detected by considering the total magnification obtained from the source.

The total amplification in terms of the variables introduced earlier can be written as: $A = A_+ + |A_-| = \frac{\beta^2+2\theta_E^2}{\beta\sqrt{\beta^2+4\theta_E^2}}$. Since the original source flux is not known, measuring the total amplification, A, is difficult from a single observation. Whereas by taking into account the relative motion of the source and lens which resulted in time-dependent amplification helps to measure the variation of the luminosity of the image (Mollerach & Roulet, 2002). The Einstein crossing time scale for a microlensing event for a transverse velocity between source and lens, $V_\perp$, is given by:

$$t_E = \frac{R_E}{V_\perp}, \tag{2.23}$$

which is equivalent to saying

$$t_E \backsimeq 70 \times \sqrt{\frac{M_L}{M_\odot}} \times \sqrt{\frac{D_S}{8kpc}} \times \sqrt{\frac{D_L D_{LS}}{D_S}} \times \frac{V_\perp}{200km/s}^{-1} days, \tag{2.24}$$

where R_E is the Einstein radius (Perryman, 2011).

2.3 Light curves

The phenomenon of microlensing occurs when an object happens to move in front of the source and results in the change of magnification. In microlensing events there is always a relative motion of the source, lens and observer implying the time dependence of the angular separation between the source and lens. This also leads us to say magnification is also a function of time. The lens-source motion as a result of uniform motion can be parametrized as:

$$u(t) = \{u_0^2 + (\frac{t-t_0}{t_E})^2\}^{\frac{1}{2}}, \tag{2.25}$$

University of Cape Town

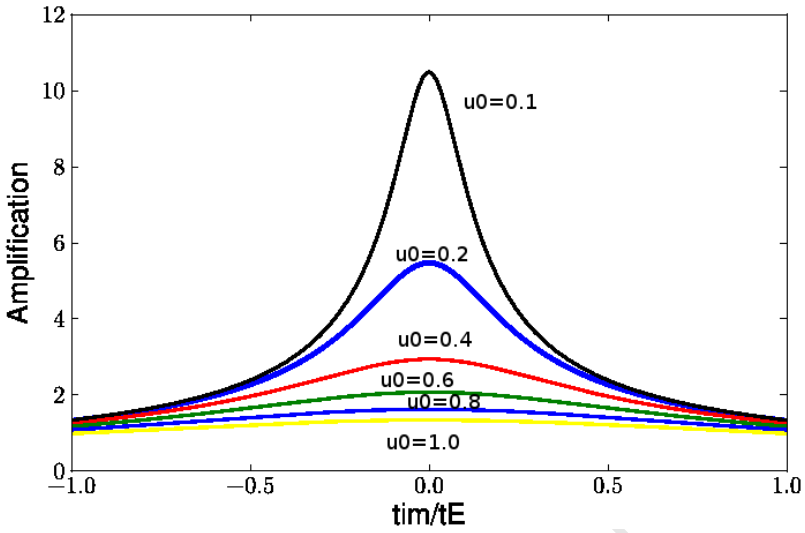

Figure 2.4: Light curves for point-source point-lens microlensing events with relative motion between the source and lens, for different impact parameters.

where u_0 is the is the smallest angular distance between the source star and the line of sight to the lens and t_0 is the time at the closest approach. Substituting equation 2.25 back to the total magnification equation given by Eqn.2.22 results

$$A(u(t)) = \frac{u_0^2 + \frac{(t-t_0)^2}{t_E^2} + 2}{\sqrt{u_0^2 + \frac{(t-t_0)^2}{t_E^2}} \times \sqrt{u_0^2 + \frac{(t-t_0)^2}{t_E^2} + 4}}, \tag{2.26}$$

where $t_E = \frac{D_L \theta_E}{V_\perp}$, u_0 is the smallest angular distance between the source star and the line of sight to the lens normalized in Einstein ring radius, t_0 the time of maximum amplification and the Einstein crossing time t_E, the time required to cross Einstein ring radius. The parametric equation in $u(t)$ with time gives a smooth and symmetric curve known as a *'Paczynski curve'* (Paczynski, 1996; Gaudi, 2010), which is the familiar point-source point-lens microlensing light curve shown in Fig.2.4

The figure above, Fig.2.4, shows the light curve for different impact parameters and we can see from the light curve that the smaller the impact parameter the higher the magnification would be and vice versa. The figure shown in Fig.2.5 demonstrates the relative tracks of the source and the two images (major, shown on the bottom side of the Einstein ring radius with black oval shape curves, and minor, smaller oval shapes shown inside the Einstein ring radius) with the source track shown in

University of Cape

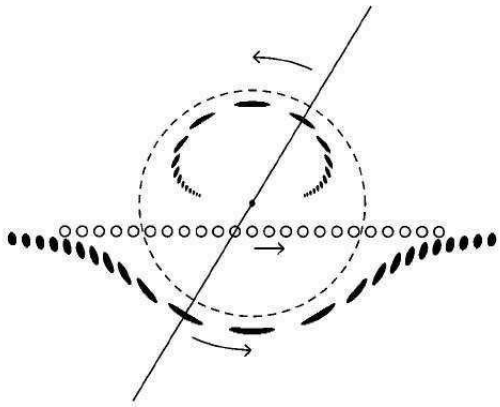

Figure 2.5: Picture showing the relative tracks of the two images, extended black oval shapes, lensing mass located at the center of the Einstein Ring, and the source positions also shown with small circles, Einstein ring shown with dashed line making circle (Adapted from Paczynski, 1996).

small circles passing across the Einstein ring radius. The big circle, Einstein ring radius, shown with dashed line.

University of Cape Town

2.4 Finite Source Effect

A point-source point-lens model which is parametrized by equation 2.26 is valid when the source size is small as compared to the Einstein ring radius and the impact parameter. However, if one of the cases mentioned fails, the light curve of the microlensing event will be affected. As Witt & Mao (1994) described, when the impact parameter u is very much smaller than the radius of the extended source ρ , $u << \rho$, the peak of magnification becomes larger. In the limiting case of the amplification equation stated in earlier sections as $u \longrightarrow 0$, the magnification for point-source point-lens goes to infinity, whereas the extended sources will have finite magnification.

Finite source effect was first investigated by Nemiroff & Wickramasinghe (1994). They demonstrated that if the impact parameter is smaller than the source radius, the central peak of the light curve is going to be modified and become wide and flattened as compared to the point-source light curves (Wambsganss, 2006). The finite source effect is also confirmed by observation later and among the observed microlensing events in the galactic bulge Witt (1995) estimated that 3% of the events are affected by the finite source effect. On the other hand, microlensing events with high magnification are also affected by finite source effect due to the smaller size of the impact parameter.

Alcock et al. (1997) observed finite source effects for the first time when the MACHO alert $95-30$ data was fitted, the light curve near the peak was found to deviate from the expected light curve. But for high magnification events this kind of deviation is common. He also described that the standard point-source point-lens model allows infinite magnification when the source and lens are perfectly aligned. When the extended source is considered the magnification is limited due to the fact that the entire source could not be aligned perfectly with the lens. Hence an extra parameter will be needed to model this type of microlensing event.

Studying finite source effect plays significant role in determining the size of the Einstein ring relative to the angular size of the source (Gould, 1997)(see also references therein) because θ_E constrains the physical properties of the lens (Yoo et al., 2004). The following two light curves Fig.2.6 and Fig.2.7 shows an event which is affected by Finite source effect for different microlensing events OGLE-2003-BLG-262 modeled by Yoo et al. (2004) and MACHO-1995-BLG-30 where this event is modeled by (Lee et al., 2009).

University of Cape Town

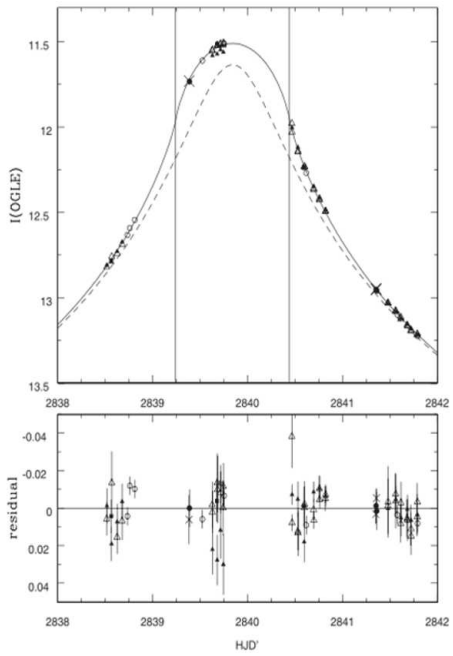

Figure 2.6: Light curve showing the microlensing event OGLE-2003-BLG-262 affected by finite source effect at its peak on 2003 July 19.34. Data points are collected using three different filters I (OGLE- open circles, μFUN Chile - open triangles, μFUN Israel- crosses), V(μFUN Chile -filled squares, μFUN Israel -filled circles) and H (μFUN Chile - filled triangles). The dashed line in the figure represents the light curve for point source point lens model (Adapted from Yoo et al. 2004).

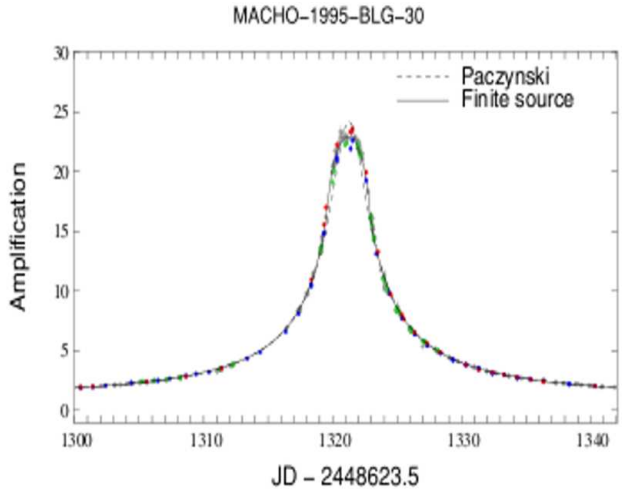

Figure 2.7: Finite source effect shown in the microlensing event MACHO-1995-BLG-30 assuming uniform source where the dashed line shows the point source model. Data points collected in R denoted by Red data points from MACHO, CTIO, UTSO, WISE, and grey points represent MJUO and, V are from MACHO points denoted in blue and UTSo labeled in green (Adapted from Lee et al. 2009).

2.5 Modeling Finite Source Effect

Gravitationally lensed extended sources have light curves which are different from the ordinary point-source point-lens microlensing events due to the flatness of the curve at the peak. In modelling the finite source microlensing light curve the total received flux is a combination of F_s, intrinsic flux of the magnified source star, F_B the background, unresolved flux from the observed target and is given by Rahvar & Dominik (2008):

$$F(t) = F_s A\{u(t); \rho, I\} + F_B, \tag{2.27}$$

where the finite source magnification $A\{u(t);\rho\}$ can be characterized by $(u_0, t_0, \omega_E = \frac{\mu}{\theta_E} = \frac{1}{t_E})$, u_0 is the impact parameter, t_0 the time at the closest distance, θ_E is the Einstein ring radius and t_E Einstein ring crossing time. Since our assumption regarding the source star is uniform bright source then the brightness profile function of the source $I = 1$,

$$F(t) = F_s A\{u(t);\rho\} + F_B, \tag{2.28}$$

where $u(t)$ is the lens-source separation assuming relative motion between the lens and the observer-source line-of-sight. The parameters we are looking for are: the impact parameter, u_0, the angular separation at the time of maximum amplification, the source radius ρ, the time it takes for a lens to cross a distance R_E, t_E, the time of maximum magnification, t_0, and the unlensed or base magnitude of the source (Peng, 1997).

University of Cape Town

3

Binary Lenses

University of Cape Town

It is a well established fact that the majority of the Galactic Disk stars are binaries (Mao & Paczynski, 1991) (and references therein) and hence observations toward these regions confirmed that a large fraction, 10%, of the lenses strongly display binary systems.

Gravitational lensing by two point-like masses is one of the most promising and active theoretical fields in gravitational lensing and hence attracts many authors, both theoreticians and observational astrophysicists. This is due to the the complexity of mathematics involved in the theoretical investigation of binary microlensing. This theoretical work has got emphasis after a pioneering work for the first time by Chang & Refsdal (1984) followed by Schneider & Weiss (1986) despite the fact that the latter never expected any to be detected (Gould, 2009), so as to study caustics in quasar macrolensing.

Caustics (refer chapter 4 for detail discussions) are indeed the new features of binary lensing as compared to point lenses. These are the directions in the source plane along which the amplification diverges or closed curves in the source plane where a point source is infinitely magnified. Chang & Refsdal (1984) also suggested that for an observed light curve in which this is apparently not the case, there are two

possibilities: the first opinion is 'Blending', light coming from another background source star or the system has more than two lenses.

In the second possibility, Schneider & Weiss (1986) also derived analytically the critical curves (refer Chapter 4 for further discussions) and caustics for binary lenses for a specific value of mass ratio $q = 1$ (the two lenses have equal mass) and found three different regions: close, intermediate and wide binary regions. We will give brief overview of these regions in the coming sections.

3.1 Basic Lens Equations in Binary Lenses

In the previous chapter we have explained the basic lens equation by point-mass lenses, which is characterized by its mass and its light curve also described by the distance of closest approach and the time of closest approach. In this chapter we are going to briefly explain binary lens equation and its properties.

When we are studying binary lenses, we should be aware of the complexity of the mathematics involved due to the presence of the second lens because the presence of the secondary lens introduces three new parameters. These new parameters are:

(a) The mass ratio $q = \frac{M_2}{M_1} \leq 1$ where M_1 and M_2 are masses of the binary components,

(b) The binary separation (source-lens projected separation in units of Einstein radius),

(c) The angle ϕ between the source trajectory and the line connecting the two lenses.

Now let us study the binary lens equation derived by Schneider & Weiss (1986). Consider two point masses M_1 and M_2 placed at a distance D_L from the observer on the lens plane (ξ_1, ξ_2), the plane perpendicular to the optical axis (line of sight), where the axis ξ_1 passes through the projection of the masses on the lens plane and choosing the origin to be in the middle of the line joining the two masses. Define the source plane coordinate system as (η_1, η_2), which is parallel to the lens plane, its origin is situated at the intersection of the optical axis and is D_{LS} distance from the lens shown in Fig. 3.1.

To derive the lens equation for the binary lens case, consider a light ray coming from a source where it is deflected by the gravitational field of the masses at a distance

University of Cape Town

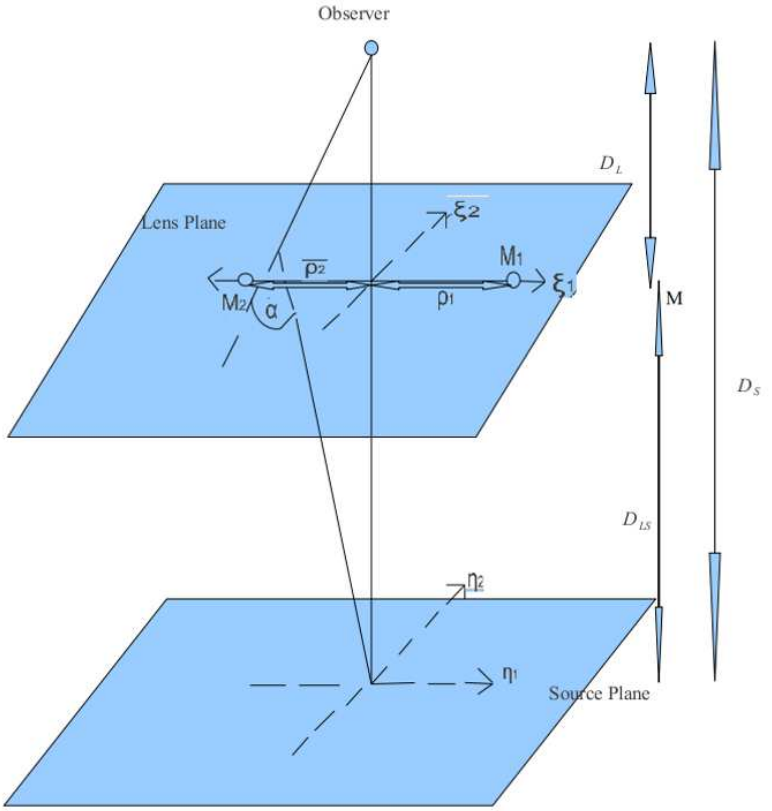

Figure 3.1: A schematic representation of gravitational lensing by two lenses, M_1 and M_2 located at $\rho_1$and ρ_2, respectively where D_L, D_s and D_{LS} are distances from lens plane to observer plane, observer plane to source plane and lens plane to source plane, respectively. α is the deflection angle, (η_1, η_2) are coordinates on the source plane and (ξ_1, ξ_2) are coordinates on the lens plane

.

d, assuming the closest approach distance $d >> r_s$ where r_s is the Schwarzschild radius. Schwarzschild radius, also known as gravitational radius, is a distance that defines the size at which a spherical astronomical object such as a star becomes a black hole. A black hole is an object so dense that not even light can escape the pull of its gravitational force. Even particles moving with the speed of light cannot escape the gravitational pull. Therefore, Schwarzschild radius, r_s, is the largest radius that a body with a specific mass can have and still keep light from escaping. This radius is given by

$$r_s = \frac{2GM}{c^2}. \tag{3.1}$$

From Fig.3.1 above, we can see that a light ray coming from a source is deflected by the two lenses M_1 and M_2. As Schneider & Weiss (1986)(and references therein) stated the total deflection angle due to the two lenses is the superposition of the two individual deflections and hence the total deflection on the lens plane at $\xi = (\xi_1, \xi_2)$:

$$\alpha(\xi) = \frac{4GM_1}{c^2}\frac{\xi - \rho_1}{|\xi - \rho_1|^2} + \frac{4GM_2}{c^2}\frac{\xi - \rho_2}{|\xi - \rho_2|^2}, \tag{3.2}$$

where ρ_1 and ρ_2 are the projection distances of the masses on to the lens plane. This system is no longer axially symmetric due to the presence of the second lens, which is responsible for the second term in the equation above (Wambsganss, 2006). As mentioned earlier, the new phenomenon encountered due to the presence of the second lens, asymmetric lensing, compared to the isolated point lens has some features such as the presence of extended caustics in the source plane, to be studied in the coming chapter and the two dimensional magnification distribution in the source plane. Our primary target in this section is to formulate the lens equation for the binary lens system. When a light ray coming from the source in the source plane η is deflected by the lens in the lens plane at ξ should satisfy the following condition so as to be observed by the observer:

$$\eta = \frac{D_S}{D_L}\xi - D_{LS}\alpha(\xi), \tag{3.3}$$

To make our approach clear it is necessary to define the Einstein ring radius, which is similar to the Einstein ring radius defined in the previous chapter for point-source point-lens model but the difference arises due to the mass. In this case we consider the total mass of the two lenses.

$$\theta_E = \sqrt{\frac{4GM}{c^2}[\frac{1}{D_L} - \frac{1}{D_S}]}, \tag{3.4}$$

University of Cape Town

where $M = M_1 + M_2$ is the total mass.

3.2 Complex Formalism of Binary Lens Equation

To make the binary lens formalism and computational work easier, we are now in a position to modify the equation and write it in complex formalism developed by Witt (1995). This type of representation will result in giving solutions separated as real and imaginary parts and hence leads to the parametric representation of the critical curves.

Witt (1993) stated that the complex formalism in microlensing lens equations is useful in some cases instead of the two-dimensional vectors because expressing the lens equation in complex formalism will allow one to find parametric representation of the caustics which enables to compute the whole caustic network of sample point masses. Another advantage of the complex formalism is that it reduces the conventional two dimensional lens equation in to one complex equation and this allows one to investigate more issues in lensing analytically (Witt & Mao, 1995). After saying this, it is easy to rewrite the lens equation in complex form by introducing complex formalism representation of the source and image positions as:

$$\zeta = \eta_1 + i\eta_2,\ z = x + iy. \tag{3.5}$$

Rewriting equation 3.3 using complex notation will give the following form

$$\zeta = \frac{D_S}{D_L} z + D_{LS}\alpha(z, \overline{z}), \tag{3.6}$$

where $\alpha(z, \overline{z})$ is the complex deflection angle. To understand gravitational microlensing in binary lens system, it is useful to work with angular variables defined in the complex plane (Mollerach & Roulet, 2002) then the simplified form of binary lensing equation in complex form is written as:

$$\zeta = z + \frac{\mu_1}{\overline{\rho_1} - \overline{z}} + \frac{\mu_2}{\overline{\rho_2} - \overline{z}}, \tag{3.7}$$

where $\mu_1 = \frac{M_1}{M}$ and $\mu_2 = \frac{M_2}{M}$ are mass fractions of the individual lenses and and $M = M_1 + M_2$ is the total mass, ρ_1 and ρ_2 are positions of the lenses, and $\overline{z}$ is

University of Cape Town

complex conjugate of z. All lengths are normalized by the Einstein ring radius given in the previous section for the total mass of the two lenses.

This equation can be written as a fifth order complex polynomial and hence it is impossible to find solutions analytically. But it is possible to get solutions using numerical methods, which gives us the position of the image z. This equation will give either three or five solutions depending on whether the source is inside or outside the caustics (Witt & Mao, 1995). Since the images resulting from microlensing cannot be resolved due to the small separations between individual images, the amplification can be obtained by the sum of individual amplifications of each image, A_j. These amplifications can be derived by the Jacobian of the transformation of the lens equation given above in Eqn.3.7 evaluated at the image position:

$$J(z,\overline{z}) = det \begin{pmatrix} \frac{\partial \zeta}{\partial z} & \frac{\partial \xi}{\partial \overline{z}} \\ \frac{\partial \overline{\xi}}{\partial z} & \frac{\partial \overline{\xi}}{\partial \overline{z}} \end{pmatrix}$$

$$A_j = \frac{1}{detJ}|_{z=z_j}, \tag{3.8}$$

$$detJ = 1 - \frac{\partial \zeta}{\partial \overline{z}} \frac{\partial \overline{\zeta}}{\partial \overline{z}}. \tag{3.9}$$

According to Chang & Han (2001), the fundamental geometrical difference between binary lenses and single point mass lens is the formation of caustics which can be seen by closer study and understanding of these amplifications. As the $det(J)$ approaches zero, with small perturbation on the light curve, there are regions in which the magnification becomes infinite and these places are known as caustics.

University of Cape Town

3.3 Binary Lenses with External Shear

Though this work does not give emphasis on lensing in the presence of external shear it is worthwhile mentioning its effect on gravitational lensing by binary lenses. When a microlensing event occurs in highly dense star fields such as in Galactic bulge, where microlensing targets are prominent, or in globular clusters, it is affected by the shear from the global distribution of mass near the lens star (Ryu & Park, 2007). A light bundle traversing a star field experiences shear due to the tidal forces produced by the stars (Schneider et al., 1992). Chang & Refsdal (1984), when they

developed the Chang and Refsdal model of microlensing, it was characterized by two factors 'Convergence' and 'Shear', where the convergence depends on the mass density within the beam and determines the magnification of the image whereas the latter depends on the mass distribution outside of the beam and determines the distortion of the image (Ryu & Park, 2007).

For a single lens microlensing event in the presence of shear, the total amplification has a shear term which results in a deviation of the light curve from ordinary single lens light curve. In the presence of shear the amount of deviation from the ordinary single lens is given by the excess magnification (Ryu & Park, 2007)

$$\delta A = A_\gamma - A_0, \tag{3.10}$$

where A_γ and A_0 represent amplification in the presence of shear and without shear respectively. As Ryu & Park (2007) described in their paper, comparison of the light curves with and without shear results the following:

(a) The presence of shear increases the deviation of the light curve from Paczynski curve whereas the impact parameter decreases;

(b) If the source trajectory is neither parallel nor perpendicular to the direction of the shear, then the presence of shear results asymmetric light curve;

(c) The magnitude of the shear produced by the globular clusters is of the order of 10^{-6} to 10^{-4}, which is difficult to observe this effect. In the future there is a possibility of detecting this shear using microlensing.

As Schneider et al. (1992) described the effect of the external shear in the binary lens equation will make the lens equation more difficult to solve analytically. The addition of the external shear also makes the algebraic equation which will give critical curves more complicated and hence the resulting caustics which can be obtained by transforming these critical curves will have self intersecting points that make the topology characterization of caustics more difficult. The mass ratio, q, of the lenses will not have any effect on the topology of the caustics if we exclude the external shear but the mass ratio has an effect on their size and detailed shape.

University of Cape Town

4

Caustics and Critical Curves

University of Cape Town

In this chapter we are going to introduce Caustics and Critical Curves in addition we are going to write the lensing equation in parametric form so that we can develop a FORTRAN program to get the solution of the lens equation.

The binary lens equation, developed earlier in the previous chapter, can be rewritten using the complex formalism for different masses of lenses assuming that the larger mass (primary) lens is situated at the origin, whereas the secondary is located at a distance d to the left:

$$\zeta = z - \frac{1}{1+q}\left(\frac{1}{\overline{z}} + \frac{q}{\overline{z}+d}\right), \tag{4.1}$$

where q is the mass ratio ≤ 1, d separation of the binary stars in units of the Einstein ring radius for the total mass $(m_1 + m_2)$. In this work we will adopt the method developed by Cassan (2008); Cassan et al. (2010).

As mentioned previously, single lenses are different from binary lenses due to the fact that the later generate caustic curves. It is obvious that the lens equation developed earlier is a mapping of the location of the point source ζ on the source

plane to the positions of its images at z on the lens plane. In the region of space $\phi \in [0, 2\pi]$, the caustic curve ζ can be parametrized as:

$$\frac{1}{1+q}(\frac{1}{z^2} + \frac{q}{(z+d)^2}) = e^{-i\phi}, \tag{4.2}$$

where z and ϕ satisfy the lens equation above (Cassan et al., 2010).

For a binary lens system (q, d), it is possible to find the numerical solution of the polynomial of fourth order assuming that a point source ζ is situated on the caustic and its point-like image z on the critical curve in the lens plane satisfies the previous equation. We can now simplify and rewrite the lens equation as a complex polynomial of degree four Cassan (2008); Cassan et al. (2010):

$$\frac{1}{z^2} + \frac{q}{(z+d)^2} = e^{-i\phi}(1+q). \tag{4.3}$$

This equation can be written as

$$z^4 + 2dz^3 + d^2z^2 - \frac{z^2}{e^{-i\phi}(1+q)} - \frac{2zd}{e^{-i\phi}(1+q)} - \frac{d^2}{e^{-i\phi}(1+q)} = 0. \tag{4.4}$$

After some algebra, the equation will reduce to

$$z^4 + 2dz^3 + (d^2 - e^{i\phi})z^2 - \frac{2de^{i\phi}}{1+q}z - \frac{d^2}{1+q}e^{i\phi} = 0. \tag{4.5}$$

This equation can be solved for a given value of ϕ and can have four complex solutions which result in caustic curves when ϕ runs from 0 to 2π. Here, we developed a FORTRAN program which can find numerical solution for Eqn. 4.5 for a given range of q, d and ϕ, where its solution is a complex number with real and imaginary parts. Using gnuplot I ploted the solutions of this equation to get the caustic curves shown below in green lines. I also developed a FORTRAN program which can find the solution for Eqn.4.1 by reading the solutions of Eqn.4.5. Hence the solutions of Eqn. 4.1 gives critical curves shown below in blue lines. In Figs. 4.1, 4.2, 4.3, 4.4 and the blue lines are therefore solutions of Eqn 4.1 whereas the green lines are solutions for Eqn. 4.5.

University of Cape Town

4.1 Critical Curves

As we mentioned earlier in the previous section the lens equation is a mapping from lens plane to source plane. This type of mapping is locally invertible at some images of the source. The lens mapping at some point can be invertible at all of its images when the source position does not lie on the caustic. A gravitationally lensed image may become very intensely magnified. This occurs when the source has a unique position with respect to a caustic curve that is either when it passes close to the caustics or crosses the cusp of the caustics. However, no gravitationally lensed image is ever really infinitely magnified because no real source is point-like. Critical curves are defined by the set of points in the space of observed angular positions for which the Jacobian determinant of the lens mapping vanishes (Dominik, 1999), i.e.,

$$det(\frac{1}{M}) = 0, \tag{4.6}$$

where M is the magnification.

4.2 Caustic Curves

The image curve under the lens mapping results in closed curves, which can intersect each other (Schneider et al., 1992). These curves are not smooth but can be understood in terms of folds of the sky sheet and sometimes they are joined in pairs at cusps (Mollerach & Roulet, 2002). Cassan et al. (2010) defined caustics as positions where the Jacobian determinant of the equation of lens mapping vanishes or lines of infinite point-source magnification.

Caustics are imaginary lines on the source plane of the sky where magnification diverges. Caustics can also be formed by the set of points in true source position space onto which the critical curves are mapped (Dominik, 1999). Detailed investigation of caustic curves is an important component in gravitational lensing theory due to the fact that the number of images changes by two (± 2) when the source passes close to the caustics or crosses the caustic. So studying the structure of caustic curves plays an important role in studying lens mapping as well as image multiplicity. Another important aspect in studying caustic curves is to investigate the amplification of a source. The amplification of a source, (Schneider et al., 1992), becomes large as a result of the area distortion of the lens mapping assuming that

University of Cape Town

the source is close to the caustics. In a gravitationally microlensed star by a lens system composed of two masses, the resulting light curve dramatically changes from symmetric one of a single lens system (Han & Hwang, 2009). This deviation occurs due to the formation of caustics for binary lensing system. Caustics of a pair of point masses may consist of a single continuous curve, or two or three separate components of curves due to its lens configuration (Schneider & Weiss, 1986) and (Erdl & Schneider, 1993). In the upcoming section detail discussion of the topologies of binary lenses due to different configuration of lenses will be discussed.

4.3 Topologies of Binary Lenses

Schneider & Weiss (1986) developed caustic curves for equal mass lens systems and showed that a binary lensing system displays in three different topologies, which are described as close binaries, intermediate binaries and wide binaries depending on the separation of the two lenses in units of Einstein ring radius, θ_E corresponding to the total mass as well as the mass ratio of the lenses $q = \frac{M_1}{M_2}$ (Dominik, 1999; Cassan et al., 2010; Gaudi, 2010).

(a) Close Binaries: According to Dominik (1999) and Dominik (2007), these types of binaries lie in the separation distance range $d < \frac{1}{\sqrt{2}}$. In this topology we obtain one big and two small critical curves inside the bigger one. The mapping of these critical curves results in diamond-shaped caustics with four cusps for the larger and two smaller triangular shaped caustics placed symmetrically on either side of the bigger caustic as shown in Fig.4.1 below.

University of Cape Town

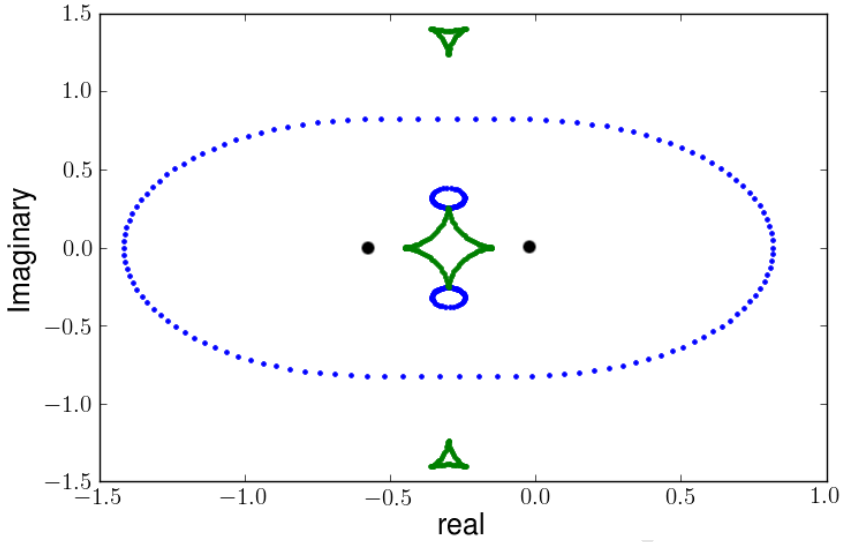

Figure 4.1: Critical curves shown with blue dotted lines and smaller blue circles and caustics shown with green line for Close Binary system with mass ratio=1 and separation distance = $\frac{1}{\sqrt{2}}$.The binary lens components are shown with black dots, on the right and left side of the central caustic, green diamond caustic, on the line passing through the origin and the center of the central caustic. The x and y-axes are the real and imaginary part of the solutions of equations 4.1 and 4.5. Where the primary star is located at the origin and the secondary situated at a distance $\frac{1}{\sqrt{2}}$ to the left. The axes are annotated in units of Einstein Radius.

(b) Intermediate (Resonant) Binaries: For binaries of equal mass lenses $q = 1$, $d = 1.414$ is the transition separation distance from close to intermediate binaries which is shown in figure 4.2. As the separation distance increases, the topology of critical curves also changes. In this region, $\frac{1}{\sqrt{2}} < d < 2$, the two smaller critical curves disappear and form one big critical curve and its transformation results with the formation of 6 cusp caustics. Resonant caustics are formed when the separation between the lenses is similar to the Einstein ring radius of the binary system (Han & Hwang, 2009).

University of Cape

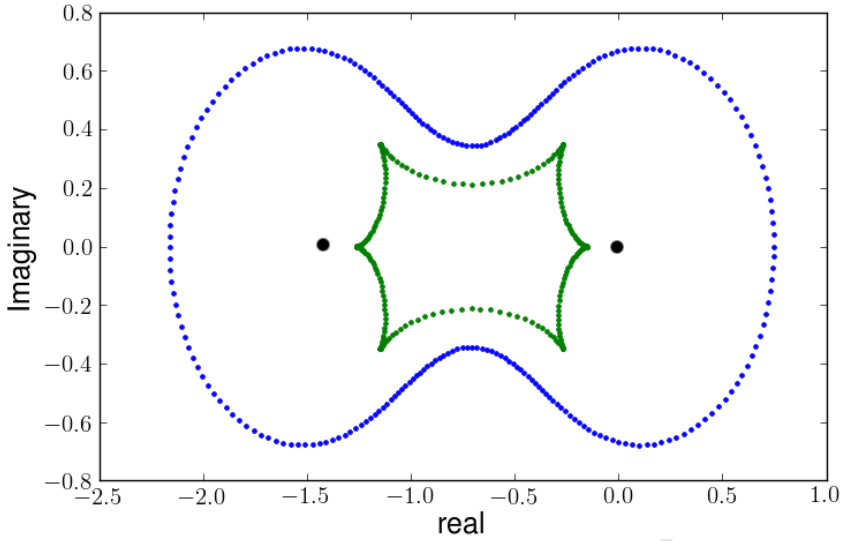

Figure 4.2: Critical and caustic curves for intermediate binary lensing with mass ratio = 1 and separation 1.414. Coloured points, black dots and axis units are as for Fig.4.1.

(c) Wide Binaries: If the binary separation increases further, $d > 2$, the topology of both critical and caustic curves change. The distance $d = 2$ is the transition of topologies from intermediate to wide binaries. In wide binaries the two critical curves, circular in shape, move further away and the two caustics move away and form a degenerate caustic (Dominik, 1999) as illustrated in Fig. 4.3 below. As separation increases the size of the caustics decreases. In this region it is also possible to assume the behavior of the lenses as two independent single lenses (Han & Hwang, 2009).

University of Cape

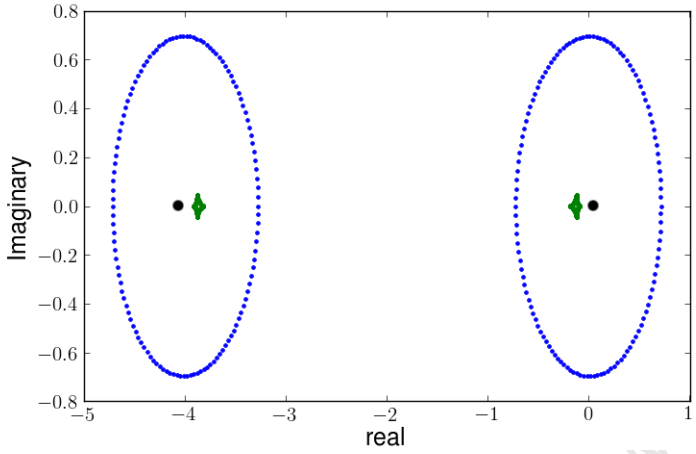

Figure 4.3: Critical and caustic curves for wide binary lensing with mass ratio = 1 and separation = 4 . Coloured points, black dots and axis units are as for Fig.4.1.

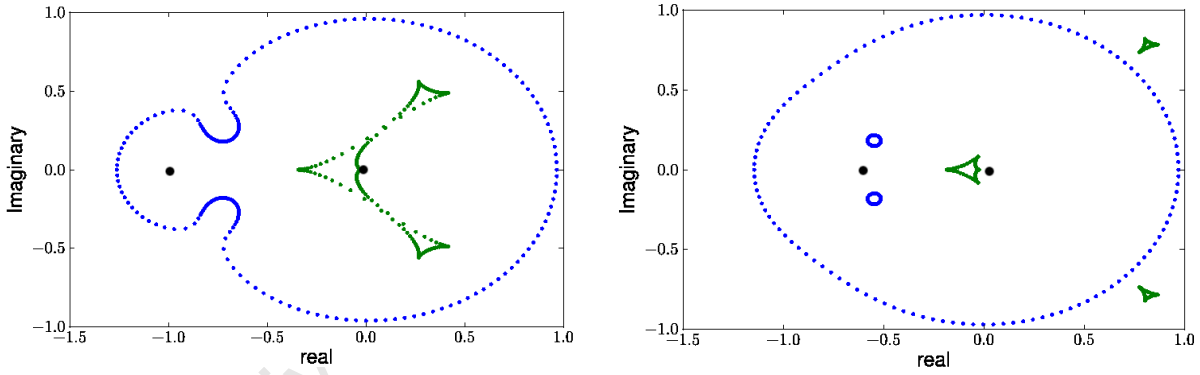

Figure 4.4: Left panel shows Caustic and Critical curves for $d = 0.8$ and $q = 0.01$ and right panel shows Caustic and Critical curve for $d = 0.6$ and $q = 0.01$. Coloured points, black dots and axis units are as for Fig.4.1.

The afore-mentioned topologies of critical curves and caustics will remain the same if we consider a different mass lens system ($q \neq 1$) but the mass ratio affects the caustics in size, position and the caustics will be stretched. The four different caustic and critical curve topologies shown in Figs. 4.4 and 4.5 demonstrate the variation in shape and structure due to the change in mass ratio and separation of the binary components.

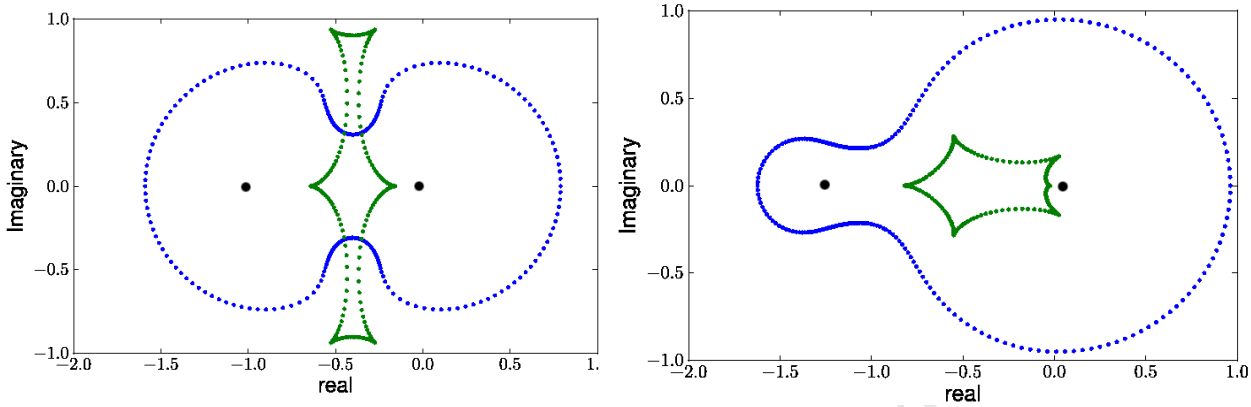

Figure 4.5: Left panel shows Caustic and Critical curves for $d = 1$ and $q = 0.8$ and the right panel shows Caustic and Critical curve for $d = 1.25$ and $q = 0.1$. Coloured points, black dots and axis units are as for Fig.4.1.

For an arbitrary value of the mass ratio (Schneider & Weiss, 1986; Erdl & Schneider, 1993; Dominik, 1999), the topology at which transition between the three regions occur which depends on the mass ratio and the lens separation distance (q, d) is the bifurcation value given by:

$$d_c^8 = \frac{(1+q)^2}{27q}(1 - d_c^4)^3, \tag{4.7}$$

$$d_w^2 = \frac{(1+q^{\frac{1}{3}})^3}{1+q}, \tag{4.8}$$

where $d_c(q)$ and $d_w(q)$ are transition distances between close and intermediate binaries and between intermediate and wide, respectively. Fig.4.6 shows the bifurication values in which transitions occur between close and intermediate as well as intermediate to wide binary configurations $d_c(q)$ and $d_w(q)$, respectively.

University of Cape Town

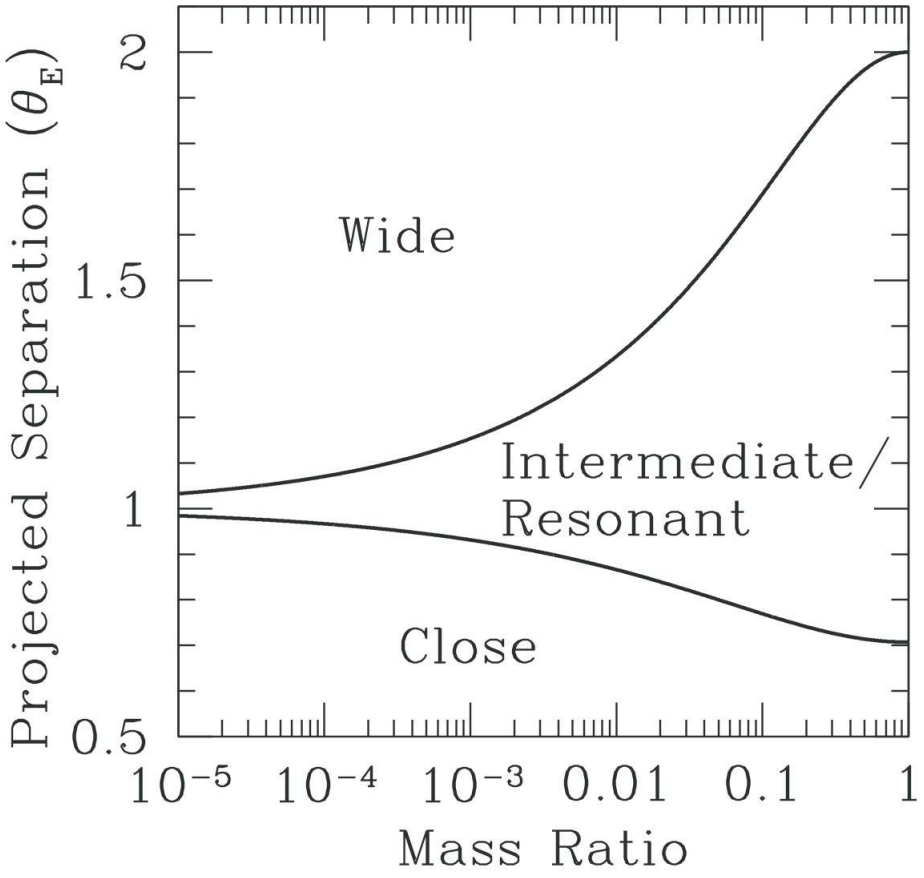

Figure 4.6: Figure showing the topologies of binary Lenses and bifurcation values $d_c(q)$ and $d_w(q)$.(Adapted from Cassan (2008, 2006), Gaudi (2011)).

4.4 Model Light Curves for Binary Lens

In this section, I will try to show some examples of model light curves developed for different mass ratio values and separation distances using a FORTRAN program and I used gnuplot for plotting the light curves as well as Dominik (2007) formalism. Modeling binary lens needs three parameters (t_0, t_E, and u_0) from the point source point lens model in addition three parameters from binary lens model (d, q, α) is required. This section presents some light curves and source track as it passes across the caustic curve for randomly selected values of binary lens parameters.

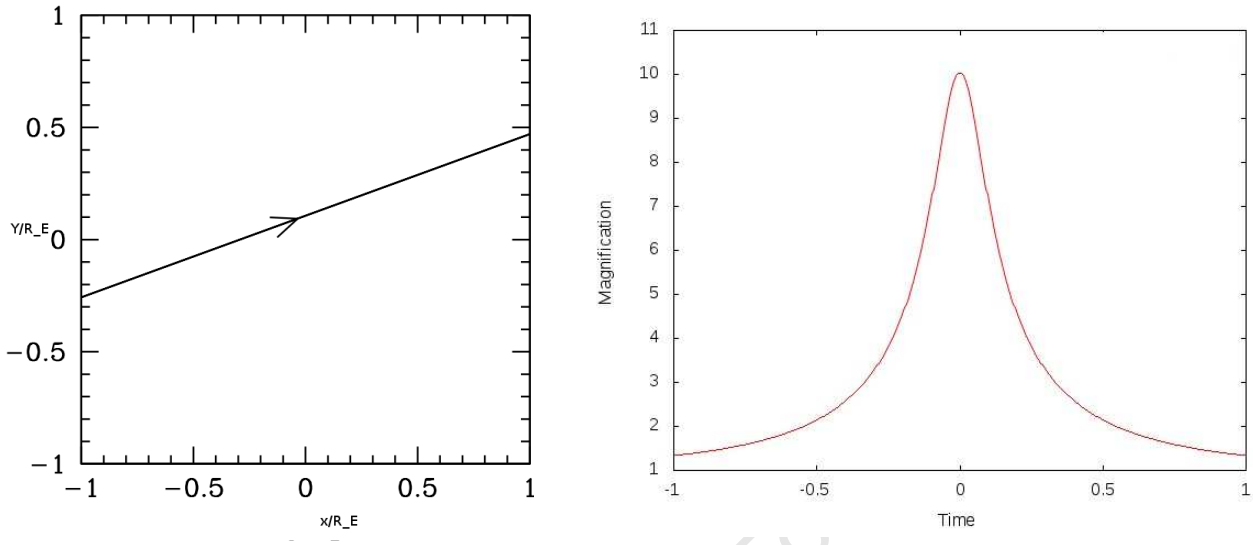

Figure 4.7: Left panel: Source passing far away from the caustic curve and the right panel demonstrates model light curve for a mass ratio of 0.5, and distance between components is 0.5.

The plot shown in Fig. 4.7 left panel shows the source path and the right panel shows the resulting light curve due to the effect of the source passing across the face of the caustic curve and its path is 20^o from the binary axis. It is clear from the light curve that this light curve looks like a single lens microlensing effect due to the fact that the source is passing far away from the caustic curve.

University of Cape To

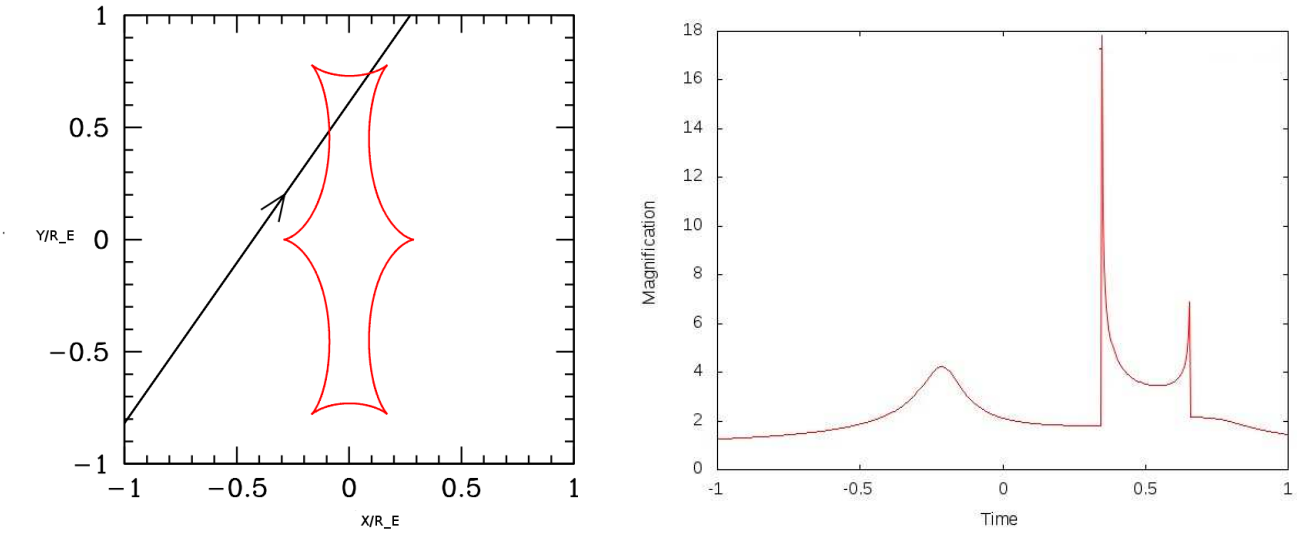

Figure 4.8: Left panel: Caustic curve structure and source path at an inclination of 55^o from the binary axis for a mass ratio of 0.99 and binary component separation distance of 0.9, Right panel: Light curve produced due to the source crossing the caustic curve for model binary lens shown in the left panel.

The left panel in fig.4.8 shows the caustic structure (red curve) and source path shown in straight line. The light curve produced is due to the effect of the source crossing the caustic curve. As the source getting closer to the cusp the first small hump is produced in addition as the source crosses the caustic curve, the magnification becomes higher and we get the sharp peak. As the source passes inside the caustic curve the magnification decreases as it is shown in the light curve shown in the right panel of fig. 4.8. The second peak is obtained when the source crosses the caustic curve as it leaves the caustic curve and finally the magnification decreases as time passes.

The left panel in fig. 4.9 shows the caustic curve and source track for a binary lens with mass ratio of 0.99 and the direction of the source path is -230^o. The only difference between the left panels of previous plots in Fig. 4.7, 4.8 and this plot in Fig. 4.9 is the direction of motion of the source.

The caustic curve (red line) generated in Fig. 4.11 is for a mass ratio of 0.5 and separation distance of 0.7 and the direction of the source motion is -30^o. The light curve produced due the effect of the source as it passes across the caustic curve. The sharp increase in the magnification is because the source enters to one of the

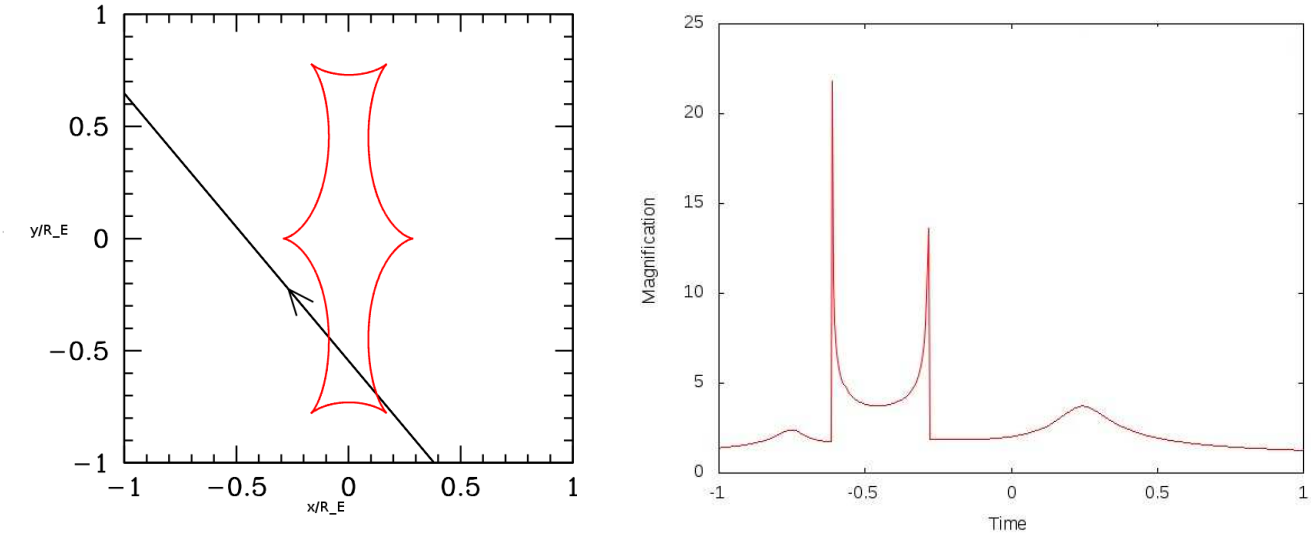

Figure 4.9: Left panel: Caustic curve(Red diamond) produced for given mass ratio of 0.99 and source track., Right panel:The light curve produced for a binary lens system with mass ratio 0.99 and distance between binary components is 0.9

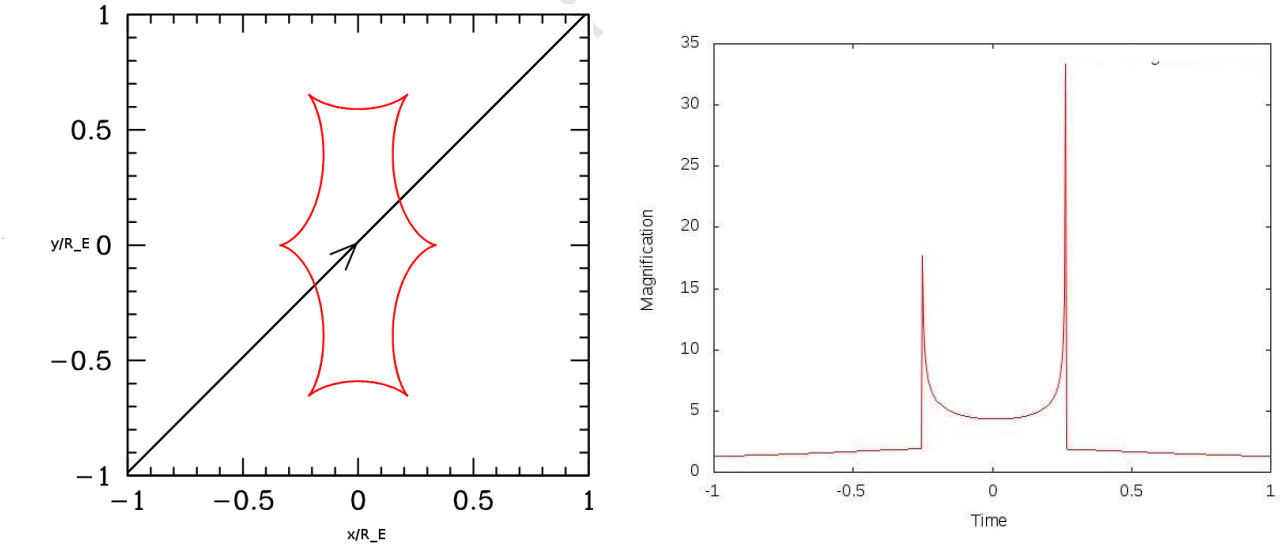

Figure 4.10: Left panel:Plot showing Caustic curve and source track at a direction of 45^o generated for mass ratio 1 and binary component separation distance of 1, Right panel: Model light curve produced due to the effect of the source passing through the caustic curve shown in the left panel.

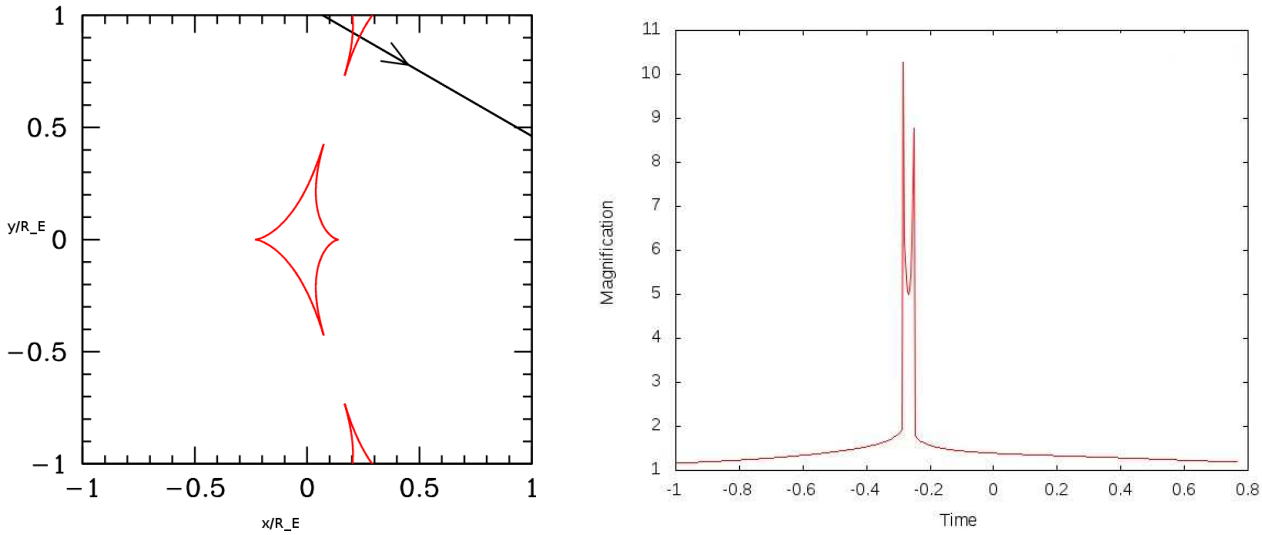

Figure 4.11: Left panel: Caustic structure (shown in red) for given mass ratio of 0.5 and separation distance between binary components 0.7 and a source track (shown in straight line)., Right panel: Model light curve produced for a binary lens system shown in the left panel.

caustic curves and stays for a short duration due to the small size of the caustic and the next sharp increase occurs when the source leaves the caustic curve.

The light curve produced looks a single lens microlensing event except when the source passes very close to one of the caustic curves which results in a short duration hump on the light curve. So, what we can learn from this section is that it is possible to generate different kinds of binary lens models based on different parameters necessary to express binary lens microlensing events. For a certain value of mass ratio and separation distance if we take the direction of the source track in clockwise direction, the light curve that we get is the mirror image of the light curve produced using anticlockwise direction of the source track as it is shown in figs. 4.8 and 4.9.

University of Cape Town

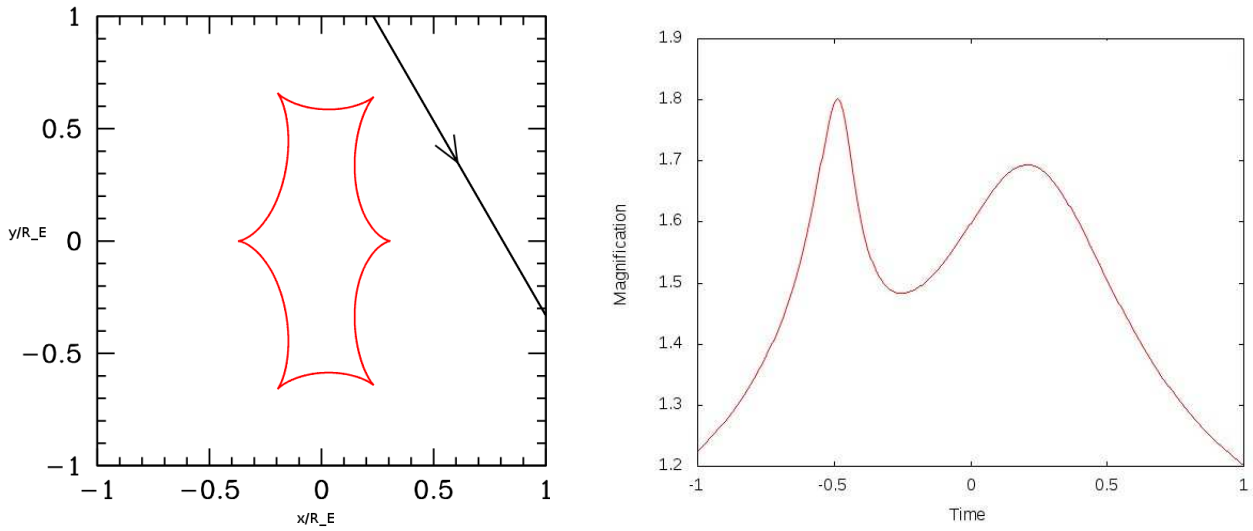

Figure 4.12: Left panel: Caustic curve generated for a binary system of mass ratio 0.8 and separation distance of 1., Right panel: Binary lens model light curve produced for a binary mass ratio of 0.8 as the source passes across the caustic line shown in the left panel.

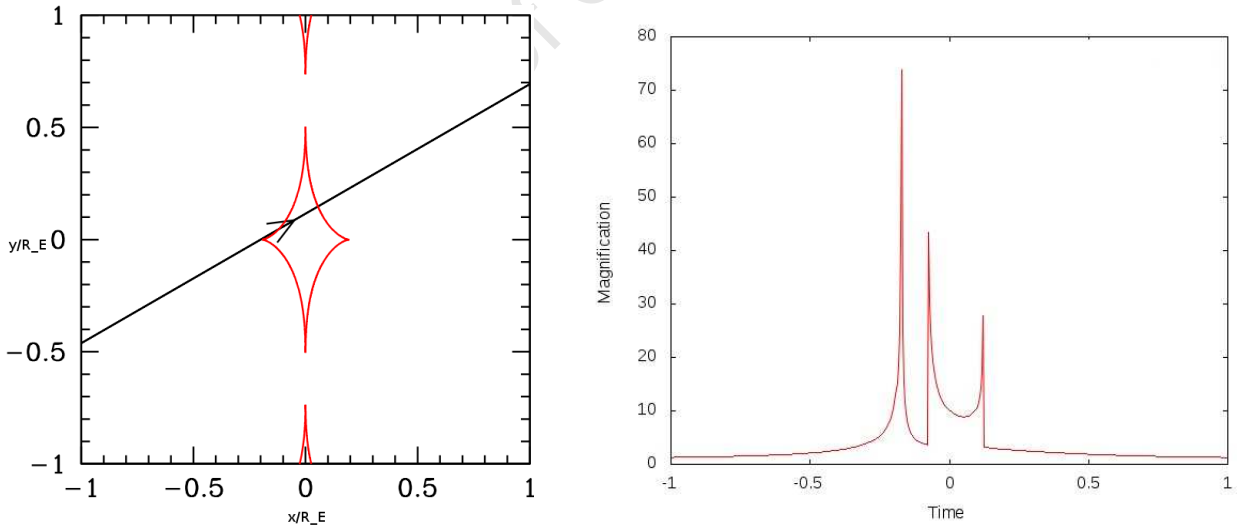

Figure 4.13: Left panel: Caustic curve plotted for a binary lens system of mass ratio 1 and separation distance of the binary components 0.7 where the direction of the source track is at angle of 30^o shown in black straight line., Right panel: Light curve produced for a binary lens system of caustic structure shown in the left panel. The magnifications are due to the effect of the source as it crosses the caustic curve.

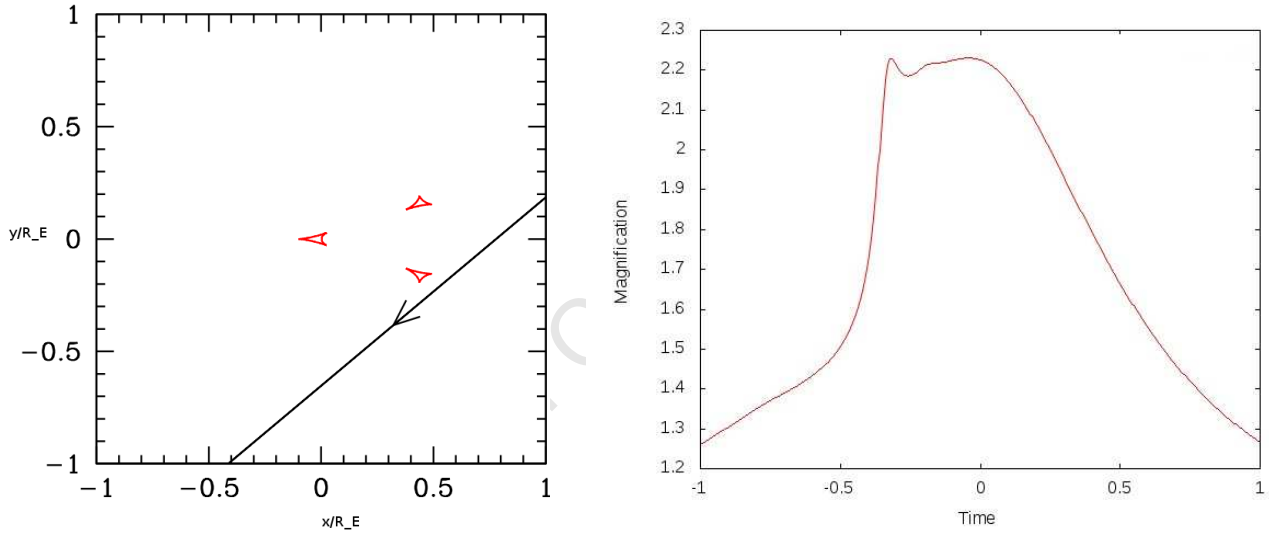

Figure 4.14: Left panel:Caustic structure (shown in red) for given mass ratio of 0.01 and separation distance of 0.8, direction of source track is at an angle of 220^o from the binary axis., Right panel: Model light curve generated due the effect of the source as it passes across the caustic curve as shown in the left panel.

5

Microlensing in Searching for Extrasolar Planets

University of Cape Town

One of the methods to detect distant planets by monitoring microlensing events in the galactic bulge is Gravitational microlensing. This method needs intensive monitoring of microlensing events towards a dense field such as the Galactic bulge. Mao & Paczynski (1991) first pointed out that from observations toward the Galactic Bulge, where the source is 8kpc and the lens is 2kpc from the source, the size of the Einstein ring in the lens plane to be:

$$\theta_E \simeq 1.9AU\sqrt{\frac{M_L}{0.3M_\odot}\frac{D_L}{6kpc}\frac{D_{LS}}{2kpc}\frac{8kpc}{D_S}}, \tag{5.1}$$

where M_L is mass of the lens, D_L,D_{LS} and D_S are observer plane-lens plane, lens plane-source plane and observer plane-source plane distances respectively.

In studying binary lenses, a particular lens case consists of a planet and a star, the case shown in Fig.5.1 below, where the planet orbits the star. These types of microlensing events have special features like the mass ratio $q = \frac{M_p}{M_*} << 1$ where

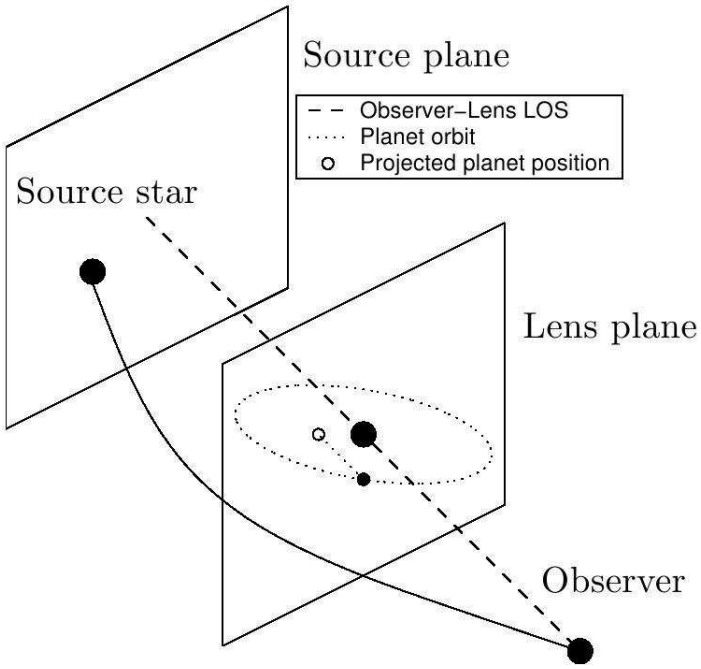

Figure 5.1: Geometry of microlensing event composed of a planet and a star in which light coming from the source is deflected by the gravitational potential of the lens system.(Adapted from Rattenbury (2006)).

University of Car

M_p and M_* are the masses of the planet and the planet host star respectively. The presence of the planets can be seen in the light curve due to its perturbation on the magnification as well as the presence of anomalies in the light curve.

Intensive monitoring of planetary microlensing events will lead to a deviation of the light curve as shown in Fig.5.2. The light curve in the upper panel is equivalent to single lens microlensing events and the lower panel is similar to the single lens model but for a short period of time it deviates from single lens and shows a behavior of binary lens light curve.

The sensitivity of microlensing in searching planets depends on the planet-star separation. The region between 0.6 to $1.6\theta_E$ is the peak for detecting planets and we call this region Lensing Zone. As Han et al. (2009) derived an analytical expression for planetary separation (Lensing Zone) which can be detected through high magnification events as:

$$|\sqrt{\frac{2q}{\rho_*}} - \sqrt{\frac{2q}{\rho_*} + 1}| \leq d \leq \sqrt{\frac{2q}{\rho_*}} + \sqrt{\frac{2q}{\rho_*} + 1} \tag{5.2}$$

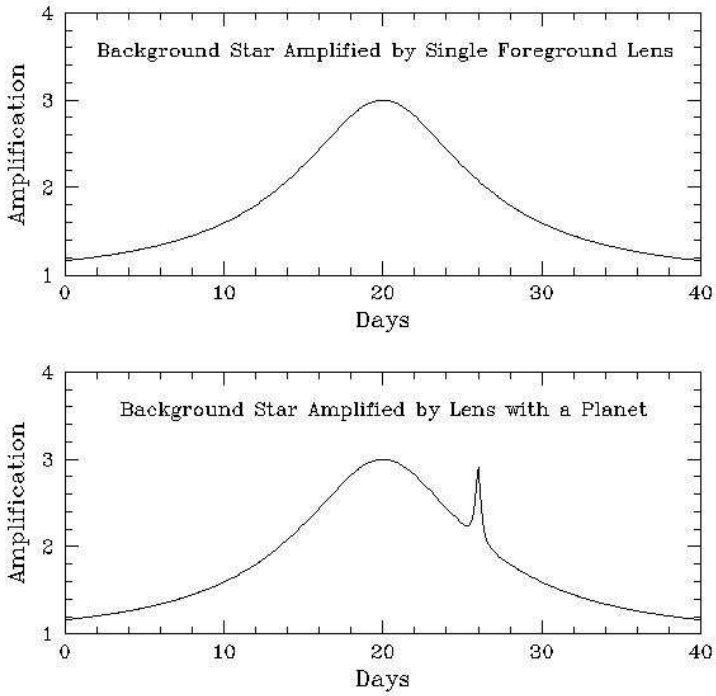

Figure 5.2: Light curve of microlensing events: Top panel shows light curve produced by single lens giving smooth and symmetric curve. Bottom panel:Light curve produced in the presence of planet. The small deviation is caused by the planet which acts as a lens and magnifies the background source and hence leaves a short duration peak.(Adapted from PLANET microlensing collaboration Home page: http://planet.iap.fr/planet.html).

and they also demonstrated that the lensing zone of central perturbations is different for different mass ratios which is different from the classical lensing zone where this is not affected by the mass ratio.

Table 5.1: Lensing zones for galactic lenses (Adapted from (Sackett, 1997))

Lens Type	Disk lens (4Kpc)	Bulge lens (6 Kpc)
$1.0M_{\odot}$ Disk	2.4 - 6.4 AU	2.1 - 5.5 AU
$0.3M_{\odot}$ Bulge Dwarf	1.33 - 3.5 AU	1.1 - 3.0 AU

5.1 Planetary Caustics

Binary lens caustic structure is determined by two parameters, the mass ratio $q = \frac{M_p}{M}$ and angular separation of the lenses. For arbitrary mass ratio, Ehlers & Schneider (1993) determined the separation of lenses for which transition between these topologies occurs. As we explained earlier planets can be detected by microlensing technique in two different ways. The first case is when the background source star crosses the planetary caustics where these events can create extended caustics (one central and large planetary caustic). When a source passes across these caustic lines, there will be a change in magnification. The total area of these curves is very small as compared to the surface of the Einstein ring disk. But the presence of the planets can be revealed on the light curve if the source approaches very close to or crosses the planetary caustics. These events basically can happen at lower magnification as well.

The second scenario occurs when a lens crosses a source star very close to the line of sight where the distance of closest approach is much smaller than the Einstein ring radius implying high magnification of the source (Rattenbury, 2009). In the second panel of Fig. 5.2 the planet is acting as a microlens and results in the distortion of the magnification pattern and hence results in a hump in the light curve due to the fact that a planet located in the "lensing zone" of its parent star may result in perturbed regions of high magnification, including infinite magnification on caustics (Sackett, 1997). So, if a background source passes through this region, it will result in a short time deviation or anomaly on the light curve.

University of Cape Town

5.2 Observational Evidence of Microlensing Events

The idea that a star's gravitational field affects the light coming from a background source, so-called gravitational microlensing, was first pointed out by Einstein in 1936 and further studied and developed by Refsdal (1964) and Fukui et al. (2007). This event was difficult to observe due to its rare occurrence. So, for this type of observation to have significant importance in microlensing studies, systematic searches are required. The more advanced the search of targets and the more stars observed, the higher the probability of observing microlensing events. Then using advanced observation tools the search for gravitational microlensing became successful since the pioneering theoretical work by Paczynski (1986). He suggested that

this technique can be used as a tool to detect Massive Astronomical Compact Halo Objects (MACHOS) in the galactic halo (Ryu & Park, 2007). Paczynski (1986) also first estimated realistic rates for microlensing toward crowded stellar fields, such as Large and Small Magellanic Clouds and Galactic Bulge (Paczynski, 1991), to study galactic structure, extrasolar planets and galactic dark matter.

Systematic searches focus on searching for microlensing event targets toward dense stellar fields such as the galactic bulge. For these targets the observation season is limited from May to September.

As a result of intensive observation, the first microlensing event candidates were discovered by three independent collaborations: MACHO (Alcock et al., 1993); OGLE (Optical Gravitational Lensing Experiment) (Udalski et al., 1992); EROS (Experience pour la Recherche d'Objets Sombres) (Aubourg et al., 1993).

After this breakthrough thousands of microlensing events have been detected, mostly toward the galactic bulge. Among the collaborations, OGLE (Fukui et al., 2007) detected almost 600 events each year. Developments in equipment and assignment of dedicated telescopes increased possible detection of microlensing targets to more than 1000. Searches of microlensing events in recent times have also been extended towards the Andromeda galaxy, toward spiral arms and toward globular clusters (Mollerach & Roulet, 2002). Moreover, collaboration of different telescopes around the world have been created to establish networks so that events are going to be observed in real time and alerted to the microlensing community for followup observation (Mollerach & Roulet, 2002).

University of Cape Town

5.2.1 Groups Working on Microlensing Observations

This section is dedicated to give an overview of microlensing observation groups. More emphasis is given for groups working in collaboration with the South African Astronomical Observatory. Those groups are characterized by searching microlensing targets toward the Galactic Bulge (Moniez, 2010).

(a) PLANET (Probing Lensing Anomalies NETwork, (Albrow et al., 1998)) Since the establishment of the PLANET consortium in 1995, this group has played a major role in photometric followup of ongoing events. Its primary aim is to perform precise and frequent multi-band observation of ongoing microlensing events. PLANET collaboration is a followup network as shown in Fig.5.3 and

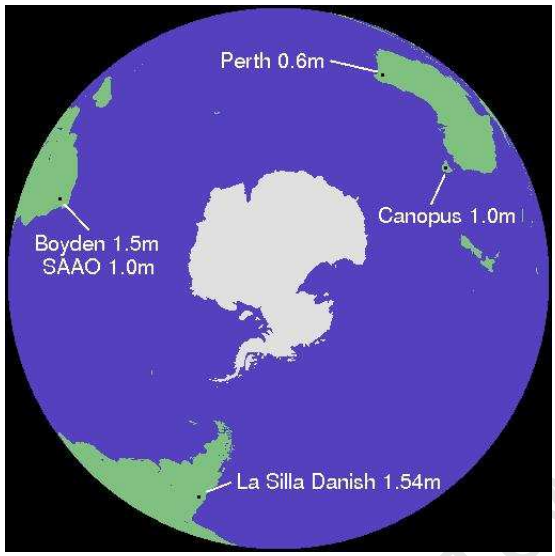

Figure 5.3: PLANET collaboration in the southern hemisphere (Adapted from Zub(2009))

University of Cape Town

mainly monitors signatures alerted by OGLE and MOA. PLANET collaboration has following targets alerted by MACHO and EROS as well before 2001 using the four telescopes located in the southern hemisphere: SAAO (1m telescope located in Sutherland, South Africa), Danish 1.54m telescope (La Silla, Chile, South America), Canopus Telescope, Tasmania, Australia, Perth 0.6m to get 24 hour continuous followup observations of several targets. In addition the Boyden observatory (Bloemfontein, South Africa) was briefly part of the network. As discussed earlier in Section 5.2, intensive follow up is crucial to observe and study short-lived binary lens events, such as caustic crossing events and planet detection. Observations towards the Galactic Bulge by PLANET usually start in April and end in September because the bulge is visible from the southern hemisphere.

Each night selected targets are monitored by observers with high precision photometric observations around the consortium and data is collected at each telescope and the data is reduced online to be sent to the central server located in France.

(b) MicroFUN (Microlensing Followup Network)

MicroFUN group is a consortium of professional astronomers as well as amateurs from around the world dedicated to follow-up observations toward the Galactic Bulge and gives more emphasis to high amplification microlensing events which in turn lead to the potential detection and discovery of planets. In early 2009, MicroFUN formed a working group with PLANET to enhance their effort in identifying high magnification events and also to use a large telescope network which allows greater sampling of the light curve giving the microlensing campaign more sensitivity to short period microlensing events. In this group the equipment ranges from a 0.25m telescope and basic CCD in Perth to the 2.4m telescope at Kitt Peak National Observatory (KPNO).

Once targets are selected and an alert is set, astronomers all over the consortium will follow up targets and then upload the data to the MicroFUN headquarters for photometric processing and PSF (Point Spread function) fitting photometry (McClelland, 2008). The main reason behind sending the data to one central office is to do the analysis with the same software and results appear in a uniform fashion. Taking into account the results of the data processing events with special features which are intensively observed and made ready for further detailed photometric time-series analysis using difference imaging.

University of Cape Town

(c) OGLE (Optical Gravitational Lensing Experiment, (Udalski et al., 1992))

OGLE was established in 1992 and is based at Warsaw University. It works in collaboration with the Las Campanas Observatory (Chile), Princeton University and the Carnegie Institution. The original objective of OGLE was to search for dark matter in the Magellanic Cloud and Galactic Bulge using the microlensing technique but now it concentrates on searching for extrasolar planets towards the Galactic Bulge and to study variable stars. Their main purpose is to identify targets and announce target events to the microlensing community so as to alert the observers (followup Networks).

OGLE historically had four phases. The first phase, OGLE-I, was the pilot project phase and ran through $1992-1995$ using the Swope 1m telescope at the Las Campanas Observatory. In the second phase, OGLE-II, $(1996-2000)$, the group built a 1.3m Warsaw telescope dedicated only for this project. Then the third phase, OGLE-III, in 2001 started observation using the newly constructed second generation CCD mosaic camera with an 8 chip 8192×8192 pixel mosaic with 15μm size giving a full field of view 35×35 arcmin (Udalski, 2003). Since the data flow is too much photometric reductions are performed in real time to avoid saturation (Udalski, 2003).

OGLE-III monitored Galactic bulge, the constellation of Carina and toward Large and Small Magelanic Clouds observing more than 2 million stars. The most recent development in OGLE phase came in 2010, OGLE-IV, after some engineering work in 2009 and started functioning with 32-chip mosaic CCD camera. Its main objective is to increase the number of planetary detections using microlensing.

(d) MOA (Microlensing Observation in Astrophysics) It is a collaboration of astrophysicists from New Zealand and Japan where its main research center is located at Mt. John, Tekapo, New Zealand. This group uses a 1.8m reflector telescope to monitor around 10 million stars toward the Magellanic Clouds and Galactic Bulge. They use gravitational microlensing technique to detect dark matter, extrasolar planets and study stellar atmospheres from the southern hemisphere. MOA focuses on searching for gravitational microlensing events with high magnification which are sensitive to the presence of extrasolar planets. As McClelland (2008) stated every extrasolar planet discovered using gravitational microlensing has some observational data from MOA.

University of Cape Town

In the following table, we summarize the different groups working on microlensing and their followup targets.

Table 5.2: Microlensing survey groups, their targets and the approximate number of events observed in different directions, as well as their running period (Adapted from Mollerach, 2002)

Observing Groups	Targets	Events	Years
MACHO	Bulge	350	$1992-1999$
	LMC	25	
	SMC	2	
OGLE I	Bulge	20	$1992-1995$
OGLE II	Bulge	520	$1996-2000$
	LMC	1	
	SMC	1	
OGLE III	Bulge		$2001-$
	SMC		
	LMC		
OGLE IV			2009-
EROS I	LMC	4	$1991-1995$
EROS II	LMC	1	-1997
	Bulge		
	Spiral arms	7	
DUO	Bulge	13	$1994-1994$
MOA	Bulge	20	-2000

Table 5.3: Followup networks (Adapted from Mollerach, 2002)

PLANET
MPS
GMAN
MicroFun
MindStep
MOA

University of Cape Town

5.2.2 Binary Lens Observation

The theory of binary lenses was extensively studied by Schneider & Weiss (1986) and Paczynski (1986) for a specific value of mass ratio ($q = 1$). This great work paved the way for observers to find signals of binary lenses and in the microlensing observing season in 1993 the first binary lens was detected with some special features having two peaks and labeled as an 'unusual' event (Wambsganss, 2006). This target was observed by OGLE. Among the OGLE microlensing candidates, OGLE No.7 showed unusual variation in amplification which is different from the variations of the known variable stars but the variation in amplification was similar to the theoretical light curves developed for microlensing by binary lens (Mao & Paczynski, 1991).

The light curve in Fig. 5.4, top panel shows (V-I) V_s HJD and lower panel shows I (magnitude) with time (Julian Date) of OGLE No.7 in the 1992/1993 observing campaign. The V-I calculation is very important in determining the type and properties of the source star, by observing the target using two bands I and V. Microlensing observations are affected by blending that occurs due to the additional light coming from a close companion of a lensed star or from the binary lens itself. According to (Udalski et al., 1994) in the 1992 observing season OGLE No.7 had constant brightness I$\sim$ 17.5mag and resulted in categorizing this event as a non-variable star but in the coming year observing season there was a dramatic change in brightness which rose by 2 mag and reached 15.1 mag, then after reaching maximum brightness it started to fade and then became dimmer and instantly it showed a rise in brightness followed by a decrease in brightness. From this observation it was clear that OGLE No.7 had two maximum brightness and analysis of the light curve resulted in binary microlensing event not a cataclysmic variable or low mass x-ray binary or Dwarf Novae because its duration was much longer than the typical dwarf novae outbursts or supernovae outbursts (Udalski et al., 1994). The arguments raised to classify OGLE No.7 as binary lens event was based on, (Mao & Paczynski, 1991), statistical reasoning stating from OGLE events around 10% is expected to be binary and from observed 10 bright star samples one could possibly be binary. The other argument is the color of OGLE No.7 showed the star was typically Galactic Bulge main sequence turn off point star (Udalski et al., 1994).

University of Cape Town

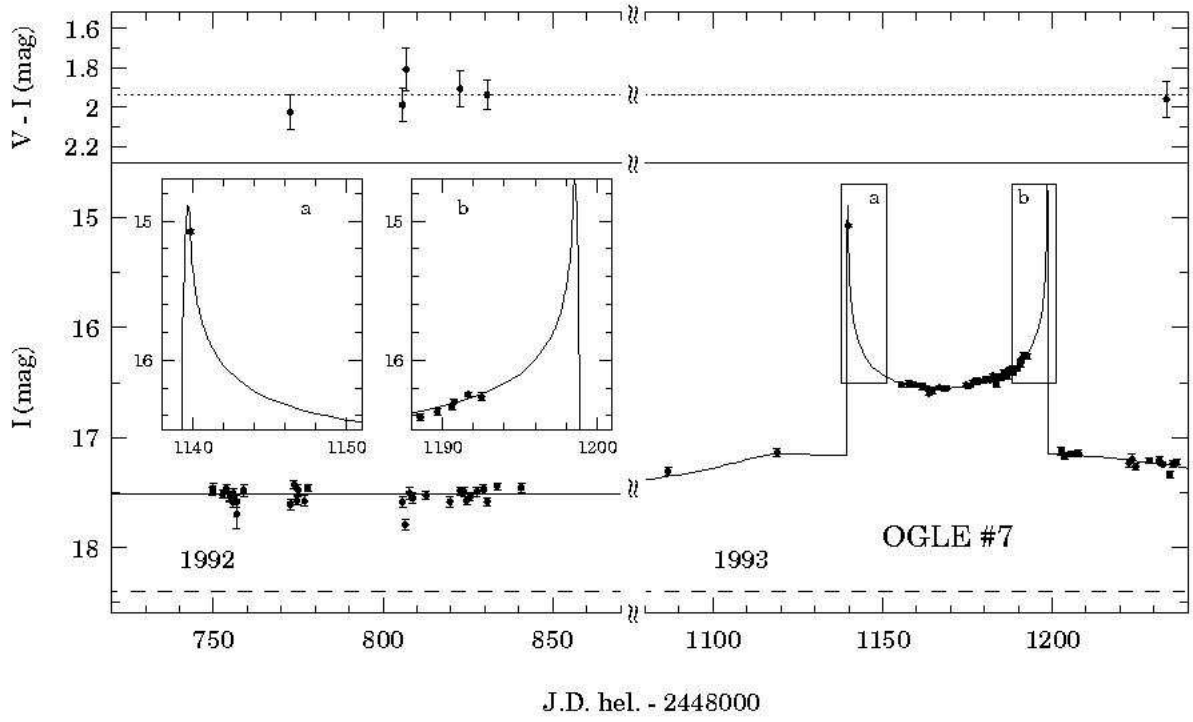

Figure 5.4: OGLE7, The first binary Microlensing event observed with mass ratio $q = 1$ separated by one Einstein radius Udalski et al. 1994 (Adapted from Udalski et al. 1994).

OGLE No.7 (Udalski et al., 1994) had two caustic crossings and its modeling was done by Mao & Di Stefano (1995). Fig.5.5 shows the structure of the caustic and critical curves with the source path. The source crosses the caustic curve at two points. Fig.5.4 demonstrates the theoretical model of the light curve developed for OGLE No.7 .

University of C

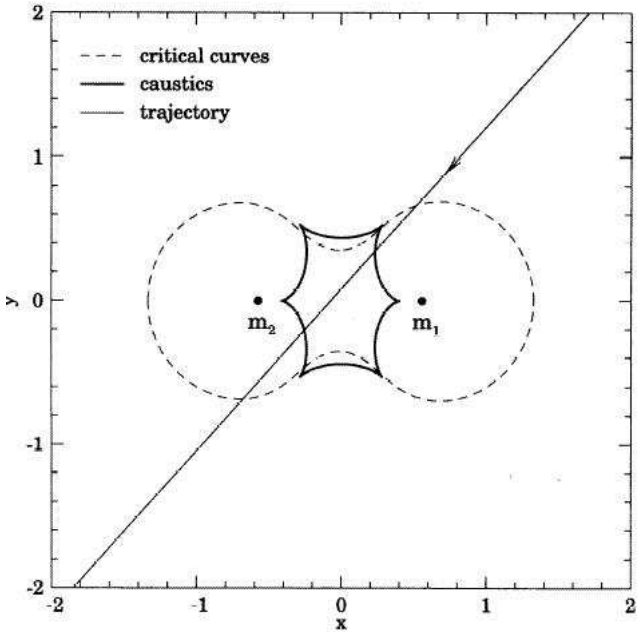

Figure 5.5: OGLE No.7 Geometry of the best fit binary lens model: The dashed line represents the critical curves and the solid line shows the caustics projected on the source plane. The straight line shows the trajectory of the source moving in the direction shown by the arrow (Adapted form A.Udalski et al.(1994)).

But in some cases, the available data is insufficient to distinguish and characterize binary and single lenses (Jaroszyński et al., 2004), more importantly when we try to study more detailed parameters of the lens system.

The improvement in the data reduction systems of groups working in microlensing allows observation of microlensing events in real time. In the 1998 microlensing campaign, MACHO-98-SMC-1 was the first caustic crossing binary microlensing event to be observed in real-time, which allows results in concentrated photometric and spectroscopic followup of observations (Alcock et al., 1999).

During followup of this target, a sudden increase in brightness by 1.5 magnitude was recorded, in which photometry from subsequent nights confirmed that the target was likely to be caustic crossing event. During that time alerts were sent to the microlensing working groups giving them the opportunity to make the first real-time detection of binary lensing microlensing event towards the Small Magellanic Cloud(SMC) (Alcock et al., 1999)(and references therein). The challenge here was finding a way for accurate prediction of the time for the second caustic crossing.

Continuous observation allowed an estimate on the date of second caustic crossing to be on June 19.3 ± 1.5UT to be issued June 15.3. Later data from June 15 made this time approximation to be revised and estimated to be June 19.2 ± 1.5UT. June 17 data provided information about prediction time to be June 18.2 when the second caustic crossing actually happened (Alcock et al., 1999).

Later Jaroszyński & Mao (2001) showed that reliable prediction of the exact timing is intrinsically difficult and this is only possible relatively late. Wambsganss (2006) stated in his paper that real-time analysis provides the possibility to analyze the light curve of a microlensing event while the event is ongoing inaddition it allows astronomers to take action quickly.

In this regard the other very interesting and spectacular event in microlensing observation is EROS BLG-$2000-5$, R.A. $=17^h53^m11^s.5$, decl.= $-30^o55'35''$, l = $359^o.14$ b = $-2^o.43$ alerted by EROS on May 5, 2000 (An et al., 2002). Later on June 8, 2000, the Microlensing Planet Searching (MPS) collaboration dispatched an anomaly alert stating that the brightness of the source increased by 0.5 from the previous night and continued its brightness by $0.1\frac{mag}{40minute}$. Then after, the PLANET (Probing Lens Anomalies NETwork) intensified their observation using the four telescopes in the consortium, the Canopus (Tasmania), The Perth/Lowell(West Australia), SAAO, Sutherland, South Africa and the Yale (Chile), until August 2001. An et al. (2002)(and references therein), stated that EROS BLG-$2000-5$ has many unique features including well covered first caustic crossing (entrance), timely prediction of the second caustic crossing (exit) and two time series of spectral observations of the source during the second crossing, the unprecedented four day length of the second crossing. The quality of the data was very good and event duration was long enough to measure parallax and projected binary orbital motion, which in turn are important for modeling the light curve.

University of Cape Town

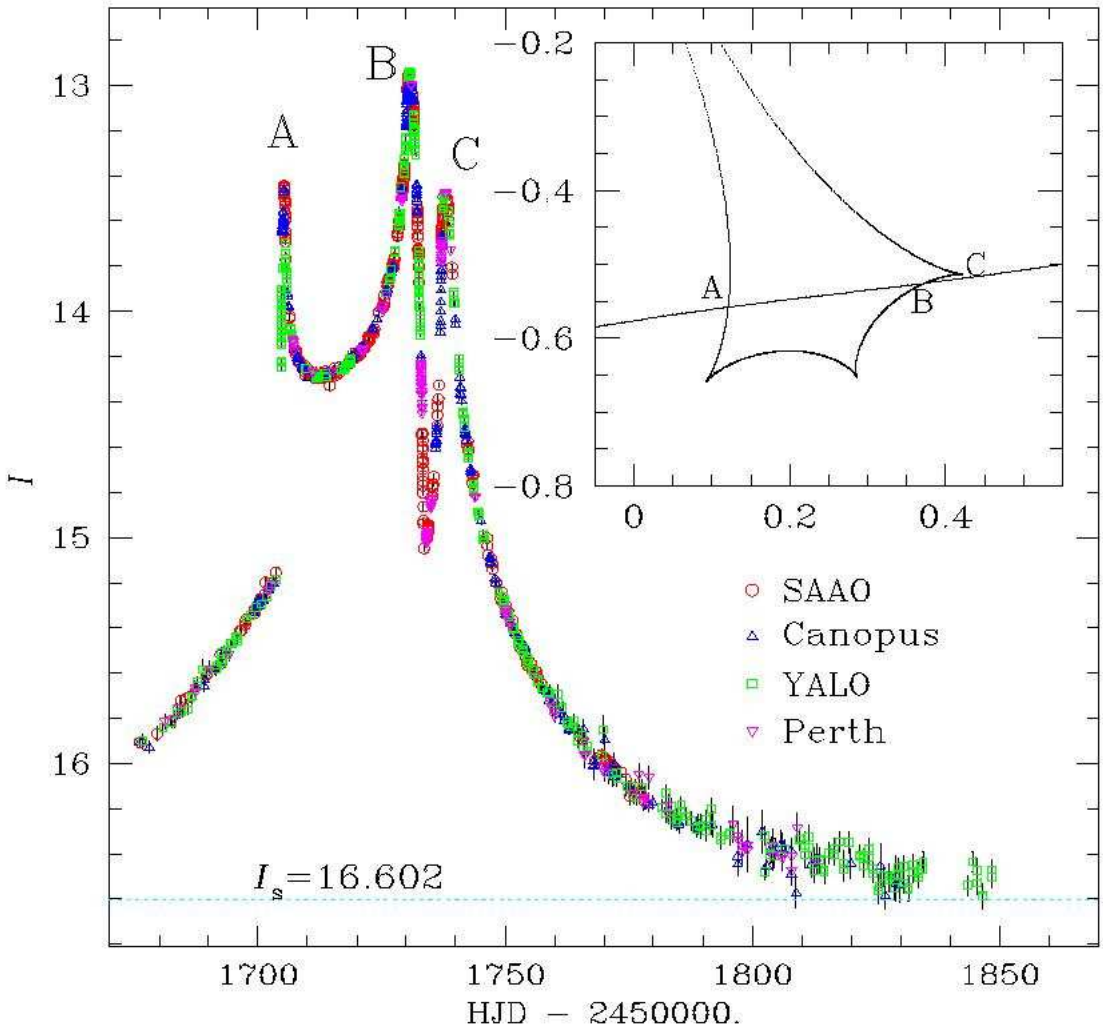

Figure 5.6: EROS-BLG-2000 − 5(2000 season only) PLANET I-band light curve. Data from SAAO shown in red circles, from Yale shown in green squares, blue triangles are from Canopus and the data from Perth are shown in inverted triangles (Adapted from An et al.2002).

The light curve shown in Fig.5.6 is the I-band data from PLANET consortium consisting of 1286 data points with three peaks. Among these two (labelled A and B) are main maxima in the light curve well over 3.5mag from the base line with very steep rising or dropping flanks showing caustic crossing. The other peak (labelled by C) which is shorter than the two shows caustic passages. The figure on the top right panel shows the source star track relative to the binary lens caustics.

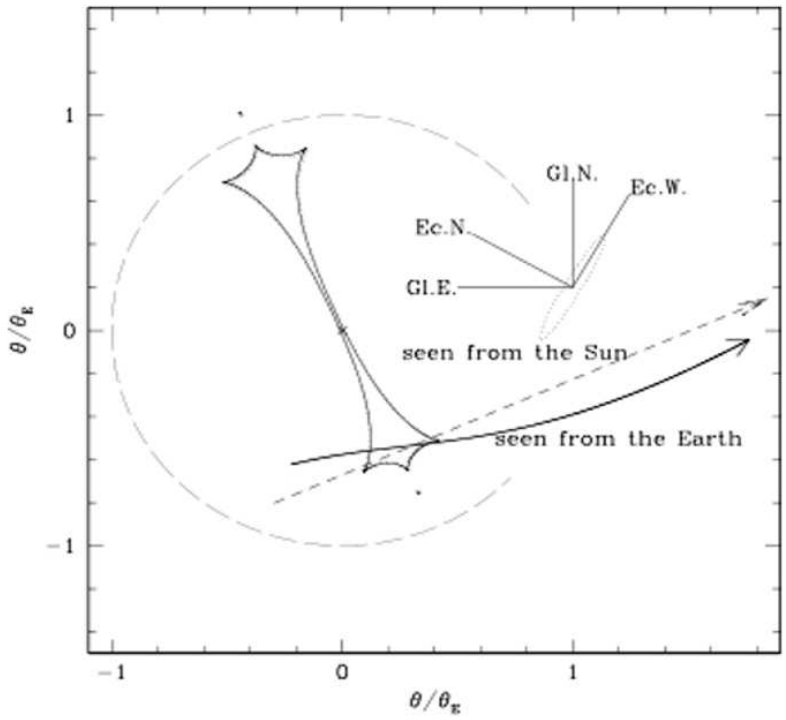

Figure 5.7: The Geometry of EROS-BLG-2000 − 5(2000) season projected on the sky (Adapted from An et al.2002)).

The geometry of the event when projected on the sky is shown in Fig.5.7, showing the differences of the relative paths as seen from Earth- where the left side and the upward side represents Galactic East and Galactic North respectively and the origin is the center of mass of the binary lens system under consideration. The solid curve shows the trajectory of the source relative to the lens as seen from Earth whereas the short dashed line describes the relative proper motion of the source seen from the sun which is the parallax effect (An et al., 2002). The circle drawn using longer dashed lines is the Einstein ring radius with the caustics inside it at two different times (An et al., 2002).

5.3 Advantages and Drawbacks of Microlensing

Though planet searching using microlensing is a challenging astrophysical phenomenon due to its complexity in modeling and analysis, microlensers implemented the technique and contributed a lot in planet detection for the last couple of years, detection of 10 planets (Perryman, 2011).

Gravitational microlensing is purely a gravitational field effect on the light coming from the background source as described by Einstein. In this section the primary objective is to give a brief overview of its advantages and drawbacks in searching for extrasolar planets, as elaborated by Wambsganss (2006).

University of Cape Town

5.3.1 Advantages

Microlensing is free of any bias for nearby stars and planets around the solar type/main sequence stars. This technique of searching for planets is sensitive to any stars along the line of sight to the source star in the Galactic bulge at a distance of 8.5kpc, most sensitive for a lens position half way in between. In a similar way this method is free of any bias regarding large mass planets because the microlensing signal (deviation) on the light curve of an event is independent of the planet's mass whereas the size of the source star has an impact on the light curve in the sense that the finite source diameter will affect the smoothing of the light curve at the peak and hence results in lower amplitude signal leading to a lower detection probability.

Another very important point in microlensing is its ability to detect lower mass planets similar to Earth-size planets from ground based observations and followups

showing its high monitoring frequency as well as photometric accuracy. Microlensing is most sensitive to regions from $0.6 - 1.6\theta_E$, called lensing zones, the region where for low mass main sequence stars considered to be habitable zone and this raises questions regarding the number of planets to be detected in this region. The unique feature of microlensing also includes the possibility of detecting multiple planetary systems. It also helps to detect long period planets with large semi-major axis (Wambsganss, 2006). It also plays a major role in detecting free floating planets and hence gives best statistics of galactic population of planets. So gravitational microlensing is an ideal technique to find planets. But this method is not free of drawbacks.

5.3.2 Drawbacks

Planet detection using microlensing has some limitations: among others, the chance of detecting planet-lensing system by following up and monitoring arbitrary background source star in the Galactic bulge is of the order of 10^{-8} or even smaller this is because of the rare occurrence of microlensing. Additionally, in planetary microlensing system the deviation from ordinary lensing system, on the light curve, and its duration is very short in the order of hours to days. In this method the planets detected are too far with distances in the order of few kpc. And sometimes it is hard to determine the exact distance of the planet unless additional information is gathered about the target in consideration and this even makes further study of the planet impossible. There is also a possibility of parameter degeneracy during modeling, with no relation between light curves and planet parameters.

Planet detection in this method as described earlier is possible but the difficulty arises in determining its mass. Instead this method allows to determine the mass ratio between the planet and its host star. The other main drawback in this method is that microlensing is a one and only one time event and further confirmation is unlikely to happen. The afore-mentioned premises are not points against implementing microlensing searching technique. Nowadays, due to the availability of software, intensive monitoring for almost 24 hours a day and collaboration work among groups working on microlensing technique reduces the drawbacks in many aspects.

University of Cape Town

6

Review of Planets Discovered through Gravitational Microlensing

University of Cape Town

6.1 Introduction

Gravitational microlensing as a technique for searching extrasolar planets is playing a major role in detecting extrasolar planets, planets beyond our solar system. Since its conception up to date thousands of microlensing targets were observed and analyzed by astronomers all over the world. In this chapter, we are going to revise some of the planets discovered using microlensing technique.

6.2 Planets Discovered through Microlensing

(a) OGLE-2003-BLG-235/MOA-BLG-53

Alerted and reported by OGLE Early Warning System (Udalski, 2003), OGLE-2003-BLG-235/MOA-BLG-53, OGLE-2003-BLG-235 (α = $18^h05^m16^s.35$, δ = -28^{o}53$'$42$"$.0, J2000) during the 2003 observing season on 22 June but this target was independently detected by MOA on 2003 July21 and was labelled as MOA-2003-BLG-53.

The OGLE observation group, according to Bond et al. (2004), observed the target in the I band with an exposure time of 120s on the other hand the MOA observation group observed the target with a broad band red filter with an exposure time of 180s. The photometry for the two observing teams were derived using difference image analysis (Wozniak, 2000).

Bond et al. (2004) stated that the microlensing event was the first microlensing target leading to the discovery of planet and they developed a model light curve shown below.

OGLE-2003-BLG-235 (MOA-BLG-53) was observed since 2000 and this long duration was a behavior for single point lens microlensing events (Bond et al., 2004), but this event had a unique feature which is a short duration deviation from known single lens microlensing events. The spike resulted was due to the source crossing the closed caustics, where the first spike is due to the source coming in to the caustic and the second spike on the other hand is due to the source exiting from the caustic. From the light curve shown below in Fig.6.1, the caustic entry and exit was well covered by MOA on July 21, 2003. Bond et al. (2004) studied the time taking for the source to cross the caustics and found to be short 12% of the total time needed to cross the Einstein ring radius and they used this information with the small amplitude (25 percent) of the photometric deviation to determine the mass ratio which resulted in the event to be a binary lens system with small mass ratio (q = 0.0039).

Bond et al. (2004) used minimization schemes to search χ^2 local minima by allowing all the parameters used to describe the binary lens, t_E the Einstein crossing time, u_0 the impact parameter, t_0 time for closest approach to the center of mass, q the mass ratio, transverse separation of lens components, ϕ the position angle and if the system is a caustic crossing event additional parameters ρ apparent angular radius of the source star with respect to the

University of Cape Town

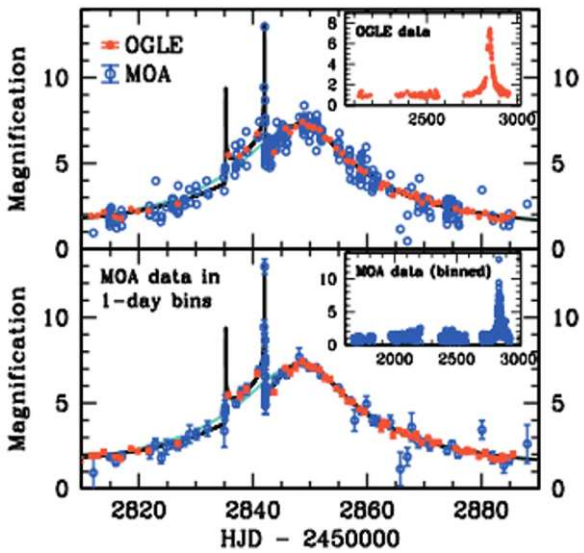

Figure 6.1: OGLE-2003-BLG-235/MOA-BLG-53 best fit model where the OGLE and MOA data points are shown as red filled circles and blue circles, respectively (Adapted from Bond et al.2009).

Einstein ring was included furthermore two linear scaling parameters between the magnification and the flux units for each passband, to vary all at a time. This minimization scheme resulted in local minima of $\chi^2 = 1390.4$ for 1267 degree of freedom with small mass ratio of $q = 0.0039$. This mass ratio is a strong evidence of its secondary to be a planetary companion (Bond et al., 2004). Further analysis of OGLE-2003-BLG-235/MOA-BLG-53 resulted in $D_{len} = 5.2^{+0.2}_{-1.29}$kpc with 90% confidence level and Bond et al. (2004) used $\frac{M_{lens}}{M_\odot} = 0.123(\frac{\theta_E}{mas})^2 \frac{D_{source}}{kpc} \frac{x}{1-x}$, where $x = \frac{D_{lens}}{D_{source}}$, which gives relationship between the lens mass and distance. The authors described the lensing system to be an M_2-M_7 dwarf star with $0.36^{+0.03}_{-0.28} M_\odot$ and its companion is a planet with a mass of $1.5^{+0.1}_{-1.2} M_J$ where M_J is Jupiter mass. The planetary companion was found to exist at a distance of $3.2^{+0.1}_{-1.7}$AU, which was concluded to be in a wide orbit.

University of Cape Town

(b) OGLE-2005-BLG-071

This microlensing target was alerted by Early Warning System on 2005 March17 using the OGLE-III observation and was predicted to have a peak about a month time. But using the OGLE observation data points 3 days before the closest approach and μFUN points the target was peaking a high magnification which in turn triggered intensive observation and follow up of the target. Udalski et al. (2005) described that a single lens fit to this observation resulted worse χ^2 which leads to a second alert by μFUN stating about the start of the anomaly. Different observatories covered the event. Udalski et al. (2005) used the data from OGLE (1.3m telescope at Las Campanas Observatory in Chile), MOA (0.6m at Mount John Observatory in New Zealand), μFUN Chile (SMART 1.3m telescope at CTIO), Palomar (60inch (1.5m) robotic telescope), MDM (Hiltner 2.4m at Kitt Peak), Auckland (0.3m Nustrini telescope at Auckland Observatory), Farm Cove (0.25m Meade at Farm Cove Observatory), Faulkes North (2.0m in Hawaii), and Canopus (1.0m at Hobart, Tasmania). Udalski et al. (2005) demonstrated that the event was a planetary microlensing with a mass ratio, $q = 0.0071$ obtained from the best fit and constrained the mass of the host star to be in the range $0.08M_{\odot} < M < 0.5M_{\odot}$ with the planet's distance found to be in the range $1.5 < D_L <$ 5kpc and the mass of the planet is in the range $0.05 < \frac{m_p}{M_{Jup}} < 4$ where m_p and M_{Jup} are mass of the planet and mass of Jupiter respectively and the planet was concluded to be a Jovian-mass planet.

From the light curve shown in Fig. 6.2 as Udalski et al. (2005) stated the two peaks were generated as a result of the source when it is passing very close to the two cusps of the central caustics. By observing the two peaks it is possible to see that the size of the peaks have equal height which is resulted due to the fact that the source passed almost perpendicular to the binary axis, $\alpha \sim \pm 90^o$. The other justification presented regarding the weakness of the middle peak was due to the asymmetric property of the caustics. OGLE-2005-BLG-71 was the second planet detected and was also the first high magnification planetary event. Udalski et al. (2005) also stated the effectiveness of searching Earth mass planets from central caustic events.

University of Cape Town

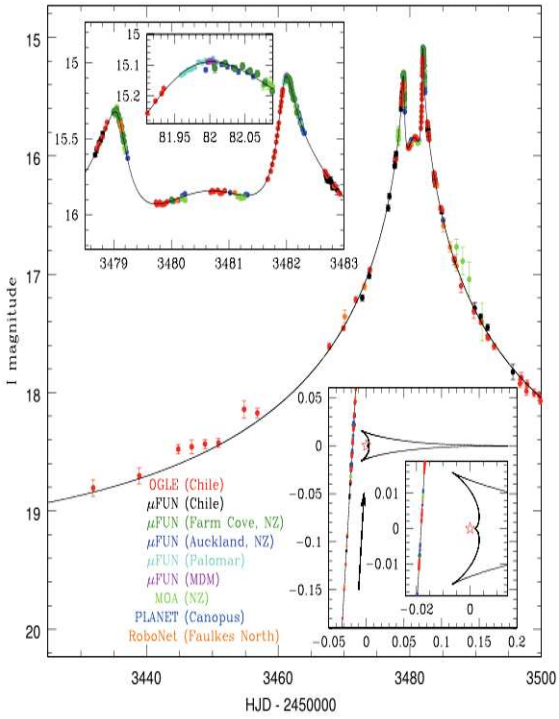

Figure 6.2: OGLE-2005-BLG-71 best fit light curve showing a planetary companion : (Adapted from Udalski et al.2005)

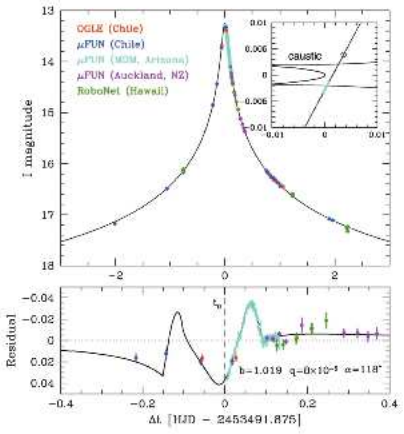

Figure 6.3: OGLE-2005-BLG-169 best fit light curve shown on the top panel: Lower panel shows the difference between the model and the single lens microlensing event model with the same parameters : (Adapted from Gould et al.2006)

(c) OGLE-2005-BLG-169 (Neptune like Planet)

OGLE-2005-BLG-169 was a target alerted by OGLE collaboration on 2005 April 21 as a microlensing event from the Warsaw telescope in Chile. Then as Gould et al. (2006) stated this target was a high magnification event. The collected data were reduced using OGLE data pipeline using DIA (Difference Image Analysis) developed by Wozniak (2000) where as the μFUN MDM data were reduced using ISIS pipeline. Gould et al. (2006) on their best fit model shown in Fig.6.3 demonstrated that OGLE-2005-BLG-169 was a caustic crossing event where the caustic exit was properly resolved which in turn resulted in a one dimensional degeneracy of model parameters.

To analyze the data collected from observation of the target to get the model parameters, Gould et al. (2006) implemented parameter grid search by fixing three parameters: b (separation of the component in units of θ_E), α (angle of the source trajectory relative to the binary axis) and q (the mass ratio) while minimizing χ^2 over the remaining parameters and obtained a binary system with mass ratio $q = 8^{+2}_{-3} \times 10^{-5}$ and $b = 1.00 \pm 0.002$. Further analysis including parallax effect, Finite source effect helped to determine the mass of the host star and the planet. Gould et al. (2006) assumed the parent star is a main sequence star having mass M$\sim 0.49^{0.29}_{-0.29} M_{\odot}$ leading the planet to have a mass

of $\sim 13M_{\oplus}$ with projected separation of 2.7AU.

(d) OGLE-2005-BLG-390(Cool Planet of $5.5M_{\oplus}$)

During the 2005 microlensing observation season, OGLE Early warning system announced a target OGLE-2005-BLG-390 ($\alpha = 17:54:19.2, \delta = -30:22:38, J2000$) and was monitored and observed by PLANET, OGLE and MOA observing groups. As Beaulieu et al. (2006) described follow up of the target resulted in a maximum magnification of $A_{max} = 3$ on the 31^{st} of July and continuous monitoring of this event resulted a deviation from single lens light curve on 9 August 2005 spotted by PLANET and the deviation finally was confirmed and resulted due to a low mass planet orbiting the lens star. The best fit light curve shown in Fig.6.4 clearly shows the deviation from single lens microlensing event. The top right panel in the figure shows the magnified view of the planetary deviation.

The analysis of the observed data revealed the presence of the first low mass planet with a mass ratio $q = 7.6 \times 10^{-5}$ and projected planet star separation $d = 1.610 \pm 0.008\theta_E$. In addition Beaulieu et al. (2006) calculated the angular radius using the surface brightness relation with its color and found to be $5.25 \pm 0.008\theta_E$ corresponding to a source radius of $9.6 \pm 1.3R_{\odot}$ where the source star is assumed to be at a distance 8.5kpc. After the discovery, the planet was named as OGLE-2005-BLG-390Lb where the suffix "Lb" refers to the secondary component of the lens with planetary mass ratio (Beaulieu et al., 2006).

Beaulieu et al. (2006) in their paper reported the implementation of Bayesian analysis using the Galactic model and mass function. The distances and velocities of the lens and source star was averaged subjected to the constraints due to the angular diameter of the source and the parameters obtained after analysis resulted in high probability (95%) for the planet host star to be main sequence star, 4% probability being a white dwarf and $< 1\%$ being a neutron star or a black hole. Then, further analysis using the medians of the lens star parameter probability distribution resulted in a companion mass of $5.5^{+5.5}_{-2.7}M_{\oplus}$ and an orbital separation of $2.6^{+1.5}_{-0.6}$AU from the lens star with mass $0.22^{+0.21}_{-0.11}M_{\odot}$ situated at $D_L = 6.6 \pm 1.0$kpc. Another impressive result obtained from the analysis done by Beaulieu et al. (2006) was the amount of radiation received from the host star and was found to be 0.1% and its surface temperature was assumed to be $\sim$ 50k, which is similar to the surface temperature of Neptune and Pluto (Beaulieu et al., 2006).

University of Cape Town

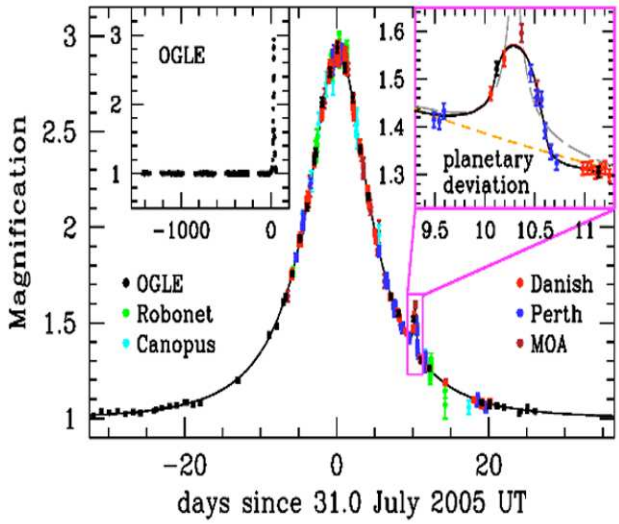

Figure 6.4: OGLE-2005-BLG-390Lb best fit model plotted as a function of time Top right panel: The magnified view of planetary deviation.(Adapted from Beaulieu et al.2006)

(e) OGLE-2006-BLG-109 (Jupiter/Saturn analog)

The OGLE Warning System announced OGLE-2006-BLG-109 as a non standard microlensing event with a sign of planet (Gaudi et al., 2008) and intensive follow up and observations was done by μFUN and RoboNet. During follow up, the event showed deviation from a single lens event on 5 April which gives a clue of a binary lens. Between 5 to 8 of April this event resulted in additional peaks within 12hrs of the firs deviation where a preliminary model indicated that the first deviation was due to the presence of a Jovian class planet. The model also predicted a peak to happen on the 8^{th} of April but there were additional peaks on 5 to 6 of April which in turn Gaudi et al. (2008) concluded that this deviation happened due to a second Jovian class planet as it is shown in the best fit microlensing light curve in Fig. 6.5.

Further analysis of the event OGLE-2006-BLG-109, Gaudi et al. (2008) confirmed a multiple planetary systems with masses $m_1 = 0.71 \pm 0.08 M_J$ and $m_2 = 0.27 \pm 0.03 M_J$ and orbital separation of ~ 2.3AU and 4.6AU orbiting a primary star with mass $\sim 0.5 M_\odot$ at a distance ~ 1.5 pc. They also detected the orbital motion of the outer planet. The orbital motion changes the shape of the caustic curve as it is shown on the top left panel of the figure. Gaudi et al. (2008) suggested that if the target under consideration is a planetary system, it may have the same property with our solar system and in general OGLE-2006-BLG-109 could demonstrate a planetary system and could be able to constrain solar system analogous through out the Galaxy.

University of Cape Town

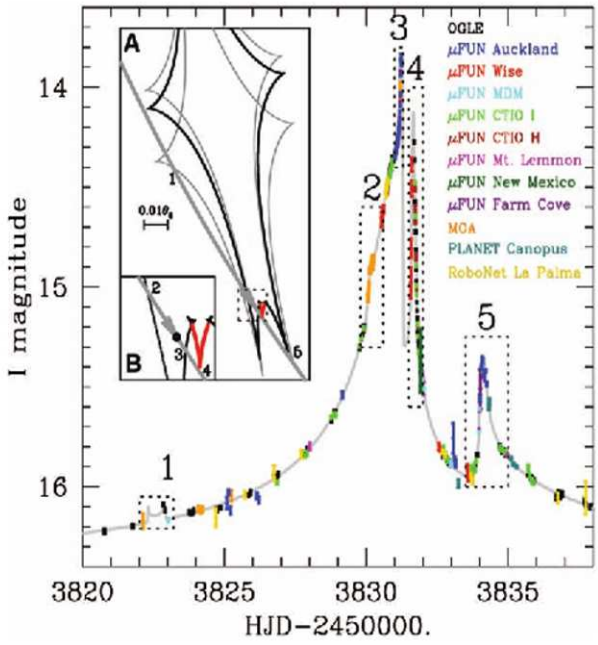

Figure 6.5: OGLE-2006-BLG-109Lb best fit model for two planet system and the panel on left corner shows the caustic structure created by the two planet system with the source trajectory: (Adapted from Gaudi et al.2008)

(f) MOA-2007-BLG-400

Among the microlensing targets observed during the 2007 observing season MOA-2007-BLG-400 was the one with $[(\alpha, \delta)_{J2000} = 18^h09^m41^s.98, \text{-}29^o13'26".95)]$, which was alerted by MOA collaboration on 5^{th} of September 2007. This target was alerted very late due to bad weather and the event time scale was short $t_E \sim 15$ days.

On the 7^{th} of September Microlensing FollowUP Network (μFUN) began observing this target as a high magnification event but intensive follow up and observation was not done till September 10, which is 15hrs before the peak magnification then intensive observation was done from seven different observatories, μFUN Bronberg (South Africa), μFUN SMARTS (CTIO, Chile), μFUN CBA Perth (Australia), μFUN Farm Cove (New Zealand), μFUN Auckland (New Zealand) and μFUN Southern stars (Tahiti), μFUN Campo Catino Austral (CAO, Chile). With a 5 minute exposure time, the peak and the planetary anomalies observed during the μFUNSMARTS (Chile) observations at CTIO, $4354.47 < HJD' < 4354.69$ using the ADICAM optical IR dual channel camera and μFUN CAO (Chile) observations $4354.5 < HJD' < 4354.7$ observed in I band with quite few data points (8) in V to measure the (V-I) color (Dong et al., 2009).

The data collected from μFUN, CTIO and MOA used for analysis due to the fact that they provide all informations required to constrain microlensing models. The MOA data and the μFUN CTIO data were reduced using the MOA Difference Image Analysis (DIA) and DIA developed by Woźniak respectively. The model shows the microlensing event MOA-2007-BLG-400 was affected by finite source effect and it resembles a single lens light curve with finite source effect included as it is shown on the top panel of the figure (Dong et al., 2009).

Detailed investigation of the lower panel has a hump on the rising side of the light curve and a negative spike on the falling side which lasts for 30 minutes (Dong et al., 2009). The time for these deviations enhances that the two humps (positive and negative) are due to the microlensing effect than stellar variability. They suggested additional explanations for the two humps that is either the source is transited by caustics resulted due to a binary or planetary companion or the limb of the source is not modeled properly. But if circular source is assumed the second explanation would lead symmetric residual where as the plot in the lower panel show other way.

Since MOA-2007-BLG-400 was a highly magnification event, Dong et al. (2009)

University of Cape Town

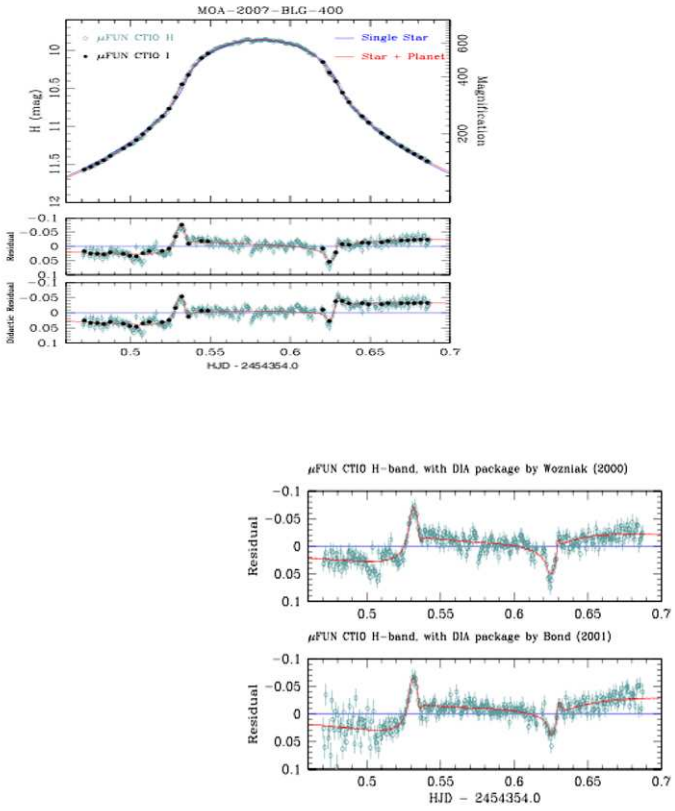

Figure 6.6: Top panel: MOA-2007-BLG-400 best fit light curve middle panel: Residuals from best fit point lens model and its deviation from planetary model Lower panel: Residuals from a point lens model with the same parameter: (Adapted from Dong et al.2009)

used "magnification map" technique for searching companions over a wide range of masses. The main principle is for a given (d, q) pair, rays were shot over a very narrow annulus in the image plane around the Einstein ring and sort the rays in pixel on the source plane. Then, if there are pixels that intersect the source, it is possible to determine weather the rays landed on the source or not then one can evaluate the source surface brightness at that position.

The results obtained after the analysis were the mass ratio which is found to be $2.5^{+0.5}_{-0.3} \times 10^{-3}$ with d=2.9 ± 0.2 and the companion was supposed to be Cool Jovian mass planet. Dong et al. (2009) demonstrated the $d \leftrightarrow d^{-1}$ degeneracy and obtained a mass ratio $q = 2.6 \pm 0.4 \times 10^{-3}$ with d=2.9^{-1}=$0.34^{+0.03}_{-0.02}$. In their model Dong et al. (2009) also demonstrated the finite source effect with source radius relative to Einstein ring radius given by $\rho = \frac{\theta_*}{\theta_E} = (3.29 \pm 0.08 \times 10^{-3})$ and MOA-2007-BLG-400 was also affected by limb darkening and blending.

University of Cape Town

(g) MOA-2007-BLG-192

Bennett et al. (2008) presented the analysis of MOA-2007-BLG-192, which was the first planetary microlensing event to be discovered without follow up observations of the light curve. Observation was done using the 2.2deg^2 field of MOA-Cam3, mounted on the 1.8m MOA-II telescope which helps to cover a wide range 50deg^2 of the Galactic bulge every hour and the frequent sampling resulted in the detection of MOA-2007-BLG-192 was one of the high magnification events where planet detection is possible from perturbation of the central or "central" caustics.

Analysis of this event was done by Bennett et al. (2008) and during modeling they included parallax and xarallap (A microlensing effect caused by the orbital motion of the source star where the source star have a binary orbit). So, Bennett et al. (2008) obtained the best fit microlensing model with finite source effect and parallax effects shown in Fig.6.8 and used these values to determine the lens mass $M = 0.06^{0.028}_{-0.021} M_{\odot}$, where $m = 3.3^{+4.9}_{-1.6} M_{\oplus}$ which was likely a brown dwarf planet orbiting the lens mass. Then further analysis of MOA-2007-BLG-192Lb could also have a habitable surface temperature taking in to account that the host star provides small radiative energy(Bennett et al., 2008).

(h) OGLE-2007-BLG-368Lb(A Cold Neptune-Mass Planet)

Sumi et al. (2010) discussed OGLE-2007-BLG-368Lb (R.A., decl.)(2000)= $(17:56:25.96, -32:14:14.7)[(l,b) = (358^o.3, -3^o.7)]$ was alerted by the OGLE Early Warning System (EWS) on 2007July10 and was independently detected by MOA and alerted as MOA-2007-BLG-308 on 2007 July 12. After a series follow ups and observations a total of twelve light curves from seven participating telescopes were collected. This event as Sumi et al. (2010) stated the photometry was difficult as compared to most microlensing events due to the presence of brighter star close to the source star. Due to this fact PSF (Point Spread Function) fitting photometry approach was inconvenient so they implemented DIA (Difference Image Analysis).

Sumi et al. (2010) modeled this event using the parameters from single lens, Binary lens parameters including parallax and xarallap and obtained the parameters necessary to describe the event. Among these the mass ratio was found to be $q = (9.5 \pm 2.1) \times 10^{-5}$ and the deviation due to this planet was detected in real time. They also implemented Bayesian analysis and obtained the mass of the planet to be $M_p = 20^{+7}_{-8} M\oplus$ with a projected separation of

University of Cape Town

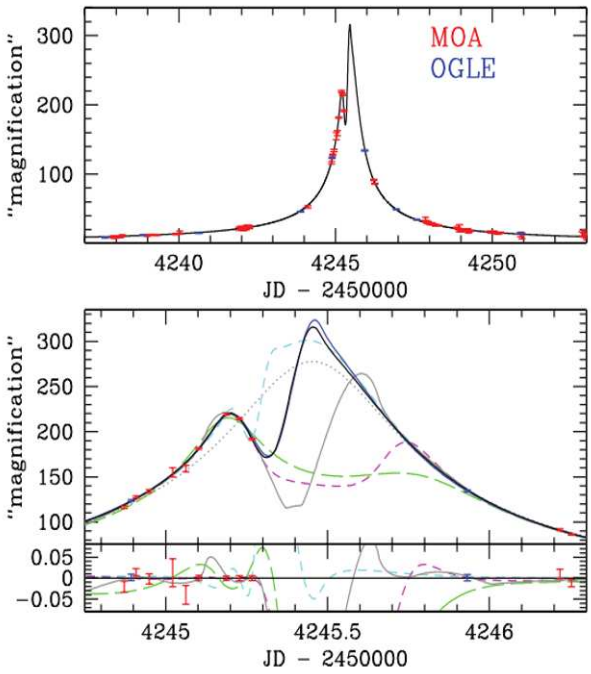

Figure 6.7: Light curve showing part of MOA-2007-BLG-192 as it is observed by MOA telescope, The middle panel shows the magnified part of the light curve peak and the lower sub panel shows the deviation of the data from the best fit model: (Adapted from Bennett et al.2008)

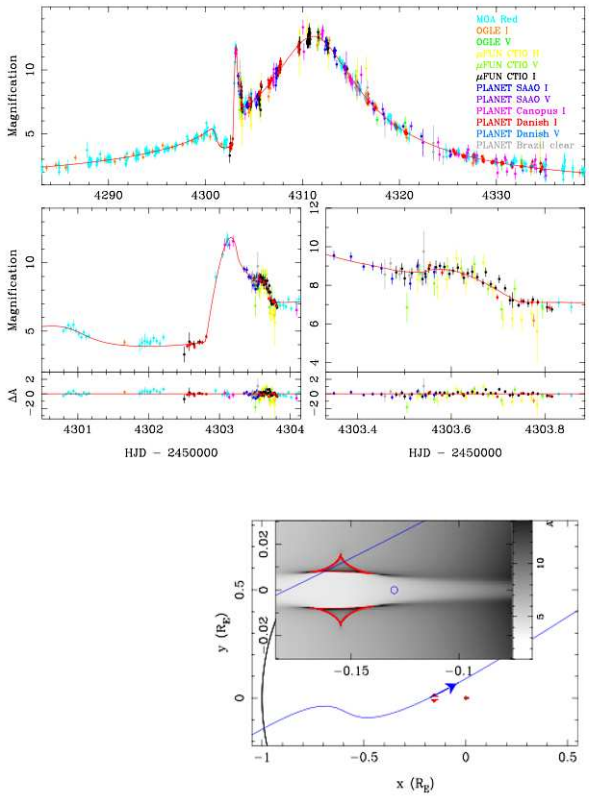

Figure 6.8: Top panel: Light curve showing OGLE-2007-BLG-368 for the whole event: Lower left panel: Magnified part of the planetary deviation. Lower right panel: Plot showing the second caustic crossing, Bottom panel: Plot showing caustics (red lines) and critical curves (black lines) the blue line shows the source trajectory. (Adapted from Sumi et al.2010)

$2.8^{+0.5}_{-0.6}$AU around a K-dwarf with mass $M_L = 0.64^{+0.21}_{-0.26}M_\odot$ and stated that OGLE-2007-BLG-368Lb was found to be the fourth Neptune-mass planet detected by microlensing (Sumi et al., 2010).

(i) MOA-2008-BLG-310Lb (Sub Saturn Planet)

Detected by Microlensing Observation in Astrophysics (MOA) on 2008 July 9 (HJD' $\equiv$ HJD $-$ 2450000 = 4654.458) as MOA-2008-BLG-310 [(R.A., decl.) = $(17:54:14.53, -34:46:40.99), (l, b) = (355.92, -4.56)$] and was one of the microlensing targets during the 2008 observation campaign. MOA then issued a high magnification alert then the microlensing Follow Up Network (μFUN) began intensive monitoring of this target (Janczak et al., 2010). Observation of this target was taken from six different observatories MOA(New Zealand) 1.8m I, μFUN Auckland (New Zealand) 0.41m R, μFUN Bronberg (South Africa) 0.36m unfiltered, μFUN SMARTS CTIO (Chile) 1.3m I, V, H, MiNDSTEP La Silla (Chile) 1.54m I, and PLANET Canopus (Tasmania) 1.0m I. Among these observatories μFUN Bronberg covered the peak and the anomaly.

The light curve shown below in Fig. 6.9 as discussed in Janczak et al. (2010) for MOA-2008-BLG-310 was primarily modeled as a single lens microlensing event and the data collected fit with this model with a prominent finite source effect. Despite the effect of the finite source effect, which made the peak of the light curve wide and smooth, no deviation from single lens model was observed but the maximum magnification, $A_{max} \sim 400$, achieved made the event to be a good candidate for planet detection. Janczak et al. (2010) studied the deviations observed in the residual from the single lens fit (middle panel) and discovered that the lens model under consideration was more complicated than a point lens where the short time scale deviation near the peak of a high magnification event (middle panel) was a clue for existence of planetary or binary companion.

Detailed analysis by Janczak et al. (2010) resulted in a planet/star mass ratio $q = (3.3 \pm 0.3) \times 10^{-4}$ with angular separation $\theta_E = 0.155 \pm 0.011$mas. The analysis of this microlensing event was done including Limb darkening and blending (which can be caused from the lens or companion to the lens, from the source or any unrelated stars) but they used the blending due to the lens to estimate the mass of the lens and obtained $M_L = 0.67 \pm 0.14 M_\odot$ and the planet's mass $m_p = 74 \pm 17 M_\oplus$ with projected separation of 1.25 ± 0.10AU.

University of Cape Town

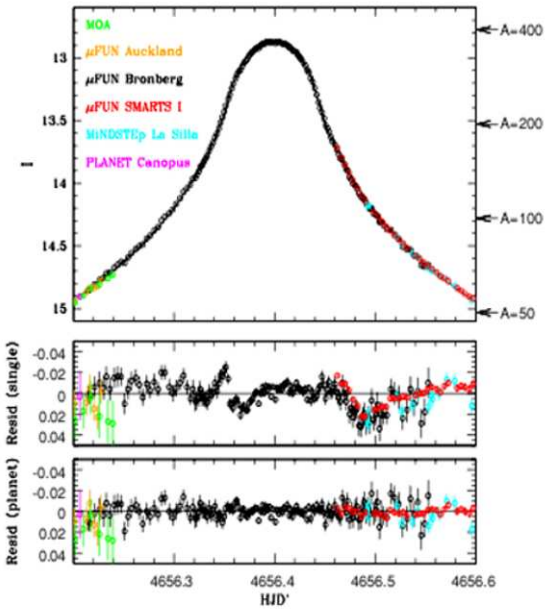

Figure 6.9: Top panel: Light curve showing MOA-2008-BLG-310 plotted using the data from all the participating telescopes where the plot was the best fit single lens model. Middle panel: Residuals to the best fit model of single lens microlensing model. Lower panel: Plot showing the residuals to the best fit planetary model. (Adapted from Janczak et al.2010)

(j) MOA-2009-BLG-319Lb

Alerted by MOA collaboration on 2009 June 20 as an ordinary microlensing event, MOA-2009-BLG-319 [(R.A., decl.)$_{J2000}$=($18^h06^m58^s.13$, $-26^o49'10".89$), (l, b)=$(4.202, -3.014)$] but was found to be a high magnification effect. The final and complete observation data was collected from 20 different observatories including MiNDSTEP, Infrared Survey Facility telescope in South Africa. Miyake et al. (2011) presented the analysis of the event and showed that the event exhibits a number of caustic crossings as it is clearly shown on the light curve. This microlensing event was also affected by finite source effect. The authors also measured the source color and used it to determine the limb darkening parameters.

In order to derive the parameters necessary to explain the event, MOA-2009-BLG-319, Miyake et al. (2011) used Markov Chain Monte Carlo (MCMC) algorithm to find the χ^2 minimum. Since the number of parameters to completely describe this event are large, where three parameters taken from single lens events: t_0 , t_E, u_0, from binary lens model: q, d, θ_E), α (the angle of the source trajectory relative to the binary lens axis), $\rho = \frac{\theta_*}{\theta_E}$ (source radius relative to the Einstein radius) in addition two parameters to describe the unmagnified source and background fluxes for each band and data set. Wide parameter search was implemented and obtained best fit model of mass ratio $q = 3.95 \pm 0.02$ with $d = 0.97537 \pm 0.00007$. Miyake et al. (2011) studied the parallax effect in MOA-2009-BLG-319 and studied the properties of the lens and the source which is found to be a bulge G-dwarf source star with $D_s \approx 8$kpc. The analysis also revealed the source star to be a K- or M-dwarf star with mass of $M_L = 0.38^{+0.34}_{-0.18} M_\odot$ and distance $D_L = 6.1^{+1.1}_{1.2}$kpc, planetary mass $m_p = 50^{+44}_{-24} M_\oplus$ and projected separation $2.0^{+0.4}_{-0.4}$AU.

The following table shows the summary of the planets discovered using gravitational microlensing from 2004 to 2011.

University of Cape Town

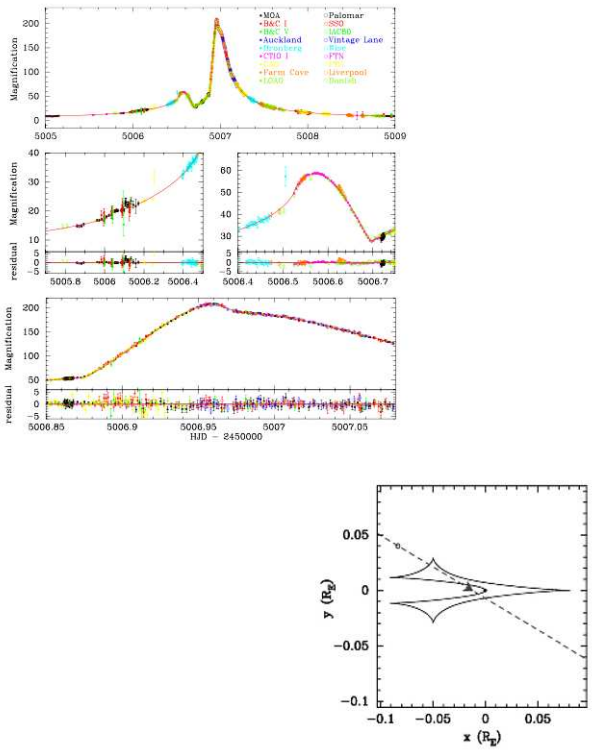

Figure 6.10: Top panel: The Best fit model and data points of the light curve showing a planetary microlensing event MOA-2009-BLG-319 with finite source and limb darkening effects. Middle and Lower panels show the magnified view of the caustic crossing and the residuals from the best fit model. Bottom panel: Plot showing the caustic curve (Solid line) and the source track (dashed line) where the source star crosses the caustic curve four times. (Adapted from Miyake et al.2011)

Table 6.1: Table summarizing the number of planets discovered using gravitational microlensing, their parameters (host star mass, lens distance, projected star-planet distance, planet mass)Adapted from (Perryman M., 2011)

.

ML Events	q	D_L(kpc)	$M_*(M_\odot)$	M_P	a(AU)
OGLE-2003-BLG-235Lb	3.9×10^{-3}	5.8 ± 0.6	$0.63^{+0.07}_{-0.09}$	$2.6^{+0.8}_{-0.6} M_J$	$4.3^{+2.5}_{-0.8}$
OGLE-2005-BLG-71Lb	7.1×10^{-3}	3.2 ± 0.4	$0.46^{+0.04}_{-0.04}$	$3.8^{+0.4}_{-0.4} M_J$	$3.6^{+0.2}_{-0.2}$
OGLE-2005-BLG-390Lb	7.6×10^{-5}	6.6 ± 1.0	$0.22^{+0.21}_{-0.11}$	$5.5^{+5.5}_{-2.7} M_\oplus$	$2.6^{+1.5}_{-0.6}$
OGLE-2005-BLG-169Lb	8.0×10^{-5}	2.7 ± 1.4	$0.49^{+0.23}_{-0.29}$	$13^{+4.0}_{-5.0} M_\oplus$	$2.7^{+1.5}_{-1.0}$
OGLE-2006-BLG-109Lb	1.3×10^{-3}	1.5 ± 0.1	$0.50^{+0.05}_{-0.05}$	$0.71^{+0.08}_{-0.08} M_J$	$2.3^{+0.2}_{-0.2}$
MOA-2007-BLG-192Lb	2.0×10^{-4}	1.0 ± 0.4	$0.06^{+0.02}_{-0.02}$	$3.3^{+4.9}_{-1.6} M_\oplus$	$1.0^{+0.4}_{-0.4}$
MOA-2007-BLG-400Lb	2.5×10^{-3}	5.8 ± 0.7	$0.30^{+0.19}_{-0.12}$	$0.83^{+0.49}_{-0.31} M_J$	$0.72 or 6.5$
OGLE-2007-BLG-368Lb	9.5×10^{-5}	5.9 ± 1.2	$0.64^{+0.21}_{-0.26}$	$20^{+7.0}_{-8.0} M_\oplus$	$3.3^{+1.4}_{-0.8}$
MOA-2008-BLG-310Lb	3.3×10^{-4}	$\gtrsim 6.0$	$0.67^{+0.14}_{-0.14}$	$74^{+17.0}_{-17.0} M_\oplus$	$1.25^{+0.1}_{-0.1}$
MOA-2009-BLG-319Lb	3.9×10^{-4}	6.1 ± 1.1	$0.38^{+0.34}_{-0.18}$	$0.16^{+0.14}_{-0.08} M_J$	2.0 ± 0.4

University of Cape Town

7 Observations and Analysis

University of Cape Town

7.1 Introduction

In this chapter the theoretical models of binary microlensing events will be tested with observational data obtained from different observatories in the southern hemisphere. The first section in this chapter is dedicated to give an overview of the observation of the microlensing target and the data reduction processes as well as introducing the telescopes we used for followup observations. The next section incorporates all data analyses and discussions with the best fit models along with parameters followed by future prospect of the project is going to be presented.

7.2 Observation and Data Reduction

Alerted by OGLE-IV EWS Udalski (2003) the microlensing target OGLE-2011-BLG-265 is found in the Galactic field BLG504.29 with R.A (J2000)$17:57:47.72$ and Dec(J2000) $-27:23:40.3$ (http:ogle.astrouw.edu.pl/ogle4/ews/blg-265.html).

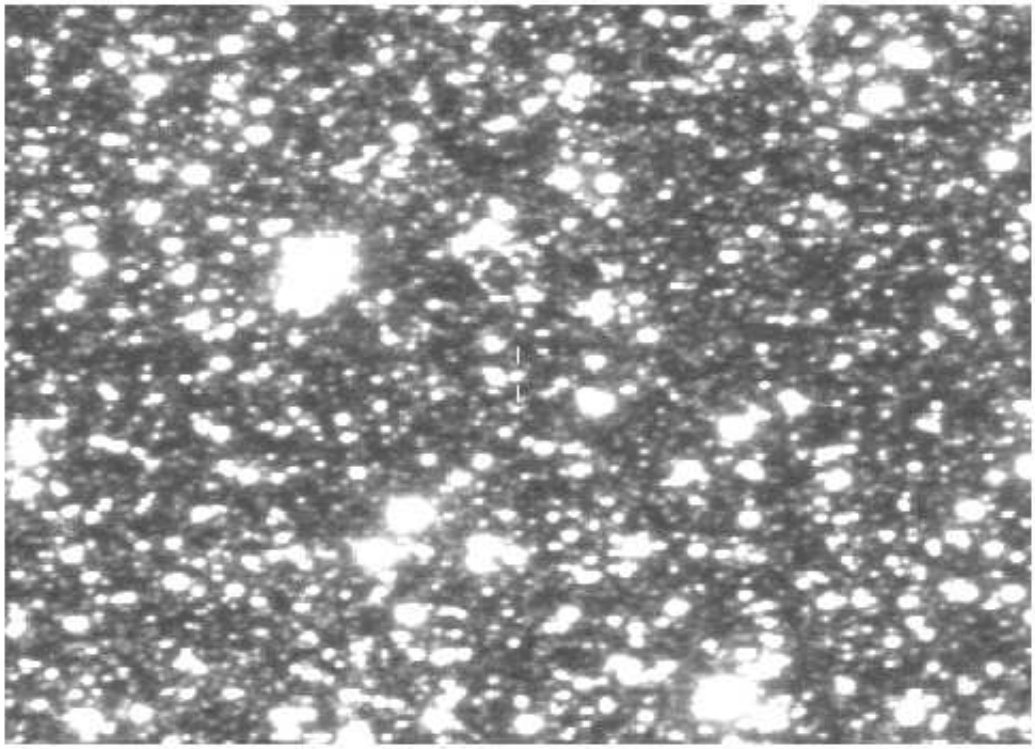

Figure 7.1: Microlensing target OGLE-2011-BLG-265 located right at the center. The image size is $2' \times 2'$. North is up and East is to the Left: Courtesy of http://ogle.astrouw.edu.pl/ogle4/ews/2011/blg-0265.html

University

OGLE-2011-BLG-265 was among the the 1500 microlensing candidates during the OGLE-IV observing season discovered by EWS. The target is located at the center point as it is shown in the fig. 7.1. The OGLE photometric data pipeline is basically based on Difference Image analysis (DIA) photometry (Alard et al.1998, Alard, 2000), (Wozniak, 2000). DIA photometry basically ensures better quality photometer in dense stellar fields so in order to monitor the target in this case I band is chosen as a primary monitoring band with an exposure time of around 200s. The I band filter was preferred because with the short exposure times and in all phases of the moon it helps to obtain stable, precise photometry in dense stellar fields.

Observation of the target was done from PLANET observation consortium: the

1m telescope at the South African Astronomical Observatory, Sutherland, South Africa, the 1.0 m Canopus telescope, Tasmania, Australia, The Perth 0.6m, Perth Observatory, Bickley, Western Australia, Australia and the OGLE 1.3m, Warsaw University Telescope in Las Campanas Observatory, Chile as well as the Danish 1.54 m telescope at La Silla, Chile. These telescopes are located at a widely separated longitudes in the Southern Hemisphere and observation and monitoring was done in coordinated monitoring campaigns. Due to this fact PLANET observation group is capable of providing a 24hr. monitoring of several microlensing events (Albrow et al., 1998). The target under consideration, OGLE-2011-BLG-265, was observed with I filter in all telescopes. Precise photometry was performed in each and every telescope of the PLANET observation group using different packages of photometry. La Silla and Perth used the DAOPHOT package (Stetson, 1987) to photometer the frames where as SAAO used DoPHOT (Schechter, 1993). As mentioned earlier for different observatories independent photometric system were assumed which in turn helps in the inclusion of the determination of independent (unlensed) source and background fluxes for each telescope and filter band in the microlensing data analysis. Data reduction was done in all sites but communication among sites were done to keep the observing campaign strategy on track. To maintain intergroup communication during observation in all weather conditions, sample star was chosen in the field as a secondary standard. The main importance of this star was to express the flux of the microlensed source in terms of the average flux of the sample star later to be calibrated against photometric standards (Albrow et al., 1998). The behavior of the sample star was also used as a guide to reduction difficulties with a particular image due to poor seeing, guiding errors or transparency fluctuation. After reduction a total of 4291 data points were collected for final analysis.

The gravitational microlensing target which is assumed to be a binary lensing event is observed between 5260.86264 $<$ HJD $<$5873.50203 and HJD-2450000.0 is the Heliocentric Julian Date at mid exposure.

University of Cape Town

Table 7.1: Observational data used

Telescope used	Telescope diameter	Filters	Time (HJD)	Number of points
SAAO	1.0 m	I	5749.260378 – 5790.448727	317
OGLE	1.3 m	I	5260.86264 – 5873.50203	3686
Perth	0.6 m	I	5738.99421 – 5760.12984	12
Canopus	1.0 m	I	5738.917747 – 5785.112483	43
LaSilla	1.54 m	I	5749.541276 – 5801.597230	233
Total				4291

University of Cape Town

7.3 Program Used for Data Analysis

For our microlensing data analysis, we used a FORTRAN program developed by Keith Horne called PLENS (http://star-www.stand.ac.uk/ ∼ kdh1 /plens/plens.html). PLENS is a FORTRAN code to fit light curves of a microlensing events. This code uses PGPLOT for graph plotting and it incorporates the following individual programs which work together for final microlensing fitting. The plens.exe contains all the executable images and plens.com is a script to compile PLENS. The other code which incorporates files with common blocks for global variables is plens.inc which includes files, sites, multi-site, site names, locations, data files, number of data points, χ^2 and degree of freedom, base line re-binning, site dependent parameters, noise model parameters, base line, source and blend fluxes, seeing and sky corrections, scope id and filter. In addition plot symbols and colors, seeing corrections, fluxes are incorporated in the program. The code also incorporates all the optimization schemes described in the appendix.

PLENS has main program known as plens.for with several subroutines lens1.for is a single lens subroutine, lens2.for is a binary lens subroutine, asp.for, dzw.for are multiple lens and detection zone subroutines respectively, misc.for is a miscellaneous subroutine which includes routines for data input and output, and time conversion, as well as subroutines from (Press et al., 1986) for complex root finding and for various simplex fitting methods. In this project we spent enormous amount of time and effort in trying to understand the program.

PLENS reads light curve data files with multi-column ASCII files with different

formats especially it reads data with default data file extension is .dat. It reads data formats ranging from 3 columns to 8 columns. It has also a feature to accept data points from single site to multiple observatories. If several site data points are considered for analysis, the data format should be arranged in such a way that it is compatible with the code with file extension .lis containing all sites considered.

PLENS point source point lens model uses PSPL magnification and impact parameters given earlier in chapter 2 equation 2.24 and 2.27. Regarding the flux (magnified source and blend) fitting PLENS uses the following equation:

$$F^k(t) = F_s^k A\{u(t)\} + F_b^k, \tag{7.1}$$

The three parameters used to do fitting are t_0, t_E, and u_0 which are non-linear parameters, parameters normalized with Einstein ring radius, and 2N linear parameters $F_s(i)$ and $F_b(i)$.

The program is compiled using an executable image plens.exe. But before execution we created .o files for all subroutines with .f extension so as to create plens.a by compiling all the .f files. Here we also created a folder to put all the subroutines so that the plens.exe will find all the subroutines.

After making all these files, we are in a position to feed the observed data from five different observatories to the program for analysis. Then after, a range of values for the mass ratio, q, and separation, d, were chosen for grid search. Since the geometry of the binary lens could be any type depending on the two parameters (d, q), we need a starting value for analysis. The following table, table 7.2 shows the relationship between the standard model parameter notation and the notations used in this work.

University of Cape Town

Table 7.2: Relation between Parameters

Standard parameter notations	Notation in this model	Description
d	u	planet-lens separation (R_E)
q	q	planet-lens mass ratio
σ	f	error bar scale
α	α	the angle between the line joining the binary axis and planet position measured from the y-axis
F_B	b	Blend flux
u_0	u_0	Impact parameter
F_0	m_0	Base line magnitude
t_E	t_E	Einstein Crossing time
t_0	t_0	Epoch of peak magnification

University of Cape Town

Now let us choose different values of u and q as q = 0.0001, 0.001, 0.005, 0.01, 0.015, 0.02, 0.025, 0.3, 0.035, 0.04, 0.045...0.75, 1 and u = 0.25, 0.5, 0.75, 1.0, 1.25, 1.5, 1.75, 2, 2.25, 2.5, 2.75, 3.0, 3.25, 3.5 for adequate sampling of the (u, q) space. We assumed that these values thoroughly covered the space so as to find the lowest χ^2 value in the grid. In the meantime searching all model parameters in this region can be achieved. For a fixed value of (u, q, α), where α is the azimuth of the planet measured from the y-axis, we tried to build a $\chi^2(u, q)$ map to identify the best fit model region in the (u, q) space. For further parameter refinement and searching best fit parameters, we took the coordinates (x, y) of the planet position, where we got the lowest χ^2. Then after considering the points where we got the local minima back to the main fitting program and editing the parameters for further refinement of the parameters by allowing all the parameters to vary so as to get the best fit model from the data that we are analyzing.

From randomly selected values of (u, q) for minimum χ^2 search, (u, q, α) = (1.5, 0.025, 165^o) is considered as a starting point for analysis. Then we obtained a local minimum and recorded the coordinates for further analysis. On the other hand, using the main program we made a $\chi^2(x, y)$ map for a planet moving in the grid x, y. The χ^2(x, y) map shown below shows in Fig.7.2 where the data points under consideration are able to rule out planets, or where there is an evidence of a planet. If the second scenario is happening, then the darker regions, where χ^2 is minimum puts the best fit planet location on the plot. We registered the coordinates so as

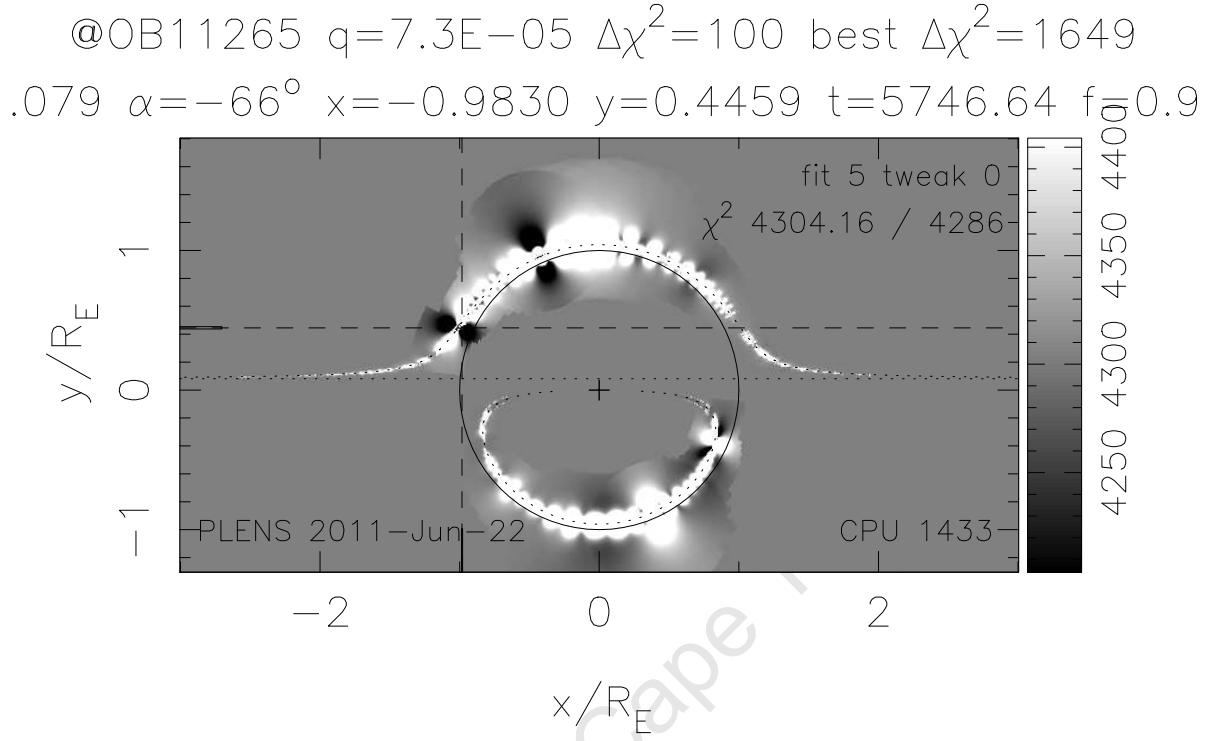

Figure 7.2: $\chi^2(x, y)$ with 4 free parameters and representation of a moving planet, where the darker regions are possible planet positions. The bigger circle is the Einstein Ring, the dashed lines passing over the Einstein Ring is the major image whereas the bowl shape inside the lower part of the Einstein Ring is the minor image. The lowest $\chi^2(x, y)$ is located where the two dashed lines meet perpendicularly close to the Ring at $(-0.9830, 0.4459)$. Further explanations of the figure can be found in the text below.

to put the value for further fitting procedures. From Fig. 7.2, the planet star mass ratio is 7.3×10^{-5} and it is easy to draw the fact that the values of the χ^2 decrease by 50 if one is moving to darker regions where planet signature is plausible whereas the values of χ^2 increase by 50 in the white regions where planet signature is ruled out. So $(x, y, \alpha) = (-0.9830, 0.4459, -66^o)$ is where the local minima is achieved, where the planet position (x, y) is measured in R_E.

The next step is to take this coordinate back to the main program and edit the parameters manually for further refinement. Allowing all the parameters to vary, one can get the best fit parameters.

University of Cape

8

Results, Discussion and Conclusions

University of Cape Town

8.1 Light Curve Fitting Strategies

The magnification for point-source point-lens microlensing events, as described earlier, is given by equation 2.24 whereas in order to model the light curve for such events, it is necessary to have the equation for the predicted flux which is given by:

$$F^k(t) = F_s^k A\{u(t)\} + F_b^k, \tag{8.1}$$

where F_s is the the source flux and F_b is the flux of any unresolved light (blend light) that is not being lensed. This flux, F_b, can be from the lens itself, or from any unresolved nearby stars or light from a companion to the lens (Gaudi, 2010). As Gaudi (2010) stated, to model light curves for ordinary microlensing events, it is important to consider the fluxes rather than the amplifications due to the fact that during real observations it is not the magnification but the flux of the photometrized source as a function of time is observed.

So, the observational data (flux as a function of time) are fitted to five free parameters: t_0, u_0, t_E, F_s and F_b. Since some of the parameters are degenerate, one

needs gross observable properties of the point-source point-lens microlensing event light curve such as t_{FWHM} (time for full width half maximum), t_0, the base and peak fluxes. Among the five parameters stated earlier, four (u_0, t_E, F_s and F_b) are highly correlated. Their correlation is even revealed on the light curve, because there is no significant difference on the light curves of single lens microlensing events plotted using different values of these parameters with the same values of the gross observables stated earlier.

During fitting observational data, because of parameter degeneracies stated earlier, it is worthwhile to consider an alternative way to parametrize these events by considering the gross observables (Gaudi, 2010). He stated that different observatory's during microlensing observations use different filter band passes. The amount of blended light is also dependent on the resolutions of the telescope under consideration. All these external factors affect the parameters that one uses for fitting single lens microlensing events. So, all external factors should be considered (source and blend fluxes for each observatories filter combinations) during fitting .

The total number of parameters is given by $N_{nl} + 2 \times N_0$, where N_{nl} is the number of parameters needed to show A(t) and N_0 is the number of independent data sets. From the expression given earlier, the observed flux is a linear function of F_s^k and F_b^k. So for N_{nl} parameters which are used to describe the amplification, one can obtain the source and blend fluxes using a least square fitting (Dominik, 2008; Gaudi, 2010).

In order to find the best fit model, it is possible to use hybrid methods such as Markov Chain Monte Carlo (MCMC), Downhill simplex or grid search so that the nonlinear parameters (u_0, t_0, t_E) are varied. Then the best fits F_s and F_b are easily obtainable for each trial of nonlinear parameters.

University of Cape Town

8.2 Lens Parameter Best Fit Results

In the previous chapter, we tried to show how the local minimum is achieved. The coordinates obtained from the local minimum, where possible planet signature is detected, were substituted back in the FORTRAN program for further analysis. Then fitting was done using amoeba downhill simplex method allowing all the parameters to vary for small iterations.

The table below, Table 8.1 shows the value of $\frac{\chi^2}{N-n}$. Consecutive decrement in the

Table 8.1: Values of $\frac{\chi^2}{N-n}$, where $N-n$ is the Degree of Freedom

$\frac{\chi^2}{N-n}$	Values	Description
$\frac{98072.188}{4291-4}$	22.876648	b_0 was 0.00 $\Longrightarrow$ −0.0077666
$\frac{46315.617}{4291-5}$	10.806257	sigmag0 was0.00 $\Longrightarrow$ 0.0575886779
$\frac{46227.586}{4291-6}$	10.788235	erbsc1 was 1.00 $\longrightarrow$ 1.3258587
$\frac{4326.1318}{4291-7}$	1.0098346	

values for different number of parameters is due to the fact that for five parameter fit, in the second row of the table, it uses the normal error bars as reported in the data files, whereas for six parameter fit it adds in quadrature an extra variance $sigma^2$ to the fluxes and scales the nominal error bars, $sigma\,i$ by a factor. These fits have parameters which in turn can change the error bars. So, the likelihood equation given in Eqn.9.11 (given in the appendix), $-2\,lnL(a_i)$ minimizes $\chi^2 + \sum_{i=1}^{N} ln\,\sigma_i^2$, where $\sigma^2 = \sigma_0^2 + (f\sigma_i)^2$, here σ_0 and f are considered to be two parameters, where σ_0 and f are base line flux accuracy in mag and $error\,bar\,scaling$ respectively. b_0, the blend flux, sigmag0, base line root mean square magnitude where its initial value was 0 because the four parameter fit for point-source point-lens microlensing model was done with no blending and erbsc1 is the error bar scale factor which initially was 1.00. The photometric programs that measure the brightness of the microlensing object also produce an estimate of the measurement error. These errors are generally based only on the counts detected in the star image. Other factors such as crowding, seeing, telescope focus and image shape may add extra errors. This is allowed for in the fitting program, where, in particular, a free parameter, f, is determined, that generally increases the error used in the calculation, to make χ^2 equal to 1.0 for each data set when the best fitting overall light curve is applied to it. In this way, data from different observatories obtained under different circumstances can be combined on an equal footing.

University of Cape Town

Table 8.2: Best Fit parameters obtained from the analysis of OGLE-2011-BLG-265

Parameters	Best fit values	Description
t_0	5760.2900 ± 0.018	time for Epoch of peak magnification
t_E	50.99 ± 0.025	Einstein crossing time
u_0	0.14 ± 0.036	Impact parameter
q	0.0042	mass ratio
u	1.034	Binary lens separation
A_0	7.25 ± 0.019	Peak magnification
m_0	1576 ± 0.023	Base line magnitude
t	5746.3500	Event time scale
α	$-63^o.00$	the angle from the +x-axis to the source path measured clockwise

Table 8.3: Best Fit parameters, f_s, f_0 obtained from the analysis of OGLE-2011-BLG-265

Parameters	Best fit values	Description
$f_s(AOB11265I)$	1.82 ± 0.0072	source flux measured at SAAO
$f_0(AOB11265I)$	1.80 ± 0.038	total base line flux
$f_s(OOB11265I)$	0.45 ± 0.00019	source flux measured by OGLE
$f_0(OOB11265I)$	0.44 ± 0.00011	total base line flux
$f_s(UOB11265I)$	3.90 ± 0.014	source flux measured at Canopus
$f_0(UOB11265I)$	21.42 ± 0.059	total base line flux
$f_s(WOB11265I)$	1.8 ± 0.0067	source flux measured at Perth
$f_0(WOB11265I)$	3.5 ± 0.031	total base line flux
$f_s(ZOB11265I)$	1.83 ± 0.013	source flux measured at La Silla
$f_0(ZOB11265I)$	1.8 ± 0.074	total base line flux

University of Cape Town

Tables 8.2 and 8.3 summarizes the parameters of the best fit model for the binary lens microlensing event. Using the outputs we got from the fit, we obtained the magnitude- residual light curve of the best possible solution of the data points analyzed with $\frac{\chi^2}{DOF} = \frac{\chi^2}{4291-7} = 1.01$, where $DOF = N - n$, N is the number of data points and n is the number of free parameters discussed before in the table 8.2. After refining the parameters we obtained best fit model with the following parameters: $q = 0.0042$, $u = 1.034$ and peak magnification of $A_0 = 7.25 \pm 0.019$ achieved at epoch time $t_0 = 5760.29$. The base-line magnitude of the event $m_0 = 15.76 \pm 0.023$ with Einstein crossing time of $t_E = 50.99$ days. The values of the source flux should have the same value for different observatories, but we got different values. This can be due to the seeing effect, sky background and the sensitivity of the CCD used for observation.

The light curve shown below in Fig 8.1 shows the magnification with time for microlensing event observed from 5 observatories. In the upper panel, the data points labeled by black are from the South African Astronomical Observatory and covers the target soon after the anomaly finished its peak. It also covers some part after the peak magnification with Base line magnitude, unmagnified $m_0 = 15.76 \pm 0.023$ with source flux $f_s(AOB11265I) = 1.82 \pm 0.0072$ and $f_0(AOB11265) = 1.81 \pm 0.038$, is the base line (unlensed flux). Later in the process, it picks a maximum magnification of 7.25 ± 0.019. Most of the data points in the light curve are coming from the OGLE 1.3m, Warsaw University Telescope in Las Campanas. The OGLE data, (OB11265I), points covered the target from the beginning, the anomaly, the peak magnification as well as the later stage of the event till the end. By considering the SAAO base line magnitude as a reference, the analysis of this data showed a change in magnitude of $m - m_0 = -1.5$ with $f_s = 0.45 \pm 0.00019$mag and $f_0 = 0.44 \pm 0.00015$mag. The data were modelled using a FORTRAN program developed by Keith Horne. The figures in this chapter are obtained from this program and although satisfactory for the present purpose, do not reproduce well.

University of Cape Town

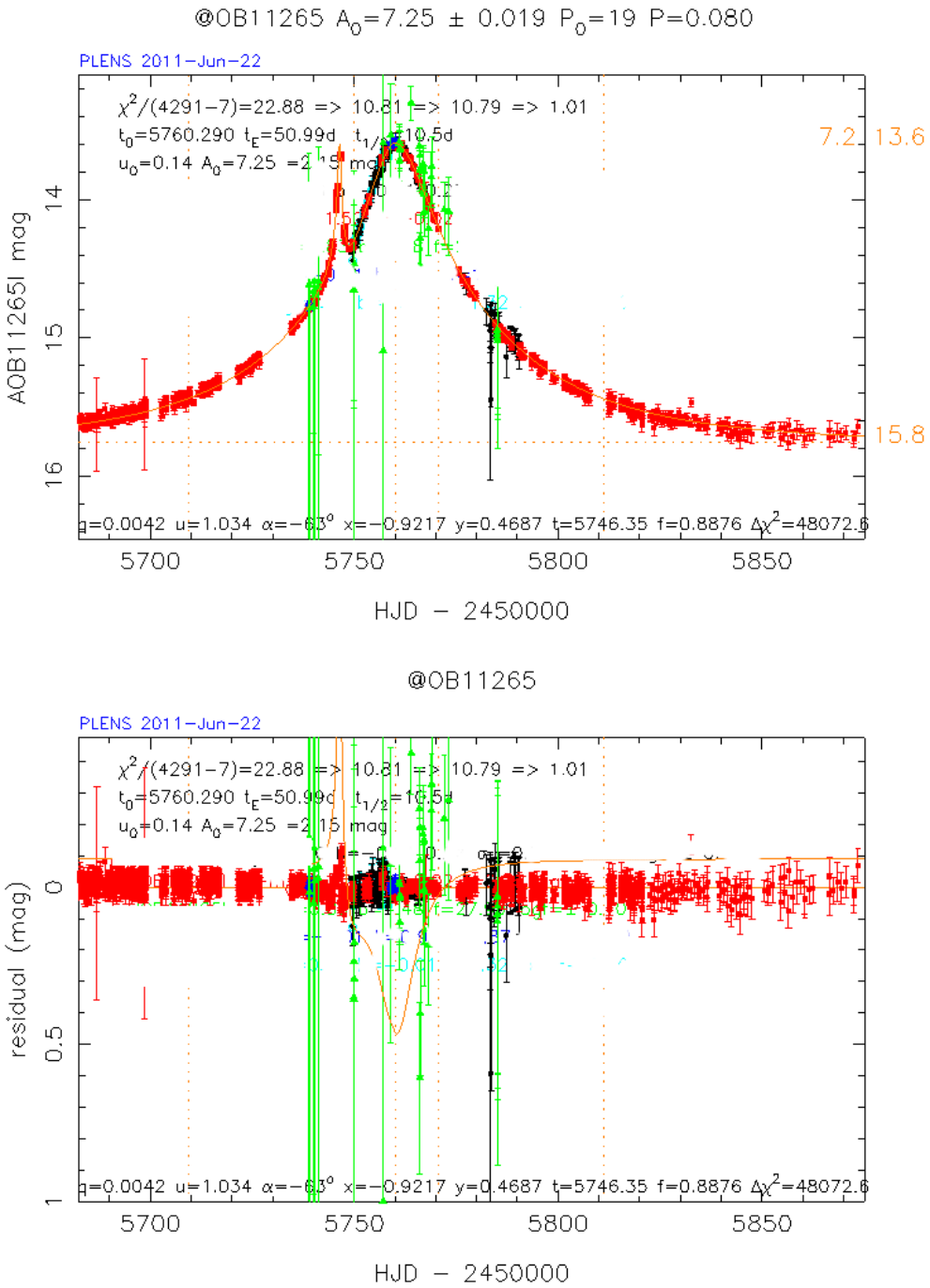

Figure 8.1: Best fit light curve for OGLE−2011-BLG-265 showing amplification with HJD and the lower panel showing residual. For detail explanation refer the text below.

The data points denoted in green are obtained from Canopus Telescope covering immediately before the anomaly, at the peak of magnification and just down the exit from the peak magnification with $m-m_0 = 0.83$ with blend flux, $b = \frac{F_{source\,flux}}{F_{total\,base\,line\,flux}}$, $b = 4.48$ and $f_s = 3.91 \pm 0.014$, $f_0 = 21.421 \pm 0.059$. The remaining two sets of data points are from Perth Observatory, blue points which has $m-m_0 = -0.01$ and blend flux of 0.94 with $f_s = 1.8 \pm 0.0068$, $f_0 = 3.5 \pm 0.031$. La Silla, labelled by cyan, cover quite few parts on the light curve with $f_s = 1.83 \pm 0.013$, $f_o = 1.81 \pm 0.074$ and blend flux of -0.01 with error bar scale of 1.33. Smith et al. (2007) stated that those data points with blend flux, $b = 1$ are not affected by blending whereas for b approaching 0 the observation is highly affected by blending.

The planetary signal (anomaly) is not well covered as shown in the light curve Figs.8.1 and Fig. 8.3. Only OGLE data covered the beginning of the anomaly very well but as the anomaly increases there should be intensive monitoring of the target but in this case it is not well covered. This results in some uncertainties in the output of the final fitting.

From the χ^2 map set up earlier the planet detection zone with lowest χ^2 was located at $(x, y) = (-0.9830, 0.4459)$. Using this coordinate for the final planetary microlensing fitting and parameters refinement, we obtained the position where the best fit model is achieved.

This planetary signal coordinate is found to be at $(x, y) = (-0.9217, 0.4687)$ with error bar scale $f = 0.8876$, where this value is the uncertainty in the data. The angle from the +x-axis to the source path, measured clockwise, after refining the parameters is $\alpha = -63^o$. Using the final best fit parameters $u = 1.034$ and $q = 0.0042$, on which the structure of the binary depends, the best fit is plotted in Fig. 8.2 using the Dominik (2007) formalism.

University of Cape Town

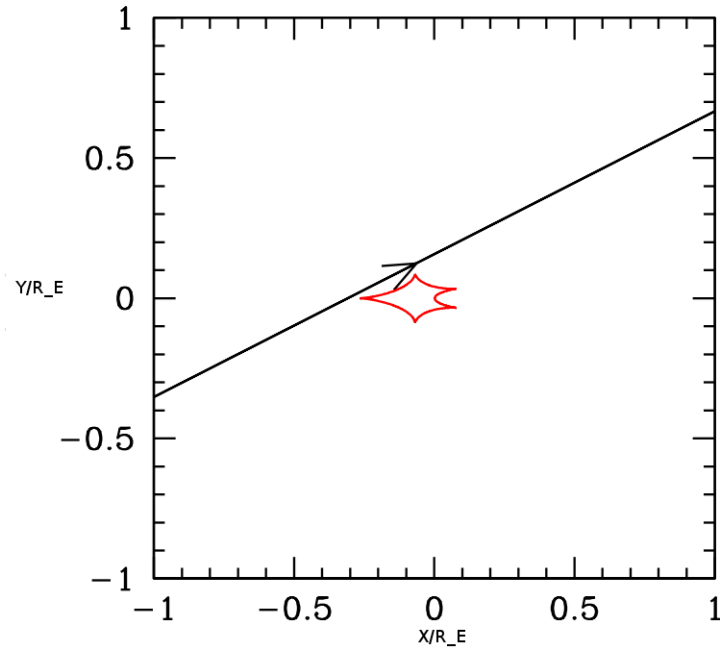

Figure 8.2: Configuration of the caustic curve for the binary microlensing lensing with source path for the event, OGLE-2011-BLG-265 with planetary signal of mass ratio q = 0.0042 and separation u = 1.034. Where the planet is located on the -x-axis supposed to be on the left side of the caustic structure where as the host star is on the + x-axis situated on the right side of the caustic.

The figure shown in Fig.8.2 is plotted using the best fit parameters. Here the angle we used for this plot is obtained from the coordinates where planet signature anomaly is observed, $(x, y) = (-0.9217, 0.4687)$. From trigonometry, we have $tan^{-1}\frac{y}{x} = tan^{-1}(-0.508) = -26.95^{o}$'. This angle is measured anticlockwise from the y-axis, and describes the relation between the source path and the line from the host star to the planet (x-axis. From Fig.8.2, it is possible to draw the fact that as the source passes close to the caustics it becomes magnified for brief amount of time as shown in the light curve of Fig.8.3, where the model light curve plotted in yellow solid line. As the source follows its path for short period of time there will be a maximum magnification as seen in Fig.8.3. Then, as the source moves away from the caustics it results in the decrease in magnification and its effect will be reduced as time goes on.

University of Cape

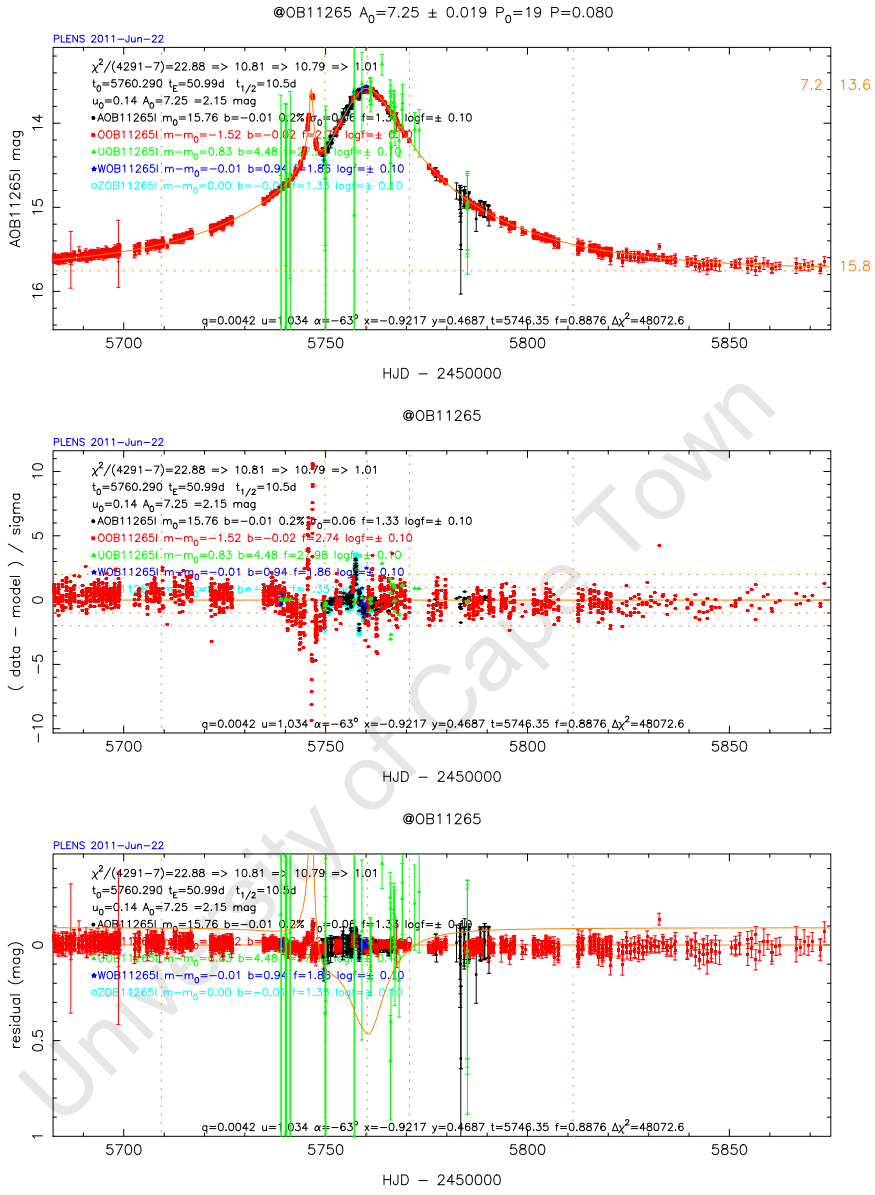

Figure 8.3: Figure showing best fit microlensing events: Upper panel: Best fit light curve of planetary signal microlensing event, Middle panel: Normalized residuals ($\frac{Data-model}{\sigma}$) plotted with respect to time and lower panel: Residual (Data- model), the deviation from the best fit model, having either positive or negative values depending on the deviation of the data points from the curve either above or below respectively, of the target , OGLE-2011-BLG-265, under consideration after fitting.

University of Cape Town

A planetary microlensing anomaly, as described by Horne et al. (2009), can be revealed on the light curve with a short duration hump. Horne et al. (2009) explained the relation between the planet's Einstein ring radius with Einstein ring radius R_E as well as the duration of the planet anomaly with the Einstein crossing time t_E using:

$$r_p = R_E q^{\frac{1}{2}}, \tag{8.2}$$

where r_p is planet Einstein ring radius and R_E is the Einstein ring radius

$$t_p = t_E q^{\frac{1}{2}}, \tag{8.3}$$

where t_p is duration of planetary anomaly, the time the planet needs to cross the diameter of the planet's Einstein ring, and t_E is Einstein crossing time.

Using the relations derived in equation 8.3, the Einstein crossing time for our best fit model is found to be $t_E = 50.99$ days with mass ratio $q = 0.0042$. We also obtained the duration of the anomaly, where the image of the source crosses the planet Einstein ring radius, to be

$$50.99 days \times 0.0042^{\frac{1}{2}} = 3.3045\, days. \tag{8.4}$$

Intensive monitoring of the target is required to get sufficient data points and monitoring the anomaly is fundamental to detect extrasolar planets. In our case the anomaly is a planetary signal where the planet acts as a lens. From the separation distance of the host star and the planet $u = 1.034$, it is easy to draw the fact that the binary lens will fall in the intermediate binary lens range, as it was explained in Section 4.3.

University of Cape Town

8.3 Conclusions

This project entitled, "Gravitational Microlensing and the Search for Extrasolar Planets", covered the theoretical aspects of gravitational lensing, microlensing and higher order effects related to microlensing such as finite- source effect.

By introducing some parameter minimization schemes and algorithms and applying them to real observational data from the microlensing event OGLE-2011-BLG-265, we concluded that the light curve is best described by a binary lens microlensing event with a planetary companion of mass ratio of $q = 0.0042$. According to Bond et al. (2004), the light curves of binary microlensing events allow much more accurate determination of the mass ratio than the mass of the individual components. They also described the criterion of the binary lens components based on the mass ratio. A planetary microlensing events therefore are characterized by a mass ratio $q < 0.03$ (Bond et al., 2004). It follows that, the microlensing target we analyzed, OGLE-2011-BLG-265 is under planet microlensing event with a planet Einstein ring crossing time of 3.30 days, which strengthens our conclusion of the existence of planetary companion.

University of Cape Town

8.4 Suggestions and Future Prospect of the Project

The FORTRAN code we used to fit microlensing events is not complete because it does not include some higher order effects such as the finite source effect discussed in chapter 2. Moreover in this fitting code binary source microlensing effects, parallax, xallarap effects (A microlensing effect caused by the orbital motion of the source star where the source star has a binary orbit or xarallap is the inverse effect of parallax) are not included. So the code can be more complete if the afore-mentioned higher order microlensing effects are included. The result of our fit is not exact solution due to the exclusion of some higher order microlensing effects giving error bars in our fitted curve. So, large error bars due to the higher order effects can be removed and there is a possibility of getting a much better fitting and reliable parameter outputs which can explain the microlensing target under study very well.

In the future, FORTRAN codes will be developed which can include higher order effects to be incorporated with the existing codes plens.for, which is developed by Keith Horne.

University of Cape Town

9 Appendix

University of Cape Town

9.1 Important Optimization Techniques Used for Microlensing Fitting

The purpose of this section is to give an overview of the algorithms we used in microlensing fitting. These algorithms help one to find the parameters which can best describe the observational data that we have at hand. Modelling microlensing, especially binary lense events, is more challenging due to the fact that the parameters have a large dynamic range. For example the mass ratio $0 < q \leq 1$ and the separation distance is $0 < d < \infty$. This makes the standard χ^2 goodness of fit measure of the complicated high dimensional parameter space very sensitive to small changes in the parameters (Kubas et al., 2005).

For a given set of observational data, one can try to analyse and fit to the model so as to get relevant information from the observed data and study the nature of the microlensing event. So in order to do fitting, it is better to have some statistical knowledge so as to understand the events under consideration. This can be done by calculating the statistical measures of the goodness of the fit which is described by

the χ^2 measure.

As Press et al. (1986) stated for a model function given by $y(x) = \Sigma_{k=1}^{M} a_k X_k(x)$ where X_k is fixed function of x, assuming that this expression is a linear model in which the model depends on the parameters a_k, χ^2 can be defined as:

$$\chi^2 = \Sigma_{i=1}^{N} (\frac{y_i - \Sigma_{k=1}^{M} a_k X_k(x_i)}{\sigma_i})^2, \tag{9.1}$$

where σ_i is measure of error (standard deviation) and N is the number of data points. A close study of the calculated values will have a magnitude of the order of N since each value of the sum is expected to have a value very close to 1(Kane, 2000). This relation will tell us how good/bad our fit is. For example, if the value of χ^2 is much greater than the number of data points, the deviation of the fit from the model is significantly high and results in poorly fitted data. On the other hand, if the χ^2 is much less than N, the error is over-estimated and results in over-fit to the model. Let us introduce $DOF = N - n$, by taking into account the number of free parameters under consideration leading to calculate the number of degrees of freedom, where n is the number of free parameters and N is the total number of data points. So the resulting value, $\frac{\chi^2}{DOF}$, is known as reduced value of χ^2. The reduced χ^2 will have a value closer to 1 for best fit model.

$$\chi^2_{reduced} = \frac{\chi^2}{N - n}. \tag{9.2}$$

After defining some terms which are very important for further analysis, we are in a position to describe some of the most commonly used minimisation techniques.

9.1.1 Downhill Simplex Method

The downhill simplex method introduced by Nelder and Mead in 1965 is a multidimensional minimization, which helps to determine the minimum of the function of more than one independent variables (Press et al., 1986). Downhill simplex method is easy for implementation and is quick and robust.

To understand the downhill simplex method consider an N dimensional space consisting of $N+1$ points or vertices and the lines joining these points, which are called simplexes. In a two dimensional space, a simplex is a triangle on the other hand for a three dimension the simplex is a tetrahedron. In order to study the downhill

University of Cape Town

simplex method, one must focus on simplexes which are not degenerate. Non degenerate simplexes are the ones that enclose a finite inner N-dimensional Volume (Press et al., 1986).

For a multi dimensional minimization, it is better to give an N vector of independent variable as an initial or starting guess. Since the algorithm is supposed to make its own way down hill through an N dimensional space until it reaches to the local minimum (Press et al., 1986).

Regarding the starting point for this method, it is possible to take not only from a single point but also from $N + 1$ points by defining an initial simplex .

If one starts searching the local minima by considering a starting point P_0 in n-dimensional model parameter, it is possible to take other N points by $P_i = P_0 + \lambda e_i$, where e_i is a unit vector and λ is a constant of the guess characteristic length scale (Press et al., 1986). After setting the initial guesses the downhill simplex method takes a series of steps by jumping from the highest point to the lowest point on the other side of the simplex as it is shown in Fig.9.1. In doing so the volume of the geometric simplex is conserved maintaining its non-degeneracy. The following figure Fig.9.1 summarizes the possible ways of moving to find the local minimum where the difference between vertices falls well below a given tolerance.

University of Cape Town

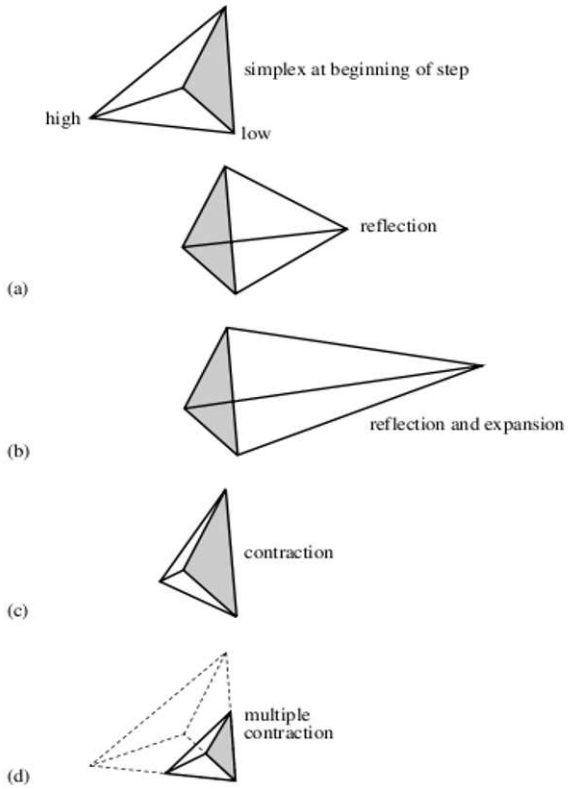

Figure 9.1: Possible ways of movement in Downhill simplex method during finding a local minima (Adapted from Press et al., 1986).

In Fig.9.1, the starting simplex for the downhill method is a tetrahedron. After applying downhill simplex method, one of the possible results can be the outputs displayed in the figures a, b, c, or d.

9.1.2 Maximum Likelihood

If one is doing fitting to a model having M adjustable parameters a_j with N data points, the model predicts let us say

$$y(x_i) = y(x_i; a_1, ...a_M), \tag{9.3}$$

minimizing the equation over the parameters $a_1, ..a_n$, $\Sigma_{i=1}^{N}[y_i - y(x_i; a_1, ...a_M)]^2$ where the equation on the right side shows the dependence of the parameters. So here obtaining the parameters using this method basically depends on the probability where the data must not be too improbable for the correct choice of the parameters. Maximum likelihood is a more intuitive method. The basic principle in maximum likelihood fitting procedure is for a collection of N events which corresponds to an independent variable x_i and dependent variable y_i. The target is to obtain the set of parameters $a_1...a_m$ of a function given earlier. So the model function can be converted to normalized probability density function (Bevington & Robinson, 1992):

$$P_i = P(x_i; a_1, a_2...a_m). \tag{9.4}$$

Assuming Gaussian distribution for the measurement of the error around the true model $y(x)$ and assuming that σ, the standard deviation, is the same for all points, then the probability of the data set is given by:

$$P \propto \Pi_{i=1}^{N} exp[\frac{1}{2}(\frac{y_i - y(x_i)}{\sigma})^2]\Delta y, \tag{9.5}$$

where the term $(\frac{y_i - y(x_i)}{\sigma})^2 = \chi^2$ and the probability density can be written as:

$$P \propto \Pi_{i=1}^{N} e^{\frac{-1}{2}\chi^2}\Delta y, \tag{9.6}$$

where Δy is a fixed value to be added or subtracted on each data point to make sure that the probability is different from zero when the value of y_i takes continuous values.

Then maximizing this equation is equivalent to maximizing its logarithm, or minimizing its negative logarithm

$$lnP = [\Sigma_{i=1}^{N} \frac{(y_i - y(x_i))^2}{2\sigma^2}] - Nlog\Delta y, \tag{9.7}$$

University of Cape Town

where N, Δy and σ are constants implying minimizing this equation, Eqn.9.7 is equivalent to maximizing $\Sigma_{i=1}^{N}[y_i - y(x_i; a_1, ...a_M)]^2$. From the discussions above one can see that if the measured errors are independent and normally distributed with constant σ, the least square fitting is maximum likelihood (Press et al., 1986).

Authors like Cassan et al. (2010) also stated that the likelihood is a function of parameters a_i and a probability distribution over the data D. so,

$$L(a_i) = P(D|a_i) = \frac{e^{\frac{-1}{2}\chi^2}}{(2\pi)^{\frac{N}{2}}\Pi_{i=1}^{N}\sigma_i}, \tag{9.8}$$

where P(D|a_i) is the likelihood, which is a function of the parameters a_i and a probability distribution over the data D.

As stated earlier, maximizing $L(a_i)$ corresponds to minimizing the negative logarithm as:

$$lnL(a_i) = lne^{\frac{-1}{2}\chi^2} - [ln(2\pi)^{\frac{N}{2}}\Pi_{i=1}^{N}\sigma_i], \tag{9.9}$$

$$lnL(a_i) = \frac{-1}{2}\chi^2 - [\frac{N}{2}ln2\pi + \Sigma_{i=1}^{N}ln\sigma_i], \tag{9.10}$$

$$-2lnL(a_i) = \chi^2 + Nln2\pi + 2\Sigma_{i=1}^{N}ln\sigma_i. \tag{9.11}$$

So from this expression above the maximum likelihood is equivalent to a minimum in χ^2, when σ_i, the error bar, is known. This formalism, on the other hand, is a Bayesian analysis which implicitly assumes prior that is uniform on the chosen parameter interval (Cassan et al., 2010).

University of Cape Town

9.1.3 Bayesian Statistics and Priors

The frequentist school of thought defines probability as "the number of times an event occurs over the total number of trials, in the limit of an equi-probable repetitions" (Trotta, 2008). This definition has some limitations in explaining probability. Among others, this theory assumes that repeated trials have the same probability and it also lacks to explain the probability of unrepeated events. In addition, the definition holds true for an infinite sequence of repetitions whereas in general practice statistical analysis is all about finite number of measurements. These shortcoming can be avoided by taking a Bayesian stance on the definition. The definition of probability from Bayesian statistics point of view is "a measure of the degree of belief about a proposition" (Trotta, 2008). This definition in general holds true for any event.

Bayes' statistics has advantage over the frequentist view in real life cases in such a way that this method deals with nuisance parameters, parameters which have an effect on the data but not important for us. The other important point in Bayesian analysis is the prior information has significant importance during analysis. This method also deals with event data which are observed unlike frequentist results that depend on what the experimenter thinks about the probability of data that have not been observed.

University of Cape Town

9.1.4 Bayes' Theorem

As Loredo (1992) stated, statistical knowledge plays a major role in astrophysics in such a way that understanding and explaining the concepts of astrophysics need to know the principles of inference which in turn helps how to extract relevant information from observational data and how theoretical predictions or models can be compared with the observational data. Bayes' theorem is a simple generalization of the probability theory. Bayes' theorem, as stated in (Trotta, 2008), can be derived from a set of consistency requirements for convincing reasoning called cox axioms. So Bayesian statistics interference is the generalization of logical deduction when the information available is incomplete.

Before heading to the mathematical development of Bayesian statistics, let us give an overview of some of the probability rules. Consider a proposition Q and its negation $\bar{Q}$, then:

Addition rule

$$P(Q|S) + P(\bar{Q}|S) = 1, \tag{9.12}$$

where P(Q|S) is probability of Q occurring on its own from the information provided in S.

Product rule

$$P(Q, R|S) = P(Q|R, S)P(R|S), \tag{9.13}$$

which is defined as the joint probability of Q given that R occurs times the probability of R occurring on its own. If we want to study the probability of R irrespective of Q both the rules stated earlier will give as:

$$P(R|S) = \Sigma_Q P(Q, R|S), \tag{9.14}$$

where $P(R|S)$ is marginal probability of R. The other thing that we should be aware of is $P(Q, R|S) = P(R, Q|S)$, then the product rule will lead us in deriving the Bayes' theorem:

$$P(R|Q, S) = \frac{P(Q|R, S)P(R|S)}{P(Q|S)}. \tag{9.15}$$

Simple substitution of Q by the observed data d and R by the hypothesis H,

$$P(H|d, S) = \frac{P(d|H, S)P(H|S)}{P(d|S)}, \tag{9.16}$$

where $P(H|d, S)$ is the posterior probability of the hypothesis, which is proportional to the sampling distribution of the data $P(d|H, S)$ assuming the hypothesis is true, times the prior probability of the hypothesis $P(H|S)$. This prior is any external information we have, S, which represents one's state of knowledge before having the data (Trotta, 2008).

In Bayesian statistics the prior choice is the most fundamental ingredient for further inference. In microlensing analysis (Cassan et al., 2010) Bayes parameter estimation takes into account the prior distribution of the parameter space (q, d). So the posterior probability distribution in Bayes' analysis is a function of the data. Hence

University of Cape Town

$$P(\theta|D) = \frac{P(D|\theta)P(\theta)}{\int P(D|\theta)P(\theta)d\theta}, \tag{9.17}$$

where $P(\theta)$ is the prior probability distribution on the parameter θ, and $P(D|\theta)$ is the likelihood which is a function of θ. Here one should notice that as a function of the hypothesis the likelihood is not a probability distribution (Trotta, 2008) because the denominator in equation 9.17 is a normalization constant.

9.1.5 Parameter Grid Search

Binary microlensing could have any geometry depending on two parameters (d,q) with $0 < d < \infty$ and $0 < q \leq 1$. So in order to get the required parameters from observational data in microlensing we are going to fix the two parameters d and q and try to build $\chi^2(d, q)$ grid that we are going to locate the best fit region (Kains et al., 2009).

Bevington & Robinson (1992) described that grid search method can be used for parameters in which the variation of χ^2 with each parameter a_j is not very sensitive to the magnitudes of the other parameters. Then the optimum parameter values can be obtained by minimizing χ^2 with respect to each of the parameters separately.

The following summarizes the grid search method as is stated in Bevington & Robinson (1992):

(a) Select a starting point for the parameters a_j with Δa_j increment for each parameter, then calculate the value of χ^2 with the starting parameters.

(b) In the second step increase one of the parameters by $\pm\Delta_j$ and calculate χ^2 and notice the sign change so that χ^2 decreases.

(c) The second step is repeated until χ^2 stops decreasing and starts to increase

(d) Using the last value of the parameter a_j and its χ^2 to determine the minimum.

(e) Minimize χ^2 again with respect to each parameter.

(f) Repeat the procedure until the last iteration yields a predefined negligibly small decrease in χ^2.

Parameter grid search method is advantageous because it is simple to implement and helps to get the absolute minimum of the χ^2 function in parameter space with precision. This method, on the other hand, has some limitations where the variation

University of Cape Town

in χ^2 with the parameters is strongly correlated which makes the process of getting the absolute minimum very slow.

9.1.6 Parameter Covariance Matrix: Parameter Error Bars

In this subsection, we are going to show the relation between the covariant matrix and Hessian matrix by considering a model function which is going to be fitted in the form $y = y(x; a)$. By defining a χ^2 merit function as $\chi^2(a) = \Sigma_{i=1}^{N}[\frac{y_i - y(x_{i;a})}{\sigma_i}]^2$ and taking the first derivative of the χ^2 with respect to the parameter under consideration, 'a':

$$\frac{\partial \chi^2}{\partial a_k} = -2\Sigma_{i=1}^{N}\frac{[y_i - y(x_i; a)]}{\sigma_i^2} \times \frac{\partial y(x_i; a)}{\partial a_k}, ...k = 1, 2...M. \tag{9.18}$$

Taking the partial derivative of the above equation (Eqn.5.18) gives us:

$$\frac{\partial^2 \chi^2}{\partial a_k \partial a_l} = 2\Sigma_{i=1}^{N}\frac{1}{\sigma_i^2}[\frac{\partial y(x_i; a)}{\partial a_k}\frac{\partial y(x_i; a)}{\partial a_l} - (y_i - y(x_{i;a}))\frac{\partial^2 y(x_i; a)}{\partial a_l \partial a_k}]. \tag{9.19}$$

Defining $\alpha_{kl} = \frac{1}{2}\frac{\partial^2 \chi^2}{\partial a_k \partial a_l}$ and $\beta_k = \frac{-1}{2}\frac{\partial \chi^2}{\partial a_k}$, then the value of α_{kl} is going to be the Hessian matrix which depends on the first and second derivatives of the basis function with respect to their parameters (Press et al., 1986). The Hessian matrix,

$$H_{kl} = \frac{\partial^2 \chi^2}{\partial a_k \partial a_l}, \tag{9.20}$$

is symmetric. So, the covariance matrix of the parameters under consideration is given by

$$cov(a_k, a_j) = [\frac{\partial^2 \chi^2}{\partial a_k \partial a_l}]^{-1} = [H]^{-1} \tag{9.21}$$

The higher order term $\frac{\partial^2 \chi^2}{\partial a_k \partial a_l}$ with $y_i - y(x_i; a)$ can be neglected when it is compared to the term containing the first derivative because for good and successful model this term is the measurement of the error for each point and in general not related to the model hence resulting in the cancellation of the higher order term when summed over all i. As Press et al. (1986) stated, the value of the matrix $\alpha_{kl}(H_{kl})$ has no effect at all on the final value of parameters 'a' reached, whereas it affects the iterative root that

University of Cape Town

is passed to reach the final value. Covariance matrix captures the variance and linear correlations in multidimensional data. If a data under investigation is N×M matrix, the covariance matrix reduces the number of columns loosing a minimal information and giving a (c×c) square matrix. So the matrix given above in equation 5.21 is related with the standard uncertainties of the parameters estimated (Press et al., 1986).

University of Cape Town

Bibliography

Albrow M., Beaulieu J.-P., Birch P., Caldwell J. A. R., Kane S., Martin R., Menzies J., Naber R. M., Pel J.-W., Pollard K., Sackett P. D., Sahu K. C., Vreeswijk P., Williams A., Zwaan M. A., The PLANET Collaboration 1998, ApJ, 509, 687

Alcock C., Akerlof C. W., Allsman R. A., Axelrod T. S., Bennett D. P., Chan S., Cook K. H., Freeman K. C., Griest K., Marshall S. L., Park H.-S., Perlmutter S., Peterson B. A., Pratt M. R., Quinn P. J., Rodgers A. W., Stubbs C. W., Sutherland W., 1993,

Alcock C., Allen W. H., Allsman R. A., Alves D., Freeman K. C., Gregg M. D., Griest K., Hearnshaw J. B., The Macho Gman Collaborations 1997, ApJ, 491, 436

Alcock C., Allsman R. A., Alves D., Axelrod T. S., Becker A. C., Bennett D. P., Cook K. H., Drake A. J., Stetson P. B., Stubbs C. W., Sutherland W., Tomaney A., Vandehei T., 1999, ApJ, 518, 44

An J. H., Albrow M. D., Beaulieu J.-P., Caldwell J. A. R., DePoy D. L., Dominik M., Gaudi B. S., Gould A., Greenhill J., Hill K., Kane S., Martin R., Menzies J., Pogge R. W., Pollard K. R., Sackett P. D., Sahu K. C., Vermaak P., Watson R., Williams A., 2002, ApJ, 572, 521

Aubourg E., Bareyre P., Brehin S., Gros M., Lachieze-Rey M., Laurent B., Lesquoy E., Magneville C., Milsztajn A., Moscoso L., Queinnec F., Rich J., Tajahmady F., Maurice E., Prevot L., Gry C., 1993, The Messenger, 72, 20

Auvergne M., Bodin P., Boisnard L., Buey J.-T., Wallner R., Waultier G., Zanatta P., 2009, A&A, 506, 411

University of Cape Town

Batista V., Gould A., Dieters S., Dong S., Bond I., Beaulieu J. P., Maoz D., Monard B., RoboNet Collaboration Allan A., Bramich D. M., Snodgrass C., Steele I. A., Street R. A., 2011, A&A, 529, A102

Beaulieu J.-P., Bennett D. P., Fouqué P., J. D., Tristram P. J., Yock P. C. M., Yoshioka T., 2006, , 439, 437

Bennett D. P., 2010, ApJ, 716, 1408

Bennett D. P., Bond I. A., Udalski A., Sumi T., Abe F., Fukui A., Furusawa K., Hearnshaw J. B., Marquette J. B., 2008, ApJ, 684, 663

Bevington P. R., Robinson D. K., 1992, Data reduction and error analysis for the physical sciences. New York: McGraw-Hill, 2nd ed.

Bond I. A., Udalski A., Jaroszyński M., Rattenbury N. J., Paczyński a. O., 2004, ApJL, 606, L155

Bond I. A., Udalski A., Jaroszyński M., Rattenbury N. J., Paczyński B., Soszyński I., OGLE Collaboration 2004, ApJL, 606, L155

Borucki W. J., Koch D., Kepler Science Team 2010, in AAS/Division for Planetary Sciences Meeting Abstracts #42 Vol. 42 of Bulletin of the American Astronomical Society, Kepler Planet Detection Mission: Highlights of the First Results. p. 1052

Bozza V., Calchi Novati S., Mancini L., Scarpetta G., 2011, ArXiv e-prints:1102.0452

Cassan A., 2008, A&A, 491, 587

Cassan A., Horne K., Kains N., Tsapras Y., Browne P., 2010, A&A, 515, A52+

Chang H.-Y., Han C., 2001, MNRAS, 327, 397

Chang K., Refsdal S., 1984, A&A, 132, 168

Dominik M., 1999, A&A, 349, 108

Dominik M., 2007, MNRAS, 377, 1679

University of Cape Town

Dominik M., 2008, in Manchester Microlensing Conference "Modelling Microlensing Events", in Proceedings of the Manchester Microlensing Conference: The 12th International Conference and ANGLES Microlensing Workshop, eds. E. Kerins, S. Mao, N. Rattenbury and Ł. Wyrzykowski. Published online at SISSA, Proceedings of Science.,p.8

Dong S., Bond I. A., Gould A., Kozłowski S., Miyake N., Gaudi B. S., Bennett D. P., Abe F., Ulaczyk K., OGLE Collaboration 2009, ApJ, 698, 1826

Doyle L. R., 2008, in H. Deeg, J. A. Belmonte, & A. Aparicio ed., Extrasolar Planets Overview of extrasolar planet detection methods. p. 1

Ehlers J., Schneider P., 1993, in R. J. Gleiser, C. N. Kozameh, & O. M. Moreschi ed., General Relativity and Gravitation 1992 Gravitational lensing. p. 21

Endl M., MacQueen P. J., Cochran W. D., Brugamyer E. J., Bryson S., Howell S. B., Fortney J. J., Hansen T., Smith J. C., Thompson S. E., Twicken J. D., 2011, ApJS, 197, 13

Erdl H., Schneider P., 1993, A&A, 268, 453

Fukui A., Abe F., Ayani K., Fujii M., Iizuka R., Itow Y., Kabumoto K., Kamiya K., Kawabata T., Kawanomoto S., Kinugasa K., Koff R. A., Krajci T., Naito H., Nogami D., Narusawa S., Ohishi N., Ohnishi K., Sumi T., Tsumuraya F., 2007, ApJ, 670, 423

Gaudi B. S., 2010, ArXiv e-prints: 1002.0332

Gaudi B. S., Bennett D. P., Udalski A., Gould A., Chaboyer B., Crocker A., Frank S., Macintosh B., 2008, Science, 319, 927

Gould A., 1994, ApJL, 421, L71

Gould A., 1997, ApJ, 480, 188

Gould A., 2009, in K. Z. Stanek ed., The Variable Universe: A Celebration of Bohdan Paczynski Vol. 403 of Astronomical Society of the Pacific Conference Series, Recent Developments in Gravitational Microlensing. p. 86

Gould A., Loeb A., 1992, ApJ, 396, 104

University of Cape Town

Gould A., Udalski A., An D., Bennett D. P., Zhou A.-Y., Dong S., Rattenbury N. J., Gaudi B. S., Mao S., Swaving S. C., 2006, ApJL, 644, L37

Griest K., 1991, ApJ, 366, 412

Han C., Hwang K.-H., 2009, ApJ, 707, 1264

Horne K., Snodgrass C., Tsapras Y., 2009, MNRAS, 396, 2087

Hwang K.-H., Udalski A., Han C., Ryu Y.-H., μFUN Collaboration 2010, ApJ, 723, 797

Janczak J., Fukui A., Dong S., Monard L. A. G., Kozłowski S., Gould A., Beaulieu J. P., PLANET Collaboration 2010, ApJ, 711, 731

Jaroszyński M., Mao S., 2001, MNRAS, 325, 1546

Jaroszyński M., Udalski A., Kubiak M., Szymanski M., Pietrzynski G., Soszynski I., Zebrun K., Szewczyk O., Wyrzykowski Ł., 2004, , 54, 103

Kains N., Cassan A., Horne K., Albrow M. D., Ulaczyk K., Wyrzykowski Ł., 2009, MNRAS, 395, 787

Kane S. R., 2000, PhD thesis, University of Tasmania

Klimov Y. G., 1963, Soviet Physics Doklady, 8, 119

Kubas D., Cassan A., Beaulieu J. P., Coutures C., Vinter C., Wambsganss J., Watson R., Williams A., Thurl C., 2005, A&A, 435, 941

Lee C.-H., Riffeser A., Seitz S., Bender R., 2009, ApJ, 695, 200

Liebes S., 1964, Physical Review, 133, 835

Loredo T. J., 1992, in E. D. Feigelson & G. J. Babu ed., Statistical Challenges in Modern Astronomy Promise of Bayesian inference for astrophysics.. pp 275–306

Mao S., 2008, in Manchester Microlensing Conference "Introduction to Microlensing", in Proceedings of the Manchester Microlensing Conference: The 12th International Conference and ANGLES Microlensing Workshop, eds. E. Kerins, S. Mao, N. Rattenbury and Ł. Wyrzykowski. Published online at SISSA, Proceedings of Science., p.2

University of Cape Town

Mao S., Di Stefano R., 1995, ApJ, 440, 22

Mao S., Paczynski B., 1991, ApJL, 374, L37

McClelland T., 2008, PhD thesis, University of Canterbury, 182 pages.

Miyake N., Sumi T., Dong S., Street R., Mancini L. Greenhill J., Kubas D., Menzies J., PLANET Collaboration 2011, ApJ, 728, 120

Mohanty S., Jayawardhana R., Mamajek E., 2007, ApJ, 657, 1064

Mollerach S., Roulet E., 2002, Gravitational lensing and microlensing. World Scientific press

Moniez M., 2010, General Relativity and Gravitation, 42, 2047

Nemiroff R. J., Wickramasinghe W. A. D. T., 1994, ApJL, 424, L21

Neuhäuser R., Mugrauer M., Seifahrt A., Vogt N., 2008, A&A, 484, 281

Paczynski B., 1986, ApJ, 301, 503

Paczynski B., 1991, ApJL, 371, L63

Paczynski B., 1996, ARA&A, 34, 419

Peng E. W., 1997, ApJ, 475, 43

Perryman M., 2011, The Exoplanet Handbook. Cambridge University Press

Perryman M. A. C., 2000, Reports on Progress in Physics, 63, 1209

Press W. H., Flannery B. P., Teukolsky S. A., 1986, Numerical recipes. The art of scientific computing. Cambridge University Press

Rahvar S., Dominik M., 2008, in Manchester Microlensing Conference "Introduction to Microlensing", in Proceedings of the Manchester Microlensing Conference: The 12th International Conference and ANGLES Microlensing Workshop, eds. E. Kerins, S. Mao, N. Rattenbury and Ł. Wyrzykowski. Published online at SISSA, Proceedings of Science.,p.37

Rattenbury N. J., 2009, MNRAS, 392, 439

Refsdal S., 1964, MNRAS, 128, 295

University of Cape Town

Ryu Y.-H., Han C., Hwang K.-H., Street R., Udalski A., Sumi T., Fukui A., Beaulieu J.-P., MiNDSTEp Collaboration 2010, ApJ, 723, 81

Ryu Y.-H., Park M.-G., 2007, ApJ, 670, 1104

Sackett P. D., 1997, ArXiv e-prints: 9709269

Schneider P., 2006, in G. Meylan, P. Jetzer, P. North, P. Schneider, C. S. Kochanek, & J. Wambsganss ed., Saas-Fee Advanced Course 33: Gravitational Lensing: Strong, Weak and Micro Part 1: Introduction to gravitational lensing and cosmology. pp 1–89

Schneider P., Ehlers J., Falco E. E., 1992, Gravitational Lenses. Springer-Verlag

Schneider P., Weiss A., 1986, A&A, 164, 237

Smith M. C., Woźniak P., Mao S., Sumi T., 2007, MNRAS, 380, 805

Sumi T., Bennett D. P., Bond I. A., Udalski A., Batista V., Dominik m., 2010, ApJ, 710, 1641

Trotta R., 2008, Contemporary Physics, 49, 71

Udalski A., 2003, , 53, 291

Udalski A., Jaroszyński M., Paczyński B., Horne K., Kubas D., 2005, ApJL, 628, L109

Udalski A., Szymanski M., Kaluzny J., Kubiak M., Krzeminski W., Mateo M., Preston G. W., Paczynski B., 1993, , 43, 289

Udalski A., Szymanski M., Kaluzny J., Kubiak M., Mateo M., 1992, , 42, 253

Udalski A., Szymanski M., Mao S., Di Stefano R., Kaluzny J., Kubiak M., Mateo M., Krzeminski W., 1994, ApJL, 436, L103

Walsh D., Carswell R. F., Weymann R. J., 1979, , 279, 381

Wambsganss J., 2006, in G. Meylan, P. Jetzer, P. North, P. Schneider, C. S. Kochanek, & J. Wambsganss ed., Saas-Fee Advanced Course 33: Gravitational Lensing: Strong, Weak and Micro Part 4: Gravitational microlensing. pp 453–540

University of Cape Town

Witt H. J., 1993, ApJ, 403, 530

Witt H. J., 1995, ApJ, 449, 42

Witt H. J., Mao S., 1994, ApJ, 430, 505

Witt H. J., Mao S., 1995, ApJL, 447, L105

Wozniak P. R., 2000, , 50, 421

Yoo J., DePoy D. L., Gal-Yam A., Gaudi B. S., Gould A., Han C., Lipkin Y., Maoz D., Żebruń K., 2004, ApJ, 603, 139

University of Cape Town